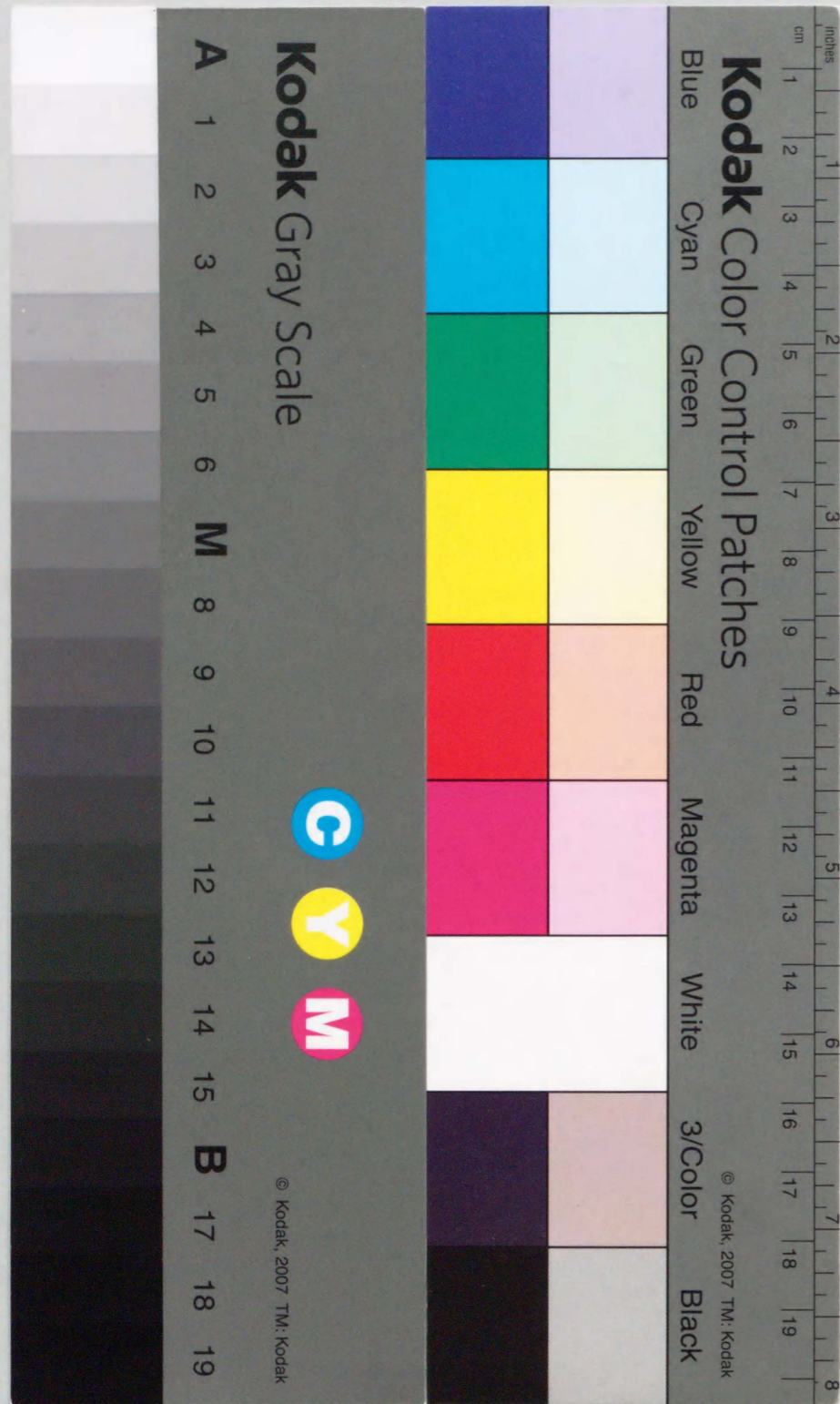Tokyo University of Agriculture and Technology

DOCTOR OF ENGINEERING THESIS

Agglomerating Fluidization of Liquid/Solid Bridging Particles and Its Control

by
Takafumi Mikami
1998

Department of Chemical Engineering

Koganei, Tokyo 184, Japan

Tokyo University of Agriculture and Technology

Doctor of Engineering Thesis

Agglomerating Fluidization of Liquid/Solid Bridging Particles and Its Control

Takafumi Mikami

1998

Department of Chemical Engineering
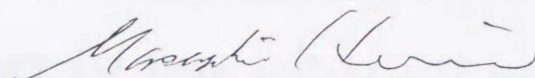
Koganei, Tokyo 184, Japan.

Tokyo University of Agriculture and Technology
Doctor of Engineering Thesis

Agglomerating Fluidization of Liquid/Solid Bridging Particles and Its Control

Takafumi Mikami
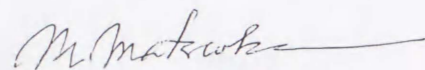
Evaluation Committee

Tokyo University of Agriculture and Technology
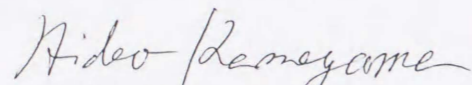Department of Chemical Engineering
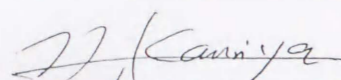
Professor   Masayuki Horio, Chair

Professor   Toshiaki Kabe
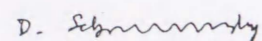
Professor   Masakuni Matsuoka

Professor   Hideo Kameyama

Associate Professor   Hidehiro Kamiya

Bhabha Atomic Research Centre, India
Head of Process Engineering Section

Dr. Dhakshinamoorthy Sathiyamoorthy

ACKNOWLEDGEMENTS

February 16 1998

Takafumi Mikami

ABSTRACT

The control of particle cohesiveness is the key issues to successfully operate many fluidized bed processes such as olefin polymerization, silicon CVD, iron ore reduction, combustion, gasification, agglomeration, coating and sub-micron powder handling. Particle cohesiveness changes very much the behavior of beds at the onset of fluidization as well as during bubbling. The objective of the thesis is to obtain fundamental information concerning the behavior of agglomerating fluidization of liquid/solid bridging particles.

In Chapter 1, the previous work on cohesive powder fluidization and direct numerical simulation of fluidization were reviewed, research needs were discussed and the objectives of the present thesis were defined.

Chapter 2 is devoted to develop phenomenological expressions for cohesive forces. Mechanistic expressions for both liquid bridges and solid bridges were obtained. For liquid bridges, approximate expressions were derived to estimate the liquid bridge force and the critical rupture distance, as functions of liquid bridge volume, distance and contact angle, for both between particles and between particle and wall. For solid bridges, the defluidization mechanism at high temperature iron particle beds was investigated from the neck observation, measurement of bed breaking velocity and diametral compression test to obtain a mechanistic model for solid bridge force.

Chapter 3 is devoted to formulate agglomerating fluidization behavior of cohesive particles from the first principle. A model SAFIRE (Simulation of Agglomerating Fluidized beds for Industrial Reaction Engineering) capable of both 2-dimensional and 3-dimensional simulations was developed based on soft sphere discrete element model. Fluidization behavior was investigated by numerical simulation for non-cohesive, liquid bridging and solid bridging particles introducing the cohesion forces investigated in Chapter 2.

Chapter 4 is devoted to establishing a engineering method to control such strong cohesiveness as metal particle sintering. To cope with the difficulties of fluidizing very sticky particles as iron a new process concept was proposed with which agglomeration behavior of solid bridging particles can be controlled by diluting the sticky particle with inert bed materials. The concept was confirmed by cold and hot reduction experiment with iron particles for powder metallurgy application. It was found that agglomeration behavior of solid bridging particles at high temperature can be successfully controlled.

In Chapter 5, the major results were summarized.

The results presented are all considered to be significant in fluidization science and very useful in the future development of various fluidized bed processes.

CONTENTS

Contents

CHAPTER 1

INTRODUCTION:
—— COHESIVE POWDER FLUIDIZATION
AND NUMERICAL SIMULATION ——

CHAPTER 1
INTRODUCTION: — COHESIVE POWDER FLUIDIZATION AND NUMERICAL SIMULATION —

1.1 FLUIDIZATION AND COHESIVE POWDERS

1.1.1 Powders and Fluidization

The powder state of solid materials is the most convenient for accomplishing their transportation, reaction, mixing, dissolution, and handling. We have a variety o powders as feed stocks materials for many industries including in the areas of medicines, foods, pigments, cosmetics, fertilizers, detergents, toners, fire extinguishers, pollen, etc. Human life has to date become very much dependent on many powders. Powder technology has been one of the key technologies since ancient days. Although powders are derived from solid materials, they can exhibit fluid like behavior in a fluidized bed. However, their features are often complex and there has been no simple theory to describe powder behaviors. Powder technology was initially developed through empirical practices to deal with the difficulties associated with powder handling.

In the modern powder technology, fluidization is one of the most widely accepted unit processes for a few several applications in chemical, physical and physico-chemical processes.

In a fluidized bed particles are supported by upwind gas flow and the fluid-solid phase behave like a liquid continuum. A bed of particulate solids is imparted the properties of fluid by the upward flow of a fluid above a minimum fluidization velocity and the resultant bed is termed as fluidized bed. The significant advantages of the fluidization are enumerated as:

1. Good solid contact because of macroscopic particle flow induced by bubbles and splash of bubbles on the surface.
2. Isothermal bed temperature because of high rate of heat transfer.
3. High thermal stability because of the large heat capacity of the bed.
4. High reaction rate due to large specific surface area, and
5. Easy transfer of particles from one column to another due to its fluid-like behavior.

The disadvantages are particle attrition, elutriation, back mixing of gas and bypassing of gas through the bubble phase.

Fluidized beds are extensively used in many industries. One of the most important applications is fluid cathartic cracking. Fluidized bed catalytic cracking (FCC) process to produce gasoline from light or heavy oil is now used all over the world. Maleic anhydride, phthalic anhydride, ethylene dichloride (oxychlorination),

acrylonitrile, LDPE (low density polyethylene) and PP(polypropylene) have been produced by catalytic processing in fluidized beds. It is also important that fluidized beds are suitable for gasification and combustion of solid materials. Fluidized beds are used a large scale power generation and waste incineration. Fluidized bed granulaters and dryers are also widely used in pharmaceutical and food industries. In relation with these applications fluidization science has been developed during the last five decades. We now have the International Fluidization Conference supported by Engineering Foundation every three years. In Japan we have Fluidization Symposium every year. Several sessions are provided every year for fluidization in AIChE Annual Meeting.

1.1.2 Fundamentals of Fluidization Engineering

There are several flow regimes in fluidized beds as shown in Fig. 1.1. When the gas flow is below the minimum fluidizing velocity u_{mf}, at which the weight of particles is balanced by the drag force and buoyancy force, the bed is said to be in incipient state. A homogeneous fluidization can be realized at low excess gas velocity $(u_o - u_{mf})$, mainly for Group A particles (Geldart (1972)[1]). Bubbling is the most common mode of fluidization. Toomey and Jhonstone (1952) [2] proposed the two-phase theory assuming that the excess gas flow, $(u_0 - u_{mf})A_t$, is accounted for flow through bubbles. Hence, the volumetric flow equivalent to minimum fluidization condition, $u_{mf}A_t$ is assumed to flow through the emulsion phase. In order to analyze reaction efficiency in a fluidized bed, the gas flow around a bubble and bubble behavior should be studied clearly.

Davidson (1961) [3] presented a gas flow model around a bubble for non-cohesive powders assuming D'Arcy's law for fluid phase and potential flow for solid phase and showed the existence of circulating gas flow zone around a bubble which is termed as 'cloud'. Davies-Taylor (1950) [4] correlated the bubble rising velocity for solid-liquid as,

$$u_b = 0.711\sqrt{gD_b} .$$ (1.1)

This relation was extended further to gas fluidized beds.

The axial distribution of bubble diameter in group B powder beds was investigated by Mori-Wen(1965)[5], Geldart (1970)[6], Chiba et al.(1973)[7] and others.

The minimum fluidization velocity, u_{mf}, is an important fundamental parameter in the science and engineering of fluidization. There are to date a large number of correlations to predict u_{mf}. However, the most popular and often cited correlation is due to Wen and Yu (1966)[8]. The Wen and Yu's equation can estimate u_{mf} with $\pm 35\%$ accuracy for non-cohesive powders.

Geldart (1972) [1] classified powders into four groups in terms of particle

density and particle diameter from the viewpoint of their bubbling fluidization behavior (Fig. 1.2) for ambient temperature and pressure conditions. For Group A particles bubble splitting and bubble coalescence are very frequent, bed expansion is very high and the minimum bubbling velocity u_b is larger than u_{mf}. For Group B particles, bubble coalescence is dominant and the minimum bubbling velocity is almost the same as u_{mf}. The Group D particles require very high gas velocity for fluidization and they tend to form a spouted bed. Group C particles are cohesive. They exhibit self-agglomeration, adhesion to wall of the fluidization column, and channeling (Fig. 1.3).

As has already been stated, a number of experimental results and theoretical considerations are reported, which can enable us now to assess and predict the fluidization behavior of non-cohesive powders. However, the behavior of cohesive powders, such as the group C powders, wet powders, hot metal and/or ash powders, is completely different from those of non-cohesive powders at the onset of fluidization as well as during bubbling. A few reports have focused the theme on the behavior of the cohesive particles as summarized in section 1.1.4. Although particle cohesiveness often causes many difficulties in many fluidized processes as described in chapter 1.1.4, there has been no study to theoretically predict fluidization behavior of cohesive particles such as minimum fluidization velocity, u_{mf}, bubble diameter and whether defluidization or agglomeration takes place or not.

Bed behavior is determined by both particle cohesiveness and macroscopic hydrodynamics. To quantify the cohesive powder behavior of different kinds and identify all the mechanical events taking place in the bed, we have to know the detail of cohesion forces and the effect of cohesion forces on the fluid and particle motions. In the next chapter the microscopic mechanisms are discussed.

Fixed bed Homogeneous Bubbling Slugging Turbulent
            fluidization fluidization   fluidization

u_{mf} u_{mb} u_c

Superficial gas velocity, u_0
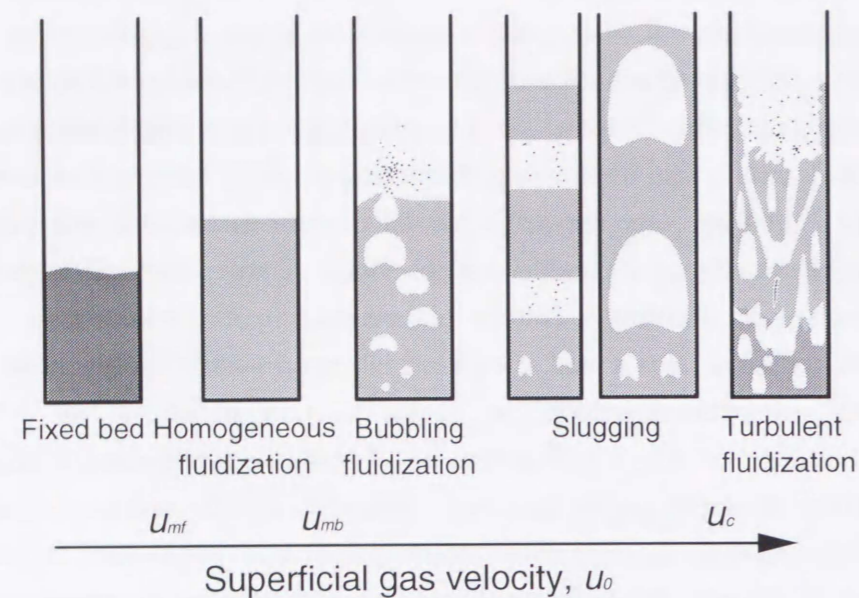
Fig 1.1   A schematic representation of variant flow regimes in gas fluidized beds
u_{mf}: minimum fluidizing velocity, u_{mb}: minimum bubbling velocity, u_c: onset
velocity of bubbling-to-turbulence transition
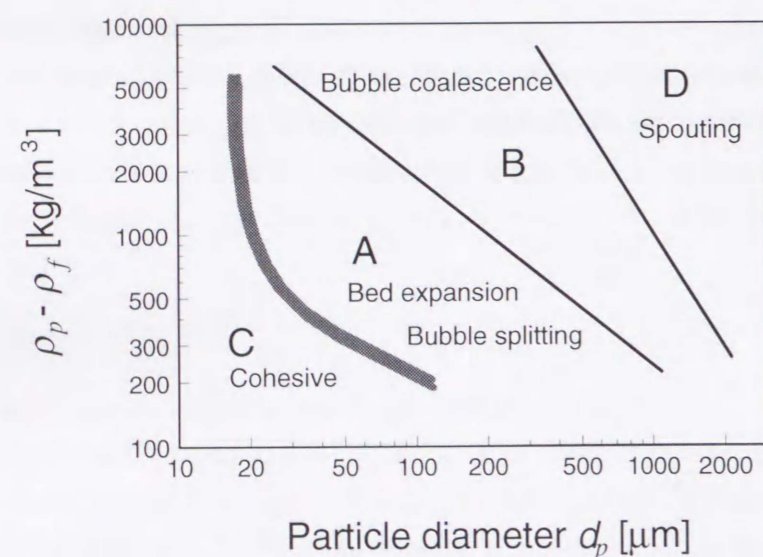
Fig. 1.2   Geldart classification of particles for fluidization by air under ambient
conditions [1]

1.1.3 Microscopic Mechanism of Particle Cohesion

As shown in Table 1.1 cohesive forces can be classified into several types such as van der Waals, electrostatic, liquid bridging, magnetic and solid bridging.

Van der Waals force

The van der Waals force is originated by dipole interaction of molecular level. The dispersion force, called London force, is the most important contribution to the total van der Waals force and is interaction between instantaneous dipole of molecules caused by fluctuation of electron cloud which have no permanent dipole moment. The van der Waals force between molecules, induced by these three interactions, is proportional to h^{-6}, where h is distance, and is a short-range force. However, the van der Waals force between particles, obtained by integration of all force for all pair of molecules, is proportional to h^{-2} and is a long range force (Israelachvili, 1985)[9]. The van der Waals force is effective for very small-sized particles because the ratio of van der Waals force to the gravity force is proportional to the square of the particle diameter. The cohesiveness of Group C powder is mainly caused by the van der Waals force. Particularly agglomeration of sub-micron powders under dry conditions is controlled by the van der Waals force. By the pressure swing granulation method proposed by Nishii et al.[10] primary particles can granulate by van der Waals force without any binders.

Electrostatic / magnetic force

By the collision between particles and between particle and wall or by the friction with a gas, the contact charge of particles takes place. The electrostatic force caused by the contact charge is about one order of magnitude less than van der Waals force for particles of 1µm size. The charged particles tend to adhere onto the wall.

Liquid bridge force

If a liquid phase exists between particles, both the static and dynamic cohesive forces act on particles. The static force originates from the contact line force and capillary pressure. The dynamic force, on the other hand, is due to viscous damping. The static liquid bridge force is important not only for wet particle fluidization under ambient condition but also for high temperature. Typical examples of high temperature are ash melting and polypropylene polymerization process. There are two approaches to estimate the static liquid bridge force between particles, namely, troidal approximation (Fischer, 1926) [11] and exact solution of Laplace-Young equation (Erle et al. [12] and De Bischop and Rigole [13]). A comprehensive set of data for liquid bride force between particles was first obtained by Mason and Clark (1965) [14]. A

Table 1.1 List of cohesion forces on particles

Cohesive Force Types	Origin	Formula	Main parameters	Remarks
Van der Waals force	Molecular dipole interaction	$F = -\dfrac{Ha\,d_p}{24h^2}$	Particle diameter and Hammaker constant	Agglomeration of very fine powders
Electrostatic force	Coulomb force	$F = \dfrac{1}{4\varepsilon_0}\pi d_p^2 \sigma^2$	Charge, moisture and permitivity	Adhesion of fine powders on the wall
Liquid bridge force (static)	Surface tension (capillary pressure and contact line force)	$F = \Delta P \pi r_1^2 + 2\pi \gamma r_1$	Liquid volume, surface tension, contact angle, distance between particles	Agglomeration under moistened atmosphere and addition of low viscous liquid
Liquid bridge force (dynamic)	Energy dissipation by liquid viscosity	$F = \dfrac{k\mu v}{\Delta x}$	Liquid volume and viscosity	Agglomeration under addition of viscous binders
Magnetic force	Magnetic force	$F = VJ\dfrac{\partial H}{\partial x}$	Magnetic field and magnetic susceptibility	Magnetic separation for magnetic materials
Solid bridge force	Mechanical strength of a bridge	?	Temperature, diffusion coefficient, tensile strength of a neck?	At high temperature or drying process of spray dring
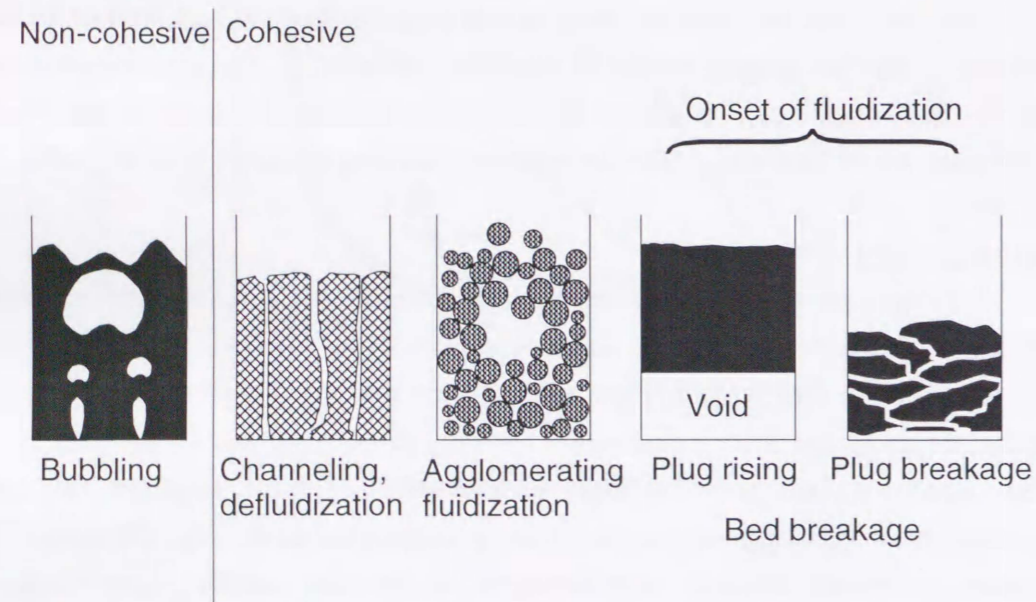
Fig. 1.3   Fluidization behavior of cohesive particles

detailed discussion on the static liquid bridge force is presented later in chapter 2. The dynamic liquid bridge force which is important for spray granulation process is caused by the viscous dumping of binders. The dynamic liquid bridge force between relatively moving spherical particles having a liquid bridge between them was first measured by Mazzone et al.[15]. Ennis et al.[16] showed that the dynamic force dominated the liquid bridge force when capillary number, which is defined as $Ca = \mu v / \gamma$, was larger than 1. The static force, on the contrary, was shown dominant for capillary number less than 10^{-3}.

Solid bridge force

The solid bridge force is caused by the solid phase formation between particles. The formation of solid bridges is caused by sintering of particles, drying of binder liquid and chemical reaction between particles. The mechanisms for solid bridging phenomena in fluidization processes have not been well established. However, the solid bridge force is a significant aspect in many engineering processes such as iron ore reduction, silicon CVD and/or spray drying. It appears from the literature survey, that reports on agglomeration mechanism caused by solid bridges are scarecely. The solid bridge caused by sintering was reported to be responsible for the defluidization behavior of copper shots, polyethylene beads and coal ash at high temperature oxidizing atmosphere by Gluckman[17] and Siegell[18]. They showed the linear relationship between the bed temperature at which defluidization started and the excess gas velocity ($u_0 - u_{mf}$) for three materials. Tardos et al.[19] investigated a fluidized bed of polyethylene beads. They presented a simple model to predict the defluidization velocity and obtained the exponential relationship between temperature and excess gas velocity. Compo et al. [20] reported that amorphous and non-ionic materials such as glass beads and polyethylene have tendency to agglomerate strongly than crystalline ionic salts which defluidize at very high temperature. None of their works have considered the mechanisms in detail and paid also not much attention to the time dependent behavior/aspect.

1.1.4 Cohesive Powder Fluidization in Industries

One of the typical processes in which defluidization often takes place is the direct iron reduction. Fluidized bed iron ore reduction processes have been developed since 1950, as an simpler alternate method than the energy intensive blast furnace process. FIOR (Fluidized Iron Ore Reduction, Venezuela) process has alone been commercially used. Serious problem is defluidization caused by agglomeration. Iron oxide particles themselves are weakly cohesive and do not show defluidization even at 1273K. On the other hand, metallic iron particles show significant cohesiveness much

below the melting temperature of iron. This cohesiveness is known to cause defluidization easily. There have been very few detailed investigations on the mechanism of defluidization of iron powders. Langstone and Stephens [21] suggested that a vague tendency for the particle stickiness in a fluidized bed using three factors, i.e. adhesive property which depends on temperature, contact area and momentum that depends on particle size and gas velocity.

$$\text{Particle stickiness in a fluidized bed} \propto \frac{adhesive\ property \times contact\ area}{momentum}.$$

Agarwal and Davis (1966) [22] showed the recorded pressure fluctuation curve in a fluidized bed when reducing iron ore by hydrogen. Iron particles of 90% reduction were fluidized well, however on the other hand, those at 95% showed sudden defluidization in less than 10sec. Gransden et al. (1970)[23] found that small fibrous nodules of iron were formed on the surface during hydrogen reduction at temperature above 983K and stated that they might be the cause of the defluidization. Kobayashi et al. (1985)[24] observed growth of fibrous iron on the surface during CO reduction of iron ore. However, they did not observe any nodules like fibers on the particles reduced by hydrogen. Since defluidization takes place for not only during reduction of iron ore particles but also in fluidization of pre-reduced metallic iron particles like steel shots at reduced atmosphere, the entangling of iron fibrous nodules may not be the primary cause of defluidization. Iron powders suitable for powder metallurgical processes should have oxygen concentration less than 0.25% and also should be small in particle diameter (40-150μm), accordingly, their cohesiveness is very serious. Further investigations to understand mechanism of defluidization are required.

Several attempts were made by researchers to prevent the bed from defluidization. In the self agglomeration method proposed by Lagston and Stephens [21], the reduced fine iron particles were captured on the surface of large iron shots of 1~2mm diameter. The large momentum of self-agglomerated particles avoided the defluidization of the bed. To prevent agglomeration, Hamada and Shirai (1965)[25] fluidized them using an agitator, Hamada and Kunii (1972)[26] used very coarse particles (0.5-1mm) and, Soma (1972)[27] used a rotary type fluidized bed. Mixing with another material such as cokes, SiC or ZrO_2 was proposed by Schenk et al. (1962)[28] and Wenzel et al.(1972)[29].

Problems caused by the cohesiveness of particles can also be found in other areas of application of fluidized beds. One example is ash agglomeration in fluidized bed combustors. It causes not only the defluidization but also erosion of the reactor wall and as well as the surface of heat exchange pipes. Once particle temperature exceeds the eutectic temperature of ash and limestone mixture, large agglomerates are formed due to the molten ash that glues the bed particles. The eutectic/melting

temperature of ash is strongly affected by their chemical composition. Indeed a little addition of alkali metal decreases the melting temperature of ash significantly and causes significant stickiness. Seki and Fujioka (1988)[30] investigated the clinker formation in a fluidized bed gasifier. They developed a defluidization map as a function of temperature and gas velocity to identify the conditions corresponding to the formation of clinkers for various types of coal. Iwadate and Horio [31] attempted to predict the size of agglomerates in a fluidized bed based on the force balance of cohesion and collision.

In fluidized bed olefin (polypropylene or polyethylene) polymerization processes, we face problems due to local hot spots caused by the poor heat removal. This leads to the formation of large agglomerates leading to defluidization[32]. Chemical vapor deposition of metallic silicon also suffers from the problem of particle cohesion [33].

The cohesion force is important even at ambient temperature. Recently, Nishii et al. [10] showed that ultra-fine particles, which have mainly the influence of van der Waals force, can be agglomerated successfully without any binder materials. It may be recalled that binders are widely used for granulation to make powders sticky by liquid bridge force in pharmacy, food and chemical industries. The addition of even small amount of binders contaminates pure materials and hence the use of binder is unwanted. Nishii et al. [10] also reported the effect of parameters, such as the granulation cycles, the duration of fluidization, the superficial gas velocity, maximum pressure difference of compaction. The roll of absorbates on particle surface on the granule diameter was also reported by Nishi et al.[34].

1.2 DIRECT NUMERICAL SIMULATION OF FLUIDIZED BEDS

1.2.1 Need for Direct Numerical Simulation

Now that the importance of cohesive powder fluidization has been recognized from both industrial and academic respects, it is necessary to construct a numerical model taking into account all mechanical events taking place in the bed.

The numerical approach which has become recently quite popular in particle technology would provide a powerful tool to investigate the detailed phenomena in the fluidized beds of both dry and cohesive particles. This kind of simulation was not possible for us in previous days because the computer resources were quite poor even for two-dimensional systems. In the present era of computers' it has been made it possible to accomplish the task of computation in an acceptable computation time. Now a computer with a CPU of 20 SpecFp95, a few hundreds megabyte in memory, and several gigabyte hard disc costs less than US$30000 (1998).

1.2.2 Numerical Simulation Model for Fluidization

In the direct simulation of fluidized beds we have two types of models, the one is two fluid model and other is discrete element method. The salient features of these two methods in a nutshell are shown in Table 1.2.

1.2.2.1 Two Fluid Model

In two fluid models a particle phase is assumed to be a fluid like continuum. The local-averaged Navier-Stokes equations (Anderson and Jackson[35]) for both fluid and solid phase are solved by taking into account fluid-solid interaction. One of the problems is how to obtain constitution equations for solid phase. There are two major approaches to arrive at constitution equations as described in the following:

Bed Elasticity Model (correlation by experimental data)

Pritchett et al.[36] obtained the regression equation for particle pressure from the experimental data of Rietema[37] on the bed elasticity and for the particle shear stress from the experimental data of Schügerl[38] as a function of the voidage. They simulated the bubbling fluidized bed by the two fluid models using these equations under the periodic boundary conditions for both vertical side boundaries. The realistic bubble formation was reproduced as shown in Fig. 1.4.

Kinetic Theory Model

Kinetic theory for granular material was developed assuming that the dynamics of particle motion is analogous to the gas dynamics. The ideal gas systems can be well described by the kinetic theory of gases based on elastic collisions of molecules. The

Table 1.2 Direct numerical simulation models for fluidization

Model		Two fluid method		Discrete element method		
				Soft sphere	Hard sphere	Direct simulation of Monte Carlo
Constitutive equations	Fluid	Local averaged Navier-Stokes equation (Anderson-Jackson)	Local averaged Navier-Stokes equation (Anderson-Jackson)	Local averaged Navier-Stokes equation (Anderson-Jackson)	Local averaged Navier-Stokes equation (Anderson-Jackson)	Local averaged Navier-Stokes equation (Anderson-Jackson)
	Particles	Empirical particle pressure correlated by bed elasticity and solid viscosity	Kinetic theory (all parameter is related to the granular temperature)	Individual interaction by a spring, a dashpot and a friction slider.	Equation of impulsive motion	Equation of impulsive motion detection of collision in a statistical manner
Typical characters		Continuum solid phase, no limitation for bed size and particle size		Tracing all particles, multiple particle contact	Tracing all particles, assuming binary contact and instantaneous repulsion	Tracing only chosen particles, assuming binary contact and instantaneous repulsion, collision detection in a statistical manner
System		Fluidized beds and CFBs for any particle size		Fluidized beds of large particle size	Fluidized beds and CFBs of large particles	CFBs of any particle size
Problems		Very sensitive to input parameters, ε^*, μ_s, fountain problem and pointed nose of a bubble, validity of analogy between fluidized particles and gases		Small time step, softened particle stiffness, limitation of particle number	Unclear bubble shape, validity of binary collision in dense region	Sampling ratio is very high, no turbulence
References		Prichett et al. (1978)[36]	Ding and Gidaspow (1990) [49]	Tsuji et al. (1993) [56]	Yuu et al. (1995) [52] Hoomans et al. (1996) [53]	Yonemura et al. (1995)[54]

Table 1.3   Kinetic theory for granular material

Granular temperature Θ [m²/s²]	$\frac{3}{2}m\Theta = \frac{1}{2}\langle v'\rangle^2$
Particle pressure p_s[Pa] (Lun et al.[48])	$p_s = (1-\varepsilon)\rho_p\Theta\big(1 + 2g_0(1-\varepsilon)(1+e)\big)$
Particle bulk viscosity λ_s[Pa.s] (Lun et al.[48])	$\lambda_s = \frac{4}{3}(1-\varepsilon)^2\rho_p d_p g_0(1+e)\sqrt{\Theta/\pi}$

Particle shear viscosity μ_s[Pa.s]

$\mu_s = \frac{4}{5}(1-\varepsilon)^2\rho_p d_p g_0(1+e)\sqrt{\Theta/\pi} + \frac{2\cdot\frac{5\sqrt{\pi}}{96}\rho_p d_p\sqrt{\Theta}}{(1+e)g_0}\left[1+\frac{4}{5}g_0(1-\varepsilon)(1+e)\right]^2$	Gidaspow et al.[39]
$\mu_s = \frac{4}{5}(1-\varepsilon)^2\rho_p d_p g_0(1+e)\sqrt{\Theta/\pi} + \frac{(1-\varepsilon)d_p\rho_p\sqrt{\pi\Theta}}{6(3-e)}\left[1+\frac{2}{5}(1+e)(3e-1)(1-\varepsilon)g_0\right]$	Syamral et al.[51]
$\mu_s = \frac{4}{5}(1-\varepsilon)^2\rho_p d_p g_0(1+e)\sqrt{\Theta/\pi} + \frac{\Theta(\rho_s(1-\varepsilon))^2}{2\beta + (1-\varepsilon)^2\frac{(1+e)(3-e)}{5}\cdot\frac{6}{d_p}\sqrt{\frac{16\Theta}{\pi}}}$	Balzer and Simonin [45]
$\mu_s = \frac{4}{5}(1-\varepsilon)^2\rho_p d_p g_0(1+e)\sqrt{\Theta/\pi} + 0.09\left[\frac{(1+1.6(1-\varepsilon)g_0)^2}{g_0} + 9.799(1-\varepsilon)^2 g_0\right]$	Dasgupta et al. [40]

Radial distribution function g_0

$g_0 = \left[1-\left(\frac{(1-\varepsilon)}{(1-\varepsilon_{min})}\right)^{\frac{1}{3}}\right]^{-1}$	Ogawa et al. [41]
$g_0 = \frac{3}{5}\left[1-\left(\frac{(1-\varepsilon)}{(1-\varepsilon_{min})}\right)^{\frac{1}{3}}\right]^{-1}$	Ding and Gidaspow [49]
$g_0 = \frac{1}{\varepsilon} + \frac{3(1-\varepsilon)}{2\varepsilon^2}$	Syamlal et al.[51]
$g_0 = \frac{1}{\varepsilon} + \frac{3(1-\varepsilon)}{2\varepsilon^2} + \frac{(1-\varepsilon)^2}{2\varepsilon^3}$	Carnahan and Starling [42]
$g_0 = \left(1-\frac{(1-\varepsilon)}{(1-\varepsilon_{min})}\right)^{-2.5(1-\varepsilon_{min})}$	Lun and Savage [43]

Momentum balance of particle fluctuation	$\frac{3}{2}\left[\frac{\partial(\varepsilon_s\rho_p\Theta)}{\partial t} + \nabla\cdot(\varepsilon_s\rho_p v_s\Theta)\right] = \tau_s:\nabla v_s - \nabla\cdot\mathbf{q} - \gamma - 3\beta\Theta$
Diffusion flux of fluctuation energy $\mathbf{q}$[J/m²s]	$\mathbf{q} = -\kappa\nabla\Theta$

Fluctuation energy diffusion coefficient κ [Pa.s]

$\kappa_{dilute} = \frac{100}{16}\frac{d_p\rho_p\sqrt{\pi\Theta}}{g_0(1+e)(82-33(1+e))}\left[1+\frac{3}{5}(1+e)^2(2(1+e)-3)(1-\varepsilon)g_0\right]$ $\kappa_{dense} = \frac{15}{2}\frac{d_p\rho_p(1-\varepsilon)\sqrt{\pi\Theta}}{(82-33(1+e))}\left[1+\frac{3}{5}(1+e)^2(2(1+e)-3)(1-\varepsilon)g_0 + \frac{4}{15\pi}(82-33(1+e))(1+e)(1-e)g_0\right]$	Lun. et al.[48]
$\kappa_{dilute} = \frac{75}{192}\frac{\rho_p d_p\sqrt{\Theta/\pi}}{(1+e)g_0}\left[1+\frac{6}{5}(1+e)g_0(1-\varepsilon)\right]^2$ $\kappa_{dense} = 2(1-\varepsilon)^2\rho_p d_p g_0(1+e)\sqrt{\Theta/\pi}$	Chapmann and Cowling[44]
$\kappa_{dilute} = \frac{5}{9}\frac{(1-\varepsilon)^2\rho_p^2\Theta}{\beta}\left[1+\frac{5}{9}\frac{(1-\varepsilon)^2\rho_p(1+e)(49-33e)}{\beta d_p}\sqrt{\frac{\Theta}{\pi}}\right]^{-1}$	Balzer and Simonin[45]

Dissipation fluctuation energy γ[J/m³s] (Jenkins and Savage[47])	$\gamma = 3(1-e^2)(1-\varepsilon)^2\rho_p g_0\Theta\big(4/d_p\sqrt{\Theta/\pi} - \nabla\cdot v_s\big)$

Algebraic formula for granular temperature (Syamral et al. [51])

$$\Theta = \left(\frac{-(K_1(1-\varepsilon)+\rho_p)\cdot\mathrm{tr}(\mathbf{D}_s) + \sqrt{(K_1(1-\varepsilon)+\rho_p)^2\cdot\mathrm{tr}^2(\mathbf{D}_s) + 4K_4(1-\varepsilon)\big[2K_3\cdot\mathrm{tr}(\mathbf{D}_s)+K_2\cdot\mathrm{tr}^2(D_s)\big]}}{2(1-\varepsilon)K_4}\right)^2$$

$$K_1 = 2(1+e)\rho_p g_0$$

$$K_2 = \frac{4}{3\sqrt{\pi}}d_p\rho_p(1+e)(1-\varepsilon)g_0 - \frac{2}{3}K_3$$

$$K_3 = \frac{d_p\rho_p}{2}\left\{\frac{\sqrt{\pi}}{3(3-e)}\left[1+\frac{2}{5}(1+e)(3e-1)(1-\varepsilon)g_0\right] + \frac{8(1-\varepsilon)}{5\sqrt{\pi}}g_0(1+e)\right\}$$

$$K_4 = \frac{12(1-e^2)\rho_p g_0}{d_p\sqrt{\pi}}$$

(m is particle mass [kg]、Θ [m²/s²] is granular temperature, v'[m/s] particle fluctuation velocity、ε_s [-] is 1-ε、e is restitution coefficient [-])

gas pressure is defined as the sum of momentum change of molecules' collision on the wall. The gas temperature is defined as the average fluctuation velocity of molecules. The gas viscosity can be modeled in terms of the momentum transfer caused by the random fluctuation of molecules. The kinetic theory can predict very well the gas characteristics i.e. viscosity, pressure and temperature even thought the simplification of collisions.

Savage and Jefrey(1981)[46], Jenkins and Savage(1983)[47] and Lun et al.(1984)[48] proposed the granular kinetic theory based on the kinetic theory of gas (Table 1.3). They assumed the following conditions:

1. Particles are spherical having smoothed surface and all of the physical properties of particles, i.e. diameter, density, friction coefficient and restitution coefficient, are the same.

2. Collisions between particles are binary and particle fluctuation velocity is isotropic.

They defined the granular temperature Θ as the mean square of the fluctuation velocity of particles.

$$\frac{3}{2}m\Theta = \frac{1}{2}m\langle v' \rangle^2 \tag{1.2}$$

They defined the granular pressure P_s, the granular shear viscosity μ_s and the granular bulk viscosity λ_s as a function of the granular temperature, Θ. Ding and Gidaspow(1990)[49] presented a direct simulation of fluidized bed of two fluid model using the kinetic theory. Boemer et al.[50] showed the behavior of a single bubble rising in a fluidized bed using three kinds of granular temperature, i.e. solving the momentum balance of particle fluctuation like Ding and Gidaspow[49], constant granular temperature and the algebraic formula for granular temperature assuming local equilibrium between generation and dissipation of fluctuating energy (Syamlal et al.[51]) The computed results of the behavior of a single bubble by the two fluid model showed that vertically elongated bubbles having pointed nose and significant splashing into freeboard(Fig. 1.5). Moreover, results are very sensitive to parameters such as particle phase viscosity and minimum fluidizing voidage.

Constitution equations for solid phase seem to be not sufficiently validated till now. There have been no discussions if kinetic theory of gas is suitable for fluidized particles which do not behave as gas but as liquid. For example, the liquid viscosity decreases, but the gas viscosity increases with temperature. We have only a few reliable data of particle viscosity for validation and correlation even for dry powders because measured viscosity data strongly depend on the experimental method and facilities. Furthermore, the particle pressure predicted by the kinetic theory faces a serious difficulty when particles are not completely fluidized (e.g. the second equation
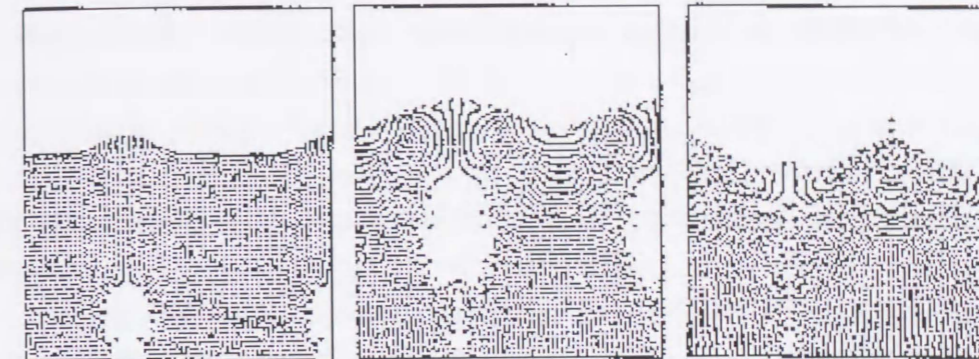
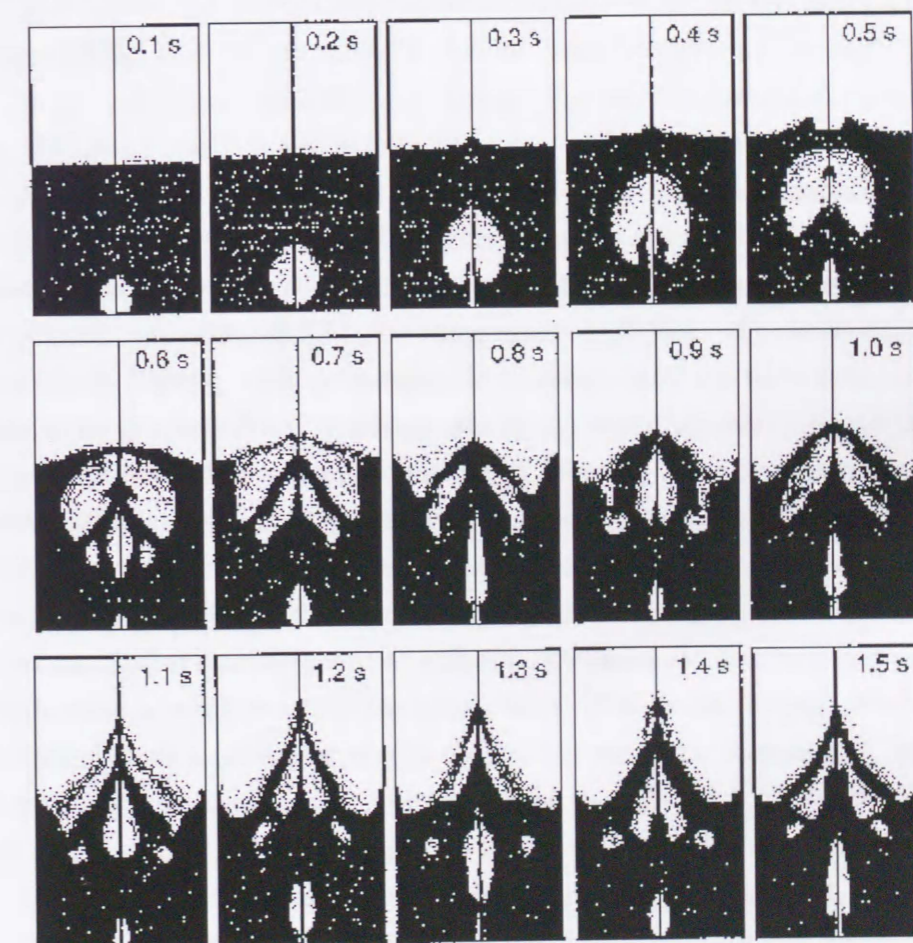Fig. 1.4   Bubble rising behavior (Prichett et al.[36])

Fig. 1.5 Single bubble rising behavior as computed by kinetic theory model (Boemer et al.[50])

of Table 1.3). It seems to be difficult to apply the two fluid models to cohesive particle fluidization.validation and correlation even for dry powders because measured viscosity data strongly depends on the experimental method and facilities. Furthermore, the particle

1.2.2.2 Discrete Element Method

The discrete element method (DEM) is extreme of the Lagrangian approach, which can trace all particles in a system based on the Newton's second law of motion. Accordingly, the equations used in the DEM model are very simple and the number of parameters is less. Moreover, as the particle is not assumed to be a continuum the DEM model can be easily applied to the discrete phenomena of powder behavior like in agglomeration, adherence on a wall and defluidization. Individually the recent remarkable developments in computer technology make it possible to trace several particles by the Newton's second law of motion.

The DEM model can be classified into several models according to the way of handling collisions, e.g. hard sphere model, DSMC, and/or soft sphere model as described in the following:

Hard Sphere Model

The hard sphere model assumes that a collision is binary in nature and contact duration is quasi-instantaneous like the molecular dynamic (MD) simulations. However, this model is essentially different from MD because the particle kinetic energy of a system is not conserved but decreased by fluid-particle drag force and inelastic collisions. The particle velocity after collision is calculated from the equation of impulsive motion for two particles taking into account the restitution coefficient. The advantage of the hard sphere model is that calculation time step can be made much larger than the soft sphere model making it possible to simulate large number of particles and over long time duration. Yuu et al. (1995) [52] and Hoomans et al. (1996)[53] presented direct numerical simulation of fluidized beds using the hard sphere model. Yuu et al.[52] handled 260000 particles (3D) and Hoomans et al.[53] did 40000 (2D). Their results did not agree well with experimental data and clear bubbles were not seen (Fig. 1.6). Since the hard sphere model treats all collisions as binary, the particle motion seems to be overestimated especially in dense region. The multiple contact may be dominant by particle interaction mechanism in fluidized beds.

Direct Simulation of Monte Carlo Model (DSMC)

In DSMC model, all particles, which are treated as hard spheres, are not traced individually. To express the system with least number of information, sample particles

are chosen, traced and copied for simulating the whole particle in the system. The occurrence of collision and the velocity of the particles after collision are determined statically in terms of voidage and relative velocity in a fluid cell and the detail locations of the whole particles in a cell at collision are not at all calculated. The assumption, that the particle behavior in a system can be represented by the motion of sample particles, is valid when the particle concentration is quite low like in CFBs. The DSMC model can treat so many particles because of such sampling technique than the soft sphere model.

Tanaka et al. simulated the particulate flow in a CFB riser using the DSMC model and presented the existence of heterogeneity of particle concentration. Yonemura et al. [54] simulated clustering particulate flow in a riser using periodic boundary conditions (Fig. 1.8). The reproduced cluster size and shape agreed well with the experimental data obtained by the laser sheet technique (Kuroki and Horio[55]).

Soft Sphere Model

In the soft sphere models, it is assumed that the Voigt visco-elastic interaction consists of a spring and dash pot at particle contact to take into account multiple particle contact (Fig. 1.7). A spring, a dash pot and a friction slider correspond to elasticity, energy dissipation estimated by the restitution coefficient and Coulomb type friction, respectively. The integration time step has to be smaller than duration of collision. Tsuji et al. [56] showed it should be less than one fifth of that. The soft sphere particle model was first applied by Cundall and Struck (1979)[57] for the quasi-static deformation of particulate bed utilizing the Hooke linear interaction and the critical dumping condition. Kiyama et al. (1983)[58] applied the soft sphere model with Hertzian non-linear spring interaction to the hopper flow consisted of 350 particles and reproduced that the Janssen type wall pressure profile under static condition, very high wall pressure at the onset of discharging and the choking with arch formation. Langston and Tuzun (1994)[59] investigated the effect of the spring constant and interaction model i.e. Hook, Hertz and the continuous interaction, and showed that the wall pressure profile is affected by these differences of models. Yoshida[60] investigated 2D and 3D hopper flow and found that the choking forming arch was frequent on 2D than 3D because degree of freedom for movement of 2D is lower than 3D.

Tsuji et al. (1993)[56] first applied the soft sphere model to a fluidized bed and presented the two-dimensional fluidization behavior of non-cohesive particles combining Anderson-Jackson equations [35] for the gas phase and the soft sphere discrete dynamics for the particle phase. The bubble formation, bubble coalescence,
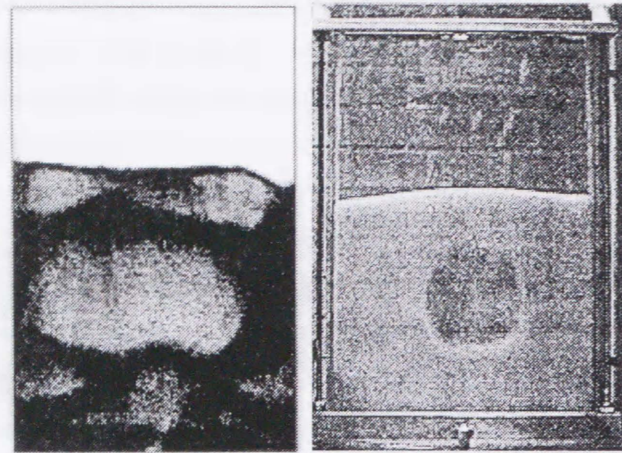
Fig. 1.6   Single bubble rising as estimated by hard sphere model (Hoomans et al. [53])
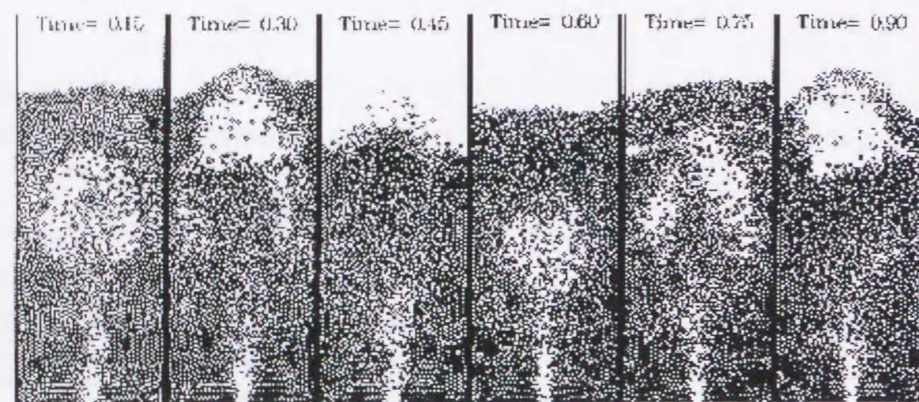

Fig. 1.7   Bubbling behavior by soft sphere particles (Tsuji et al.[56])
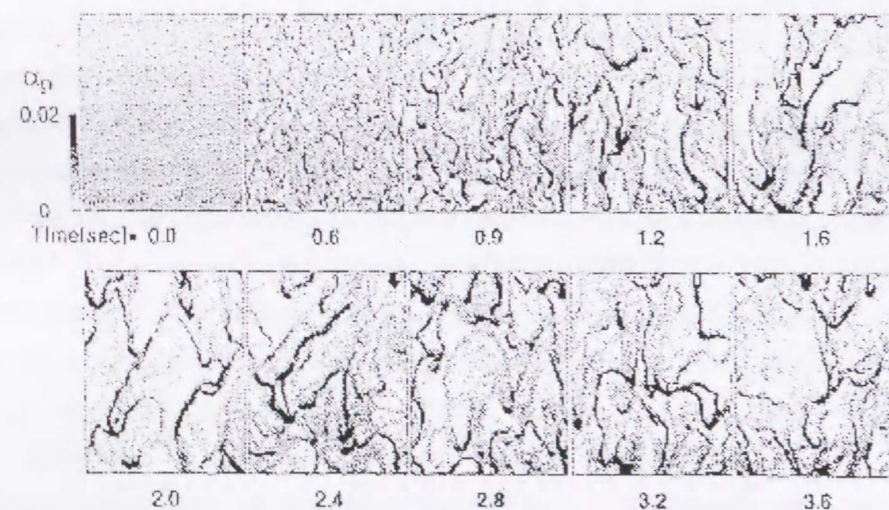

Fig 1.8   Clustering behavior in CFB riser as estimated by DSMC model (Tanaka et al.[54])

bubble eruption behavior were reproduced quite well by their soft sphere model.   They showed the time step should be smaller than one fifth of the duration of contact to avoid numerical instability.   They also calculated the behavior of single bubble in a fluidized bed consisted of 64000 particles [61] and showed clear shape of a bubble with wake and good agreement of bubble rising velocity with the empirical correlation.   The two fluid model simulations have not predicted such beautiful single bubble rising yet.

They used Hooke type interaction consisted of a quite soft linear spring and a dashpot to keep away form wasting so much time.   If the practical particle stiffness is utilized for the particle collision, the duration of contact always becomes extremely small to complete calculation on the recent computers available for us.   The practical Young modulus was reduced from 5×10^{10} Pa to 7×10^7 Pa for diameter of 2mm in the condition of Kiyama et al.[58] and 800N/m was used in Tsuji et al.[56] condition. However, they have not showed the effect of their input parameters on the bed behavior.

So far, no report has been published on the numerical simulation of cohesive powder fluidization because the simulation of dry non-cohesive powders has been the major issue of the last few years.   In case of cohesive powders agglomerates are formed which have multiple contact points within themselves.   Accordingly, it is rational especially in the case of cohesive particle simulation to take into account the softness of particles and multiplicity of particle interaction.

1.3   OBJECTIVES AND SCOPE OF THE THESIS

The objectives of the thesis is to develop the entire insight of cohesive powder fluidization technology of both fundamentals and applications from obtaining fundamental information concerning the behavior of agglomerating fluidization of liquid/solid bridging particles and to investigate an engineering method to control. This thesis is structured into five chapters and the outline of each chapter is given in the following:

CHAPTER 1: INTRODUCTION: — COHESIVE POWDER FLUIDIZATION and
            NUMERICAL SIMULATION —

Cohesive powder fluidization and direct numerical simulation of fluidization are reviewed.

CHAPTER 2: LIQUID and SOLID BRIDGE FORCES in FLUIDIZED BEDS:

The useful explicit regression expressions to estimate the liquid bridge force and the critical rupture distance as a function of liquid bridge volume, distance between the surfaces and contact angle have been obtained both for particle-particle and particle-

wall contacts. For solid bridge force the mechanism of defluidization in a fluidized bed for a typical case of gas fluidized bed of iron particles at high temperature is investigated experimentally and the solid bridge force is measured.

CHAPTER 3: DEVELOPMENT of SAFIRE MODEL and NUMERICAL ANALYSIS of COHESIVE POWDER FLUIDIZATION

The SAFIRE model (Simulation of Agglomerating Fluidized beds for Industrial Reaction Engineering) both for two-dimensional and three-dimensional conditions has been developed based on the soft sphere discrete element model. Fluidization behavior is investigated by numerical simulation for non-cohesive, liquid bridging and solid bridging particles introducing the cohesion forces (described in Chapter 2) into SAFIRE model.

CHAPTER 4: CONTROL of AGGLOMERATION BEHAVIOR in a FLUIDIZED PROCESS — A CASE STUDY: PRODUCTION of IRON POWDER through SPONTANEOUS AGGLOMERATION and SEDIMENTATION —

To develop a process, A new process for the production of iron powder in which agglomeration behavior can be controlled is demonstrated and evaluated both by cold and hot reduction experiments.

CHAPTER 5: SUMMARY of FINDINGS and CONCLUSIONS

The results of the investigations and findings of the thesis are summarized.

REFERENCES

1) Geldart, D, *Powder Technol.* **4** (1970) 41
2) Toomey, R. D., H. F. Johnstone, *Chem. Eng. Progr.*, **48** (1952) 220
3) Davidson, J. F. and D. Harrison, "Fluidized Particles", Cambridge Univ. Press (1963)
4) Davies, R. M. and G. Taylor, *Proc. Royal Soc.*, **200** (1950) 375
5) Mori, S. and C. Y. Wen, *AIChE J.,* **21** (1975) 109
6) Geldart, D., *Powder Technol.*, **4** (1970/1971) 41
7) Chiba, T., K. Terashima and H. Kobayashi, *J. Chem. Eng. Japan*, **6** (1973) 76
8) Wen, C. Y. and Y. H. Yu, *AIChE J.*, **12** (1966) 610
9) Israelachvili, J. N., Intermolecular and surface forces, Academic Press, London (1985)
10) Nishii, K., Y. Itoh, N. Kawakami and M. Horio, "Pressure swing granulation, a novel binderless granulation by cyclic fluidization and gas flow compaction," *Powder Technol.*, **74** (1993) 1
11) Fisher, R. A., On the capillary forces in an ideal soil; correction of formulae given by W. B. Haines. *J. Agric. Sci.* **16** (1926) 492
12) Erle, M. A., Dyson, D. C. and Morrow, N. R., Liquid bridges between cylinders, in a torus, and between spheres. *AIChE J.*, **17** (1971) 115
13) De Bisschop, F. R. E.and Tigole, W. J. L., A physical model for liquid capillary bridges between adsorptive solid spheres; the nodoid of plateau. *J. Colloid Interface Sci.* **88** (1982) 117
14) Masson, G. and W. C. Clark, Liquid bridge between spheres, *Chem. Eng. Sci.*, **20** (1965) 859
15) Mazzone, D. N., G. I. Tardos and R. Pfeffer, The behavior of liquid bridges between two relatively moving particles, **51** (1987) 71
16) Ennis, B. J., J. Li, G. I. Tardos and R. Pfeffer, The influence of viscosity on the strength of an axially strained pendular liquid bridge, *Chem. Eng. Sci.*, **45** (1990) 3071
17) Gluckman, M. J., J. Yerushalmi and A. M. Squires, "Defluidization Characteristics of Sticky or Agglomerating Beds", Fluidization Technology, D. L. Kearins (Ed.) Vol. II (1976) 395
18) Siegel, J. H, "High temperature Defluidization", *Powder Technol.* **38** (1984) 13
19) Tardos,G., D. Mazzone and R. Pfeffer, "Destabilization of Fluidized Bed Due to Agglomeration", *Canadian J. Chem. Eng.* **63** (1985) 377
20) Compo, P., Pfeffer, R. and G. I. Tardos, "Minimum Sintering Temperatures and Defluidization Characteristics of Fluidizable Particles", *Powder Technol.* **51** (1987) 85
21) Langston, G. G. and F. M. Stephens, Jr., "Self-Agglomerating Fluidized Bed Reduction", *J. Metals*, **12** (1960) 312
22) Agarwal, J. C. and W. L. Davis, Jr., "The Dynamics of Fluidization of Iron and Its Ores," *Chemical Engineering Progress Symposium Series*, **62** (1966) 101
23) Gransden, J. F., J. S. Sheasby and M. A. Bergougnou, "An investigation of Defluidization of Iron Ore During Reduction by Hydrogen in a Fluidized Bed," *Chemical Engineering Progress Symposium Series*, **66** (1970) 208
24) Kobayashi, M., W. W. Gudenau, W. G. Burchard and H. C. Schaefer, "Fibrous Growth of Iron Precipitates during Redution of Iron Ores by CO Gas", *Tetsu to*

Hagane, **71** (1985) 1102

25) Hamada, T. and T. Shirai, "Reduction of Iron Ores in a Stirred Fluidized Bed," *Kagaku Kougaku*, **29** (1965) 995

26) Hamada, H. and T. Kunii, *Tetsu to Hagane*, **58** (1972) 328

27) Soma, T., "The Countercurrent Reduction of Iron Ore in a Fluidized Rotary Bed." *Testu to Hagane*, **58** (1972) 1557

28) Schenck, V. H., W. Wenzel and H. D. Butzmann, "Verhindern des Zusammensinterns von Wirbelbetten bei der Reduktion von Eisenerzedn," *Archiv fur das Eisenhuttenwesen*, **33** (1962) 211

29) Wenzel, V. W., F. R. Block and E. Wortberg, "Die Reduktion von Eisenerzen mit Wasserstoff im Zweikomponenten-Fluidatbett," *Archiv fur da Eisenhuttenwesen*, **43** (1972) 805

30) Seki, E. and Y. Fujioka, *Proc. 10th Coal Utilizing Technology Meeting*, 272 (1989)

31) Iwadate, Y., H. Kamiya and M. Horio, "The prediction of sizes of ash agglomerates formed in fluidized bed gasifiers", *Proc. of the 2nd SCEJ Symposium on Fluidization*, Tokyo Japan (1996) 358

32) Miyazaki, K., M. Hanba, H. Nagashima and T. Konaka, "Fluidized Bed Technology in Gas Phase Polymerization," *Proceedings of the 3rd SCEJ(Society of Chemical Engineers of Japan) Symposium of Fluidization*, Nagoya, Japan (1997) 176

33) Houngu, K., Kagaku Sochi, **33** (1991) 78

34) Nishii, K. and M. Horio "Performance control of pressure swing granulation by changing species adsorbed on powder surface," *Fluidization VIII*,

35) Anderson, T. B. and R. Jackson, "A Fluid Mechanical Description of Fluidized Bed," *Ind. Eng. Chem. Fundamentals*, **6** (1967) 527

36) Pritchett, J. W., T. R. Blake and S. K. Garg, A numerical model of gas fluidized beds, *AIChE Symp. Ser.* No. 176, **74** (1978) 134

37) Rietema, K., The effect of interparticle forces on the expansion of a homogeneous gas-fluidized bed. *Chem. Eng. Sci.*, **28** (1973) 1493

38) Schügerl, K., M. Merz and F. Fetting, Rheologische Eigenschaften von gasdurchstromten Fliessbettsystemen, *Chem. Eng. Sci.*, **15** (1961) 1

39) Gidaspow, D., R. Bezburuah and J. Ding, " Hydrodynamics of Circulating Fluidized Beds: Kinetic Theory Approach," *Fluidization VII* (1992) 75

40) Dasgupta, S, R. Jackson and S. Sundaresan, "Turbulent Gas-Particle Flow in Vertical Risers", *AIChE J.* **40**, No. 2 (1994)

41) Ogawa, S., A. Umemura and N. Oshima, " ON the Equation of Fully Fluidized Granular Materials," *J. Appl. Math. Phys.*, **31** (1980) 483

42) Carnahan, N. F. and K. E. Starling, "Equations of State for Non-attracting Rigid Spheres", *J. Chem. Phys.* **51** (1969) 635

43) Lun, C. K. K. and F. B. Savage, "The Effects of Impact Velocity Dependant Coefficient of Restitution on Stress Developed by Sheared Granular Materials", *Acta Mecanicaa*, **63** (1986) 15

44) Chapman, S. and T. G. Cowling, 'The mathematical Theory of Non-Uniform Gases,' 3rd Ed., Cambridge, Cambridge University Press (1970)

45) Balzer, G. and O. Simonin, 'Extension of Eulerian Gas-Solid Flow Modelling to Dense Fluidized Bed, *Proc. 5th Int. Symp. on Refined Flow Modeling and Turbulence Measurements*, P. L. Viollet, ed., Paris (1993) 417

46) Savage, S.B., and D. J. Jeffrey, 'The Stress Tensor in a Granular Flow at High Shear

Rates,' *J. Fluid Mech.*, **110** (1981) 255

47) Jenkins, J. T. and S. B. Savage, A theory for the rapid flow of identical, smooth, nearly elastic, spherical particles, *J. Fluid Mech.*, **130** (1983) 187

48) Lun, C. K. K., S. B. Savage, D. J. Jeffrey and N. Chepurniy, 'Kinetic Theories for Granular Flow: Inelastic Particles in Couette Flow and Slightly Inelastic Particles in a General Flow Field,' *J. Fluid Mech.*, **140** (1984) 223

49) Ding, J. and D. Gidaspow, 'A Bubbling Fluidization Model Using Kinetic Theory of Granular Flow,' *AIChE J.*, **36** (1990) 523

50) Boemer, A., H. Qi and U. Renz, Eulerian simulation of formation at a jet in a two-dimensional fluidized bed, IEA/FBC Mathematical model meeting (1995)

51) Syamral, M., T. J. O'Brien, MFIX Documentation ,Theory Guide, Technical Note DOE/METC-94/1004 (1993)

52) Yuu, S., K. Ikeda and T. Umekage, Numerical simulation of flow fields in three dimensional fluidized bed and experimental verification, *Proc. of the 2nd International Conference on Multiphase Flow, April, Japan* FB2-1

53) Hoomans, B. P. B., J. A.M. Kuipers, W. J. Briels and W. P. M. Swaaij, Discrete particle simulation of bubble and slug formation in a two-dimensional gas fluidized bed: a hard-sphere approach. *Chem. Eng. Sci.* **51** (1996) 99

54) Yonemura, S., T. Tanaka and Y. Tsuji, Cluster Formation in Dispersed Gas-Solid Flow (Effects of Physical Properties of Particles), *Proceeding of 2nd International Conference of Multiphase Flow*, April, Kyoto (1995)

55) Horio, M. and H. Kuroki, *Chem. Eng. Sci.* **49** (1994) 1213

56) Tsuji, Y., T. Kawaguchi and T. Tanaka, Discrete particle simulation of two-dimensional fluidized bed. *Powder Techol.* **77** (1993) 79

57) Cundall, P. A. and O. D. L. Strack, 'A discrete numerical model for granular assemblies,' *Geotechnique*, **29** (1979) 47

58) Kiyama, H. and H. Fujimura, 'Application of Cundall's discrete block method to gravity flow analysis of rock-like granular materials,' *J. Jpn. Soc. Civ. Eng.*, **333** (1983) 137

59) Langston, P. A., U. Tuzun and D. M. Heyes, 'Continuous Potential Discrete Particle Simulations of Stress and Velocity Fields In Hoppers: Transition From Fluid To Granular Flow,' *Chem. Eng. Sci.*, **49** (1994) 1259

60) Yoshida, J., Study on Static Pressures on Granular Materials in a Silo Using the Distinct Element Method, *Funtaikougakukaisi*, **32** (1995) 16

61) Kawaguchi, T., Y. Yamamoto, T. Tanaka and Y. Tsuji, 'Numerical Simulation of Single Rising Bubble in a Two-dimensional Fluidized Bed,' *Proceedings of The 2nd International* Conference *on Multiphase Flo*w, Vol. 4, FB2-17 '95-Kyoto, April, 1995, Japan

CHAPTER 2

LIQUID AND SOLID BRIDGE FORCES IN

FLUIDIZED BEDS

CHAPTER 2
LIQUID AND SOLID BRIDGE FORCES IN FLUIDIZED BEDS

2.1   INTRODUCTION

Several troubles take place fluidized process at high temperature due to particle cohesiveness and the causes chiefly consist of two types.   The first one is liquid bridge force and very important for the ash agglomeration by molten ash of low melting temperature in pressurized fluidized bed gasifier.   The second one is solid bridge force and very considerable in gas phase poly-olefin polymerization, silicon chemical vapor deposition, iron ore reduction and spray granulation.   In order to solve the problems at high temperature these two forces have to be well understood.

As has been already described in Chapter 1, the liquid bridge force is a well analyzed topic.   However, one of the problems still remaining unresolved is the availability of explicit equations to estimate the liquid bridge force and the critical rupture distance as a function of liquid volume, separation distance and contact angle. Although the troidal approximation with the assumption circular shape of a bridge can provide useful expression for liquid bridge force, it does not provide any information for the rupture condition of a bridge.   On the particle-particle interaction force due to liquid bridging there has been several studies, Fisher [1], Mason and Clark [2], Ennis et al. [3], Lian et al. [4], Hotta et al. [5], Mazzone et al. [6], Erle et al. [7], De Bisschop and Rigole[8] and Kousaka et al.[9]

In solid bridge forces metal-metal bridging is the one of the most important phenomena because the iron ore reduction process have been a typical high temperature process for long time because of its capability of continuous powder handling and good gas–solid contact.   We have only overall observation by Agarwal and Davis [10], Grandsen et al. [11], Kondo et al. [12] for metal-metal bridging and some preliminary observation by Langston and Stephen [13], Kobayashi et al. [14] for iron ore reduction. There is no precise study on the detailed mechanism of solid bridging that should be completely different from liquid bridging one.   Formation of solid bridges between particles caused by neck growth due to sintering is an outcome of inter-particle cohesion force especially with metal particles.

There are in principle four significant mechanisms for sintering of powders, i.e. viscous flow, vaporization and condensation, volume diffusion and surface diffusion. In many cases, surface diffusion is the most significant in an early stage of sintering, then volume diffusion takes over at the middle stage which causes densification and

contraction. Kuczynski [15] proposed a theory of sintering for surface and volume diffusion mechanisms. His theory was confirmed experimentally [16, 17, 18]. Tardos et al. [19] discussed the defluidization mechanism based on the viscous flow sintering model (Rumpf [20]) for glass beads and polymer beads. However, there is no investigation on the defluidization mechanisms of iron particles and its cohesion force.

In this chapter, the following investigations have been carried out:

On the liquid bridge force:

1   Regression expressions to estimate liquid bridge force and critical rupture distance as a function of liquid bridge force, separation distance and contact angle both between particles and between particle and wall have been obtained.

On the solid bridge force:

2   The growth of a "neck", i.e. the contacting section between the neighboring steel particles, was investigated using a scanning electron microscope and the mechanism of defluidization in a fluidized bed is discussed.

3   The temperature at which the cohesion force becomes not negligible was determined from the measurement of bed breaking velocity from a fixed bed-to-fluidized bed transition.

4   The cohesion force between particles was estimated both from the data on bed breaking velocity and the diametral compression test.

5   In order to explain the particle behavior in a high-temperature bubbling fluidized bed of iron particles, the forces acting on a single particle were estimated. The prediction was confirmed experimentally from the defluidization behavior of a fluidized bed of iron particles.

2.2   LIQUID BRIDGE FORCE

2.2.1   Theoretical Description

There are two contributions for liquid bridge force, i.e., static force and dynamic force and this has been already discussed in Chapter 1. The liquid viscosity is assumed to be so low in this work. Hence, that the dynamic liquid bridge force can be neglected safely. To validate this assumption let us examine the contribution of both viscosity and surface tension to a liquid bridge force by using the dimensionless capillary number $Ca = \mu v / \gamma$, i.e. the ratio of the dynamic force to static force. Ennis et al. [3] showed that the viscosity effect dominated the liquid bridge force when Ca was larger than 1. On the contrary the surface tension dominated it when Ca was less than 10^{-3}. In the case of water at 20^0C its surface tension, γ, is 72.75×10^{-3} N/m and viscosity μ is 1.01×10^{-3} Pa s. Since particle to particle relative velocity v may not

exceed 1m/s, the capillary number should be less than 0.014. Therefore the assumption that the dynamic liquid bridge force can be neglected is reasonable for water.

Moreover, the liquid transport between particles and the change of liquid bridge volume by the flow of the surface water are neglected in this work. This is equivalent to assume a liquid viscosity sufficiently small so as to neglect the dynamic liquid bridge force, which is relatively smaller than the static bridge force, and, on the other hand, to assume a large viscosity which is insufficient for a liquid film traveling from areas around the neighboring contact sites. This assumption should be valid as long as the water content is low.

For a static liquid bridge (Fig. 2.1) there have been two typical approaches. One is the troidal approximation (Fisher[1], 1926) and another is the exact numerical solutions of the following Laplace-Young equation (Eq.   (2.1))

$$2\hat{H} = \frac{d^2\hat{y}/d\hat{x}^2}{\left[1+\left(d\hat{y}/d\hat{x}\right)^2\right]^{3/2}} - \frac{1}{\hat{y}\left[1+\left(d\hat{y}/d\hat{x}\right)^2\right]^{1/2}} \qquad (2.1)$$

where $H = Hr_p$ is the dimensionless curvature and r_p is the particle radius. The boundary conditions are $\hat{y} = \sin\phi$ and $d\hat{y}/d\hat{x} = 1/\tan(\theta+\phi)$ at $\hat{x} = \hat{x}_c$ and $d\hat{y}/d\hat{x} = 0$ at $\hat{x} = 0$ where ϕ is the filling angle, θ is the contact angle. Eq.   (2.1) can be integrated to give

$$\frac{\hat{y}}{\left[1+\left(d\hat{y}/d\hat{x}\right)^2\right]^{1/2}} + H\hat{y}^2 = C. \qquad (2.2)$$

From the above boundary conditions at $\hat{x} = \hat{x}_c$ the integration constant C is estimated as:

$$C = \sin\phi\sin(\phi+\theta) + \hat{H}\sin^2\phi \qquad (2.3)$$

From the boundary condition at $\hat{x} = 0$, the neck radius at the center of liquid bridge $\hat{y}_0$ also can be estimated as follows:

$$\hat{y}_0 = \begin{cases} C & \text{if} \quad \hat{H} = 0 \\ \dfrac{-1+\sqrt{1+4\hat{H}C}}{2\hat{H}} & \text{if} \quad \hat{H} \neq 0 \end{cases} \qquad (2.4)$$

Accordingly, the interface profile can be obtained by the modified Euler method using initial point $\hat{y}_0$, the first and the second derivative of the function $\hat{y}$.

Lian et al. [4] found out that the one with the troidal approximation, which is sometimes called gorge model (Hotta et al.[5]), had errors only less than 10% and that the two models agreed well with the experimental results (e.g. Mason and Clark, 1965[2]). However, the practical difficulty accompanied with the above two models is that they cannot provide the liquid bridge force as an explicit function of the liquid bridge volume and the separation distance.
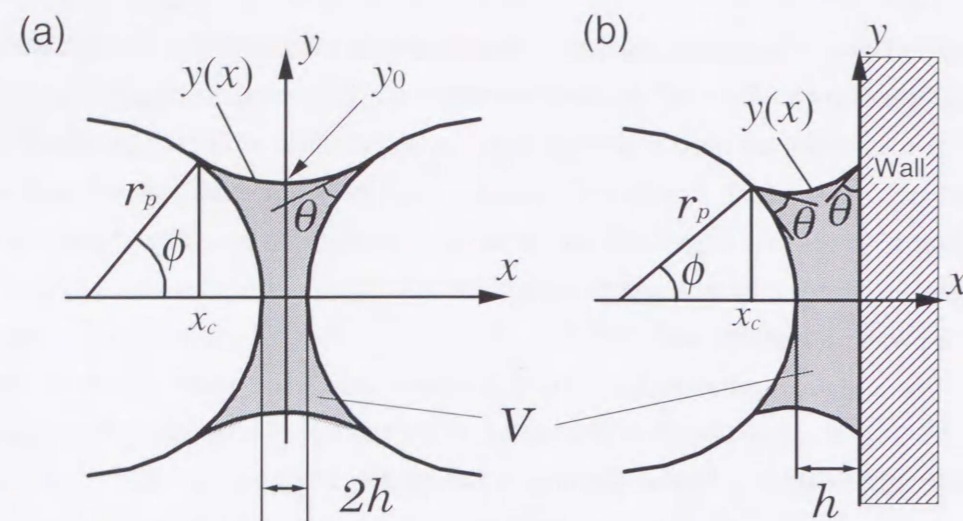
Fig. 2.1   Schematic of liquid bridges, (a) between spheres, (b) between a sphere and a wall (ϕ is filling angle and θ is contact angle)
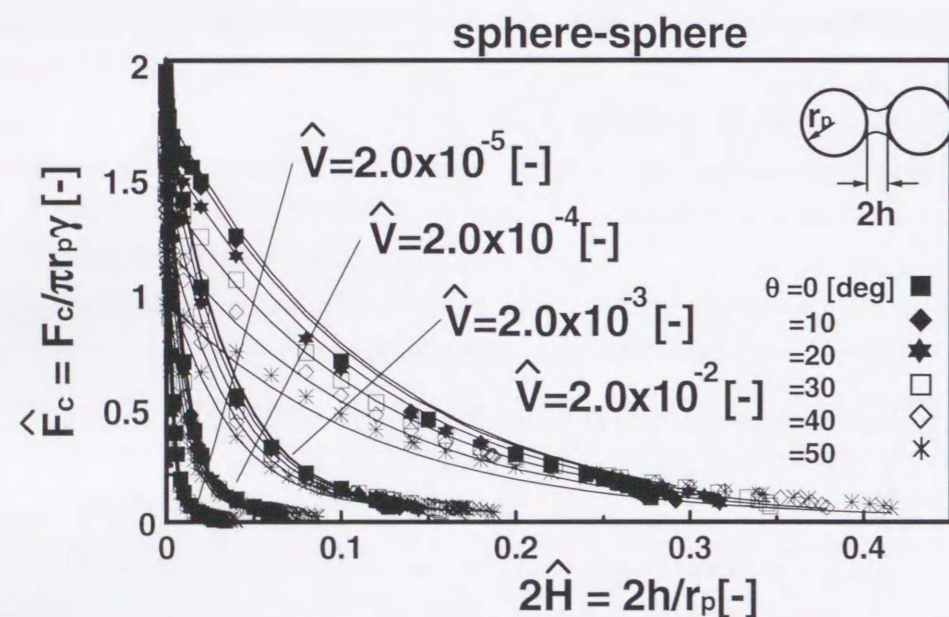

Fig. 2.2 (a) Calculated dimensionless liquid bridge force vs. dimensionless distance between spheres

The additional important parameter is the critical rupture distance of the liquid bridge $h_c = h_c / r_p$ at which the bridge ruptures. However, the troidal approximation cannot predict the critical rupture distances. On the other hand, as reported by Mazzone et al. [6] and Lian et al. [4] the exact solution of the Laplace-Young equation can provide the critical rupture distance accurately from the critical separation distance above which no solution can be obtained for the equation. Lian et al. [4] found the following simple relationship between the critical rupture distance and the dimensionless liquid bridge volume from their calculation for two spheres:

$$\hat{h}_c = (0.5\theta + 1)\sqrt[3]{\hat{V}} . \tag{2.5}$$

In the following regression expressions similar to the above are also derived for the two spheres system and for the sphere and wall system.

2.2.2   Regression Expressions

The Laplace-Young equation was solved employing the modified Euler method under constant liquid volume $\hat{V} = V / r_p^3$ conditions.

$$\hat{V} = 2\pi \int_0^{\hat{x}_c} \hat{y}^2 d\hat{x} - \tfrac{2}{3}\pi(1 - \cos\phi)^2 (2 + \cos\phi) \tag{2.6}$$

The liquid bridge force $\hat{F} = F_c / \pi r_p \gamma_c$ is calculated:

$$\hat{F}_c = 2\hat{y}_0 \left(\hat{H}\hat{y}_0 + 1 \right). \tag{2.7}$$

The calculation was repeated for both forces between spheres and between a wall and a sphere to obtain the relation between the liquid bridge force and the separation distance. The symbols in Fig. 2.2 show the calculated dimensionless liquid bridge force, for a) between spheres and b) between a wall and a sphere. Though there were two solutions which converged to a single solution at a critical separation distance, only the stable solutions prescribed by Erle et al. [7], De Bisschop and Rigole [8] and Lian et al. [4] were plotted in Fig. 2.2(a, b). From the regression analysis the numerical data were correlated by the following equation with the parameter A, B and C:

$$\hat{F}_c = \exp(A\hat{h} + B) + C \tag{2.8}$$

force between spheres: $A = -1.1\hat{V}^{-0.53}$

$$B = (-0.34\ln\hat{V} - 0.96)\theta^2 - 0.019\ln\hat{V} + 0.48 \tag{2.9}$$

$$C = 0.0042\ln\hat{V} + 0.078$$

force between a sphere and a wall: $A = -1.9\hat{V}^{-0.51}$

$$B = (-0.016\ln\hat{V} - 0.76)\theta^2 - 0.12\ln\hat{V} + 1.2 \tag{2.10}$$

$$C = 0.013\ln\hat{V} + 0.18 .$$

For the critical rupture distance $\hat{h}_c$ the following simple relations were

obtained following their ways:

between spheres: $\hat{h}_c = (0.62\theta + 0.99)\hat{V}^{0.34}$ (2.11)

between a sphere and a wall: $\hat{h}_c = (0.22\theta + 0.95)\hat{V}^{0.32}$.   (2.12)

The lines in Fig. 2.3 show the numerical critical separation distances and the regression expressions.   Even in the analysis of Ennis et al. [3] for the oscillating liquid bridge between particles the dynamic change of the contact angle was not considered.   We also neglect the dynamic change of the contact angle θ during a contact and a constant value of $\theta = 0$ rad was used in all simulations.
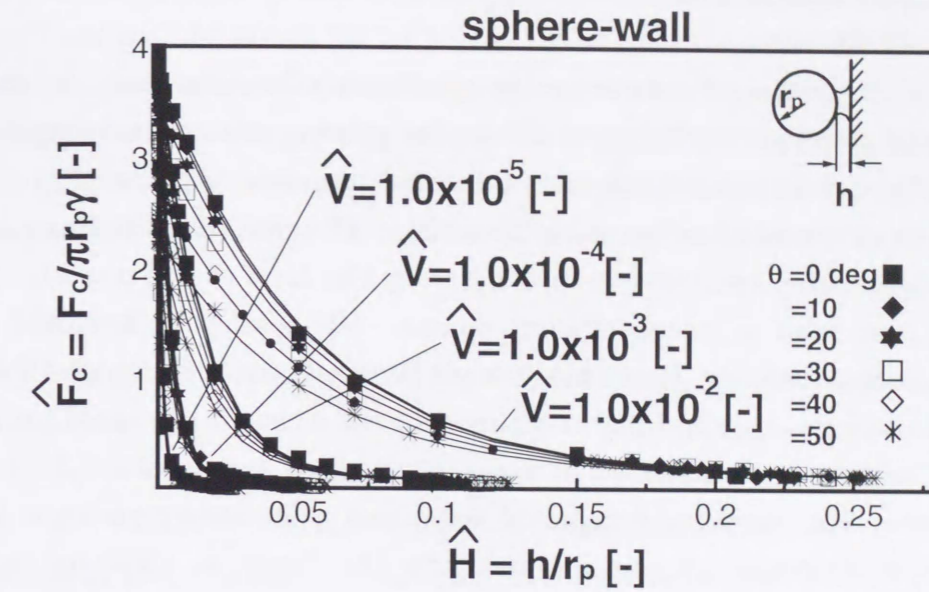
Fig.2.2 (b)   Calculated dimensionless liquid bridge force vs. dimensionless distance between a sphere and a wall
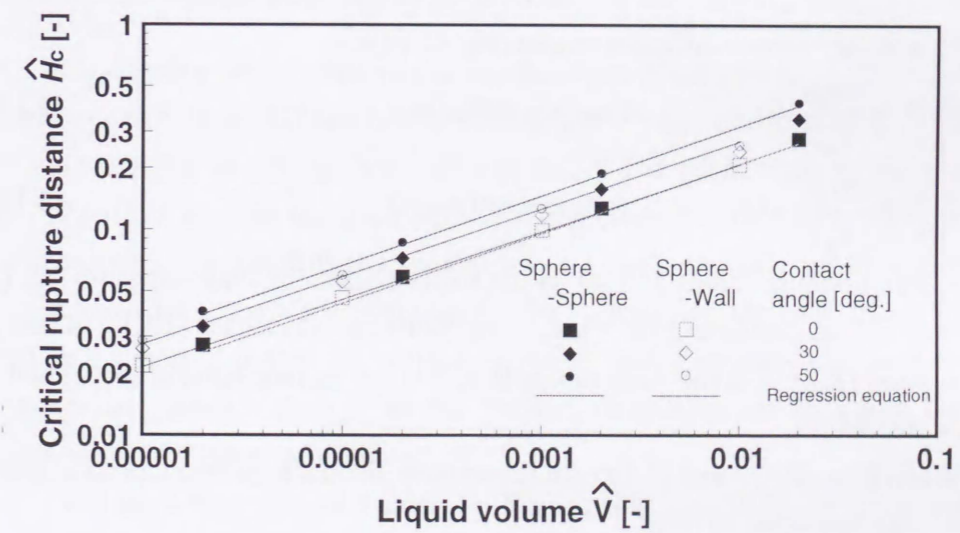
Fig. 2.3   Calculated critical rupture distance between spheres and between a sphere and a wall

2.3 SOLID BRIDGE FORCE — A CASE STUDY: IRON PARTICLES AT HIGH TEMPERATURE —

Powder metallurgy, characterized by its versatility for making complex shapes with advanced properties, has been and still is a fast growing industry extending its use in automobiles, household machines, etc. Presently iron powder is produced by a very long belt furnace is used for reduction and annealing. However, this process requires a large high-temperature space only for treating a very thin layer of iron powder. It is, accordingly, far from an energy-efficient process. To develop an improved iron powder production process, "fluidization" would be one of the key principles for the new process because of its capability of continuous powder handling and good gas-solid contact. For direct iron ore reduction processes, fluidized beds were once tested in many countries but abandoned because of the serious defluidization problems arose from cohesion of metallic iron particles, as described in Chapter 1. However, there is few investigation on the defluidization mechanisms of iron particles and cohesion force in detail.

2.3.1 Theoretical

2.3.1.1 Mechanism of Sintering

The surface diffusion and the volume diffusion mechanisms are the most significant ones in sintering of metal powders. Kuczynski [15] derived the following relation between neck growth time and neck radius based on the surface diffusion model (Eq. (2.13)) and the volume diffusion model (Eq. (2.14)):

$$\frac{x_{neck}^7}{a^3} = \frac{56\gamma\delta^4}{k_B T} D_s t \qquad \text{(surface diffusion)} \qquad (2.13)$$

$$\frac{x_{neck}^5}{a^2} = \frac{10\gamma\delta^3}{k_B T} D_v t \qquad \text{(volume diffusion)} \qquad (2.14)$$

where a is the curvature radius [m], D_s is the surface diffusion coefficient [m²/s], D_v is the volume diffusion coefficient [m²/s], k_B is the Boltzmann constant [J/K], t is time [s], T is temperature [K], x is the neck radius [m], γ is the surface tension [N/m] and δ is the lattice constant [m].

When Eqs. (2.13) and (2.14) are rearranged, the neck growth can be expressed as the following functions of time:

$$x_{neck} = \left(\frac{56\gamma\delta^4}{k_B T} D_s a^3 t \right)^{1/7} \qquad \text{(surface diffusion)} \qquad (2.15)$$

$$x_{neck} = \left(\frac{10\gamma\delta^3}{k_B T} D_v a^2 t \right)^{1/5} \qquad \text{(volume diffusion)} \qquad (2.16)$$

Neck diameter increases with time as per one seventh power law for surface diffusion and one fifth power law for volume diffusion. The temperature for sintering of iron compacts in powder metallurgy process varies from 1373-1473 K, where sintering mechanism is regarded as volume diffusion. However, it has been said that surface diffusion is the main mechanism that plays in sintering in iron powder at lower temperature (<1323 K)[18]. The surface diffusivity of iron (Matsumura [18]) is given by:

$$D_s = D_{0,s} \, exp(-E_s/RT) \qquad (2.17a)$$

where the frequency factor, $D_{0,s}$, and the activation energy of volume diffusion, E_s, are given as follows:

$$D_{0,s} = 2.4 \, \text{m}^2/\text{s}, E_s = 2.42 \times 10^5 \, \text{J/mol} \qquad (T<1180 \text{ K}) \qquad (2.17b)$$

$$D_{0,s} = 5.2 \times 10^{-2} \, \text{m}^2/\text{s}, E_s = 2.21 \times 10^5 \, \text{J/mol} \, (1180 \text{ K}<T) \qquad (2.17c)$$

The change at 1180 K is due to phase transition from α-Fe to γ-Fe.

For the volume diffusion coefficient, the following expression is often used for calculation:

$$D_v = D_{0,v} \, exp(-E_v/RT) \qquad (2.18a)$$

where the frequency factor, $D_{0,v}$, and is the activation energy of volume diffusion, E_v, are given as follows [21][22]:

$$D_{0,v} = 4.4 \times 10^{-5} \, \text{m}^2/\text{s}, E_v = 2.53 \times 10^5 \, \text{J/mol}[7] \, (933< T <1013 \text{ K}) \qquad (2.18b)$$

$$D_{0,v} = 4.4 \times 10^{-4} \, \text{m}^2/\text{s}, E_v = 2.53 \times 10^5 \, \text{J/mol}[7](1073< T <1163 \text{ K}) \qquad (2.18c)$$

$$D_{0,v} = 4.4 \times 10^{-5} \, \text{m}^2/\text{s}, E_v = 2.80 \times 10^5 \, \text{J/mol}[8](1273< T <1573 \text{ K}) \qquad (2.18d)$$

Concerning with the above two mechanisms, Fischmeister *et al.* [17] found that the neck growth follows 1/7 law below 1195 K and 1/5 law above 1623 K. Matsumura [18] found that the switching from 1/7 law to 1/5 law takes place in the temperature range 1323~1573 K. As has been already recognized [17][18], there exists a paradox. The Kuczynski's volume diffusion model gives a neck diameter much larger than the value predicted by the surface diffusion model. However, the well known fact in the case of iron sintering is that the surface diffusion model predicts well and agrees well with observed values. Hence, in the present discussion let us adopt the surface diffusion model for the present cases.

The neck diameter calculated by Kuczynski's Eq. (2.15) is delineated in Fig. 2.4 as a function of time. It can be understood from Fig. 2.4 that the neck diameter reaches a recognizable size in a very short period. Therefore, even in a fluidized bed, where particles are intermittently mixed, each particle have sufficient contact time to form sintered necks especially in dead spaces and in wall regions where bubbles do not pass. Once sintering is started, the necks keep growing and the cohesion force

increases continuously.

Using this neck growth vs. time relationship to iron powder fluidization at high temperature, the defluidization behavior of iron particles can be discussed.

2.3.1.2   Cohesion Force for a Neck

The cohesion force for a neck, F, is calculated from the following equation:

$$F_c = \pi x^2 \sigma_{neck} \tag{2.19}$$

where σ_{neck} is the tensile strength of a neck between two particles.   Since the neck region is supposed to contain more lattice defect than the bulk, the tensile strength of a neck should be smaller than the one for the bulk σ_t.   However, as far as the authors' knowledge is concerned, no data seems to be available for the tensile strength of a neck at high temperatures.   Hence, the tensile strength σ_t of the bulk of 0.2 %C steel shown in Fig. 2.5. [23] is used as the reference values in the following.

2.3.1.3   Diametral Compression Test

The diametral compression test can be employed to determine the cohesion force.   When a disk shaped test piece of diameter D_d and thickness W is used as a sample, the tensile strength of the test piece S_t can be calculated from the following equation [24]:

$$S_t = \frac{2F_0}{\pi D_d W} \tag{2.20}$$

where F_0 is the fracture load.

The relation between the tensile strength of a bed of spherical particles and the cohesion force between particles was derived by Rumpf [25] as

$$S_t = \frac{1-\varepsilon}{\pi} n_k \frac{F}{d_p^2} \tag{2.21}$$

where n_k is the coordination number for a particle and it is the number of other particles that are in contact with a selected particle.   It can be predicted by [26]:

$$\varepsilon n_k = \pi \tag{2.22}$$

Substituting the empirical relation Eq. (2.22) into Eq. (2.21), we can obtain Eq. (2.23).

$$S_t = \frac{1-\varepsilon}{\varepsilon} \cdot \frac{F}{d_p^2} \tag{2.23}$$

2.3.1.4   Bed breaking Velocity

The minimum fluidization velocity u_{mf} must be determined from the u_0-ΔP velocity can be utilized to characterize the particle cohesion force in the initial fixed
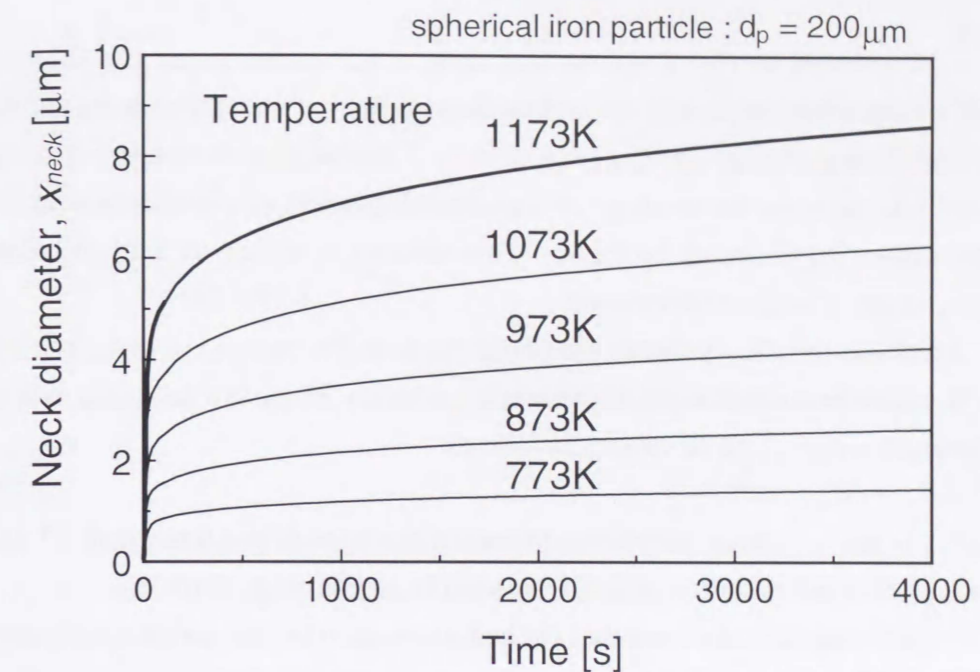
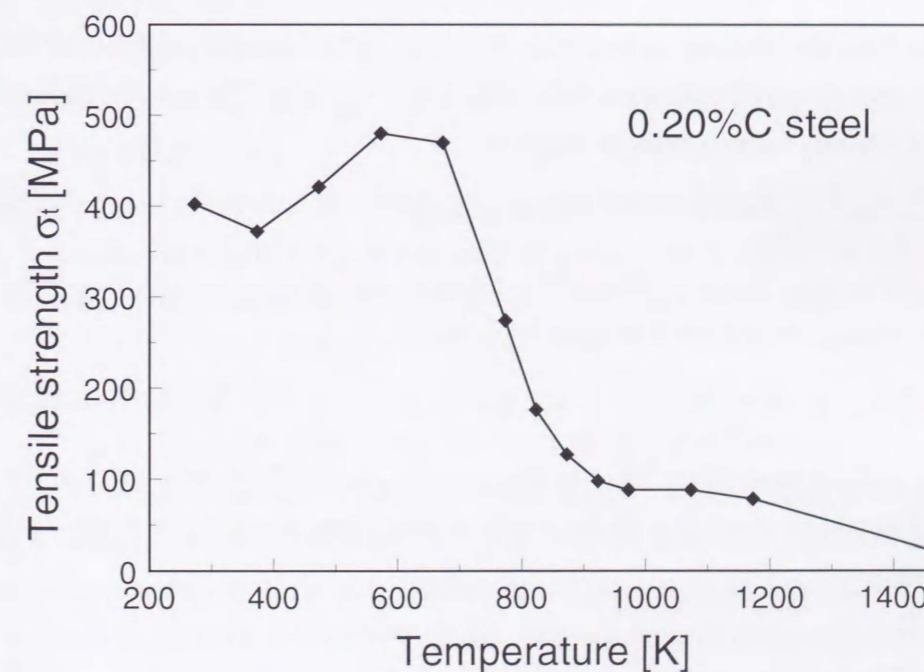Fig. 2.4 Neck growth predicted by the surface diffusion mechanism [15].

Fig. 2.5   Tensile strength of 0.2% steel as a function of temperature [23].

bed.

As illustrated in Fig. 2.6, a sudden drop of ΔP occurs when gas velocity is increased relationship obtained for decreasing superficial gas velocity so as to eliminate the effect of the initial structure of a packed bed. However, u_0-ΔP data for increasing the gas and this indicates the breakage of the original structure of a fixed bed which was kept consolidated by the cohesion force. This velocity is termed as the bed breaking velocity u_{bb} in the subsequent discussion.

The force required to break the bed is equal to the excess pressure drop at the onset of fluidization multiplied by the bed cross section. Thus, at $u_0 = u_{bb}$ the observed total pressure drop $\Delta P_{tot.}$ can be written as follows:

$$\Delta P_{tot.} = \Delta P_{bed} + \Delta P_c \tag{2.24}$$

where ΔP_{bed} is the weight of the bed supported by the upward gas flow, and ΔP_c is the contribution of the cohesion force caused by solid bridge between particles.

Nishii et al. [27] observed that the bed breakage was initiated at the distributor level. The bed breaking velocity closely relates to the breakage of the contacting point between the bottom of the bed and the distributor.

We can use the following Wen and Yu [28]correlation to predict u_{mf}:

$$Re_{mf} = \sqrt{33.7^2 + 0.0408Ar} - 33.7 \tag{2.25}$$

When the Archimedes number is less than 33000 as in the present case (i.e. 2500, for 200 μm steel shot fluidized with air at 0.24 m/s), Eq. (2.25) can be reduced to Eq. (2.26) for viscous force dominant region as:

$$u_{mf} = \frac{d_p^2(\rho_p - \rho_f)g}{1650\mu} \qquad (Ar < 33000) \tag{2.26}$$

Eq. (2.26) can be rearranged to obtain the relation between the gravity force and the drag force F'_d acting on one particle layer is given,

$$\frac{\pi}{6}d_p^3(\rho_p - \rho_f)g = 1650\mu\left(\frac{\pi}{6}\right)d_p u_{mf} \equiv F'_d \tag{2.27}$$

If there are n particle layers in a bed, the drag force acting on the lowest level of the bed F_d at the bed breakage is n times as large as the drag force acting on one particle layer F_d'. Thus we have:

$$F_d = n \cdot F'_d \tag{2.28}$$

$$n \approx L_f / d_p \tag{2.29}$$

Taking into account the drag force F_d for n particles in a vertical alignment, the gravity force and the cohesion force F acting on one contacting point at the bed breaking velocity, we obtain:

$$n \cdot 1650\mu\left(\frac{\pi}{6}\right)d_p u_{bb} = n \cdot \frac{\pi}{6}d_p^3(\rho_p - \rho_f)g + F . \tag{2.30}$$

On the other hand when gas velocity is decreased, the bed remains fluidized until u_0 becomes equal to u_{mf} which is given by Eq. (2.26). Substituting Eq. (2.26) into Eq. (2.30) and rearranging it for u_{bb}, we have

$$u_{bb} = \frac{F}{1650(\pi/6)n\mu d_p} + u_{mf} . \tag{2.31}$$

To predict u_{bb}, F is calculated from Eq. (2.19) with x from Eq. (2.15) and σ_{neck}. In this work the observed values of u_{bb} is substituted into Eq. (2.31) to determine F and, accordingly, σ_{neck}.

2.3.1.5 Estimation of the Force Caused by a Bubble

In order to roughly estimate the force acting on one particle from a passing bubble, the following model, which is also illustrated in Fig. 2.7, is developed. From the predicted bubble diameter, the bubble buoyancy force can be estimated. During bubble rise this buoyancy force acts on N particles in the periphery of the bubble. Since the bubble buoyancy force acting on one particle F_b[N] should be in the order of the total buoyancy force divided by the number of particles N in a horizontal circle around the bubble, we obtain the following equations:

$$F_b \approx F_{buoy} / N \tag{2.32}$$

$$F_{buoy} = (1 - \varepsilon_{mf})\rho_p g V_b \tag{2.33}$$

$$N \approx \pi D_b / d_p \quad [-] \tag{2.34}$$

where D_b is the bubble diameter [m], F_{buoy} is the bubble buoyancy force [N], g is the gravity acceleration [m/s²], V_b is the bubble volume [m³], ε_{mf} is the bed voidage at minimum fluidizing condition [-] and ρ_p is the particle density [kg/m³].

2.3.2 Experimental

The experiments were carried out in a fluidized bed shown in Fig. 2.8, which consisted of a column of 43mm i.d. and 430mm long. A perforated plate (ϕ 0.6mm, 61 holes) was used for the distributor. The pre-reduced steel shot particles (SB-2, Sinto-brador, Nagoya, Japan, diameter : 200μm) were used as particles. A semi-conductor pressure sensor (COPAL P-3000S-501D-02) was used for ΔP measurements.

2.3.2.1 Observation of Contact Points

The pre-reduced steel shot particles were placed in a container (5 x 5 mm) made from platinum gauze to form a particle mono layer for the observation of contacting points between particles. Samples were treated in a furnace in hydrogen
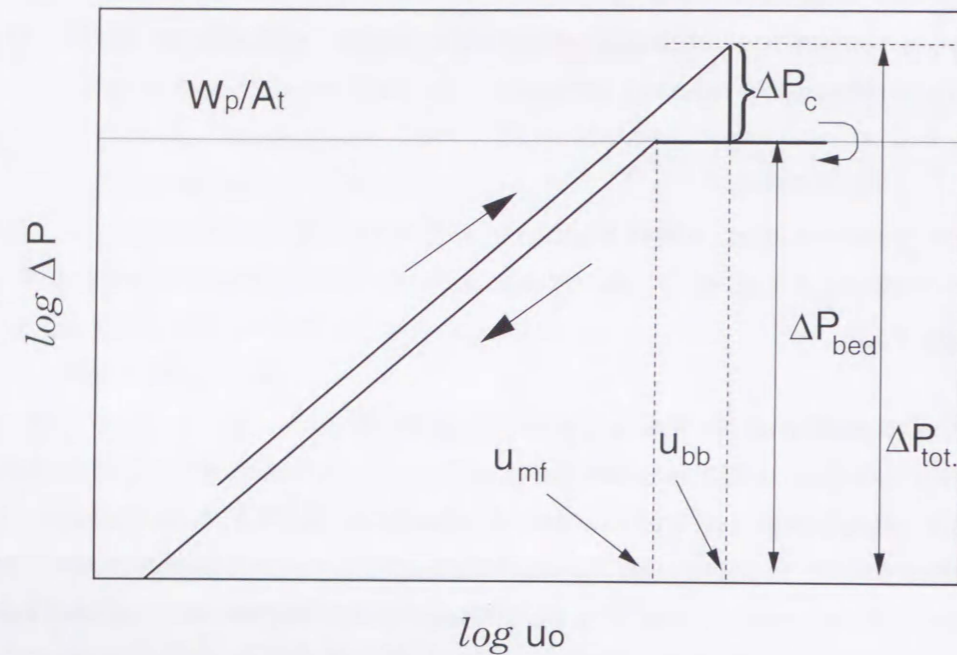
Fig. 2.6   Variation of fluidization curve for sticky particles.
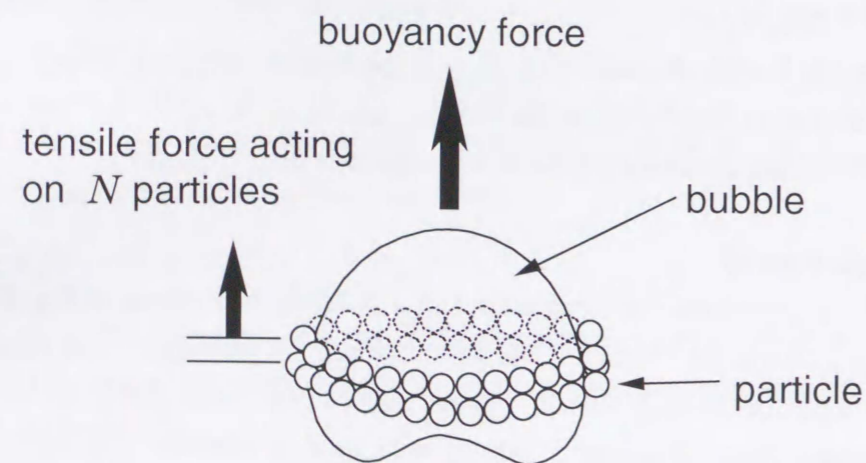

Fig. 2.7   Buoyancy force and tensile force acting on particles in a fluidized bed.

atmosphere at a specified temperature for an hour.   After samples were cooled down, contact points were observed directly using a Scanning Electron Micrograph (SEM) and the neck diameters were measured.

2.3.2.2   Diametral Compression Test

To obtain sintered samples for the diametral compression test, heat treatment of steel shots was performed in a slow hydrogen stream flowing downward in the same apparatus mentioned above for measurement of contact points.   The treatment temperature ranged from 1000 to 1273K.   After the treatment, the bed was cooled down, taken out of the column and cut into disk shaped test pieces (D ~20 mm) whose W/D was adjusted to about 1/2.   The voidage of the test pieces ε was measured by a pycnometer with using helium gas.   The diametral compression test was performed using a commercial testing machine (CATY 2000YH, Yonekura, Osaka, Japan).   The tensile strength of test pieces was calculated by Eq. (2.20), and the cohesion force between particles was estimated by Eq. (2.23).   The cohesion force per unit cross section of a contacting point $F / \pi x_{neck}^2$ was calculated from the observed neck diameter, (ie. $2x_{neck}$).

2.3.2.3   Bed Breaking Velocity

To determine the temperature at which the cohesion force becomes not negligible, the bed pressure drop ΔP was measured at room temperature for heat treated beds.   For this experiment steel shot particles were placed in a column and the static bed height was adjusted to 37mm.   For heat treatment the hydrogen gas was introduced from the distributor.   The superficial gas velocity was kept at a value much less than u_{mf} so that steel shots were heat-treated in a fixed bed condition.   The steel shot bed was kept for an hour at various temperatures in the range from 293 K to 873 K in H_2 gas flow.   After the bed was quenched to the room temperature, bed pressure drop ΔP was measured in the same bed for the flow of N_2 gas.   The fluidization test was performed at room temperature, increasing the gas gradually until the bed was completely fluidized and then decreasing the flow rate gradually to zero.

2.3.3   Cohesion Phenomena of Iron Particles
2.3.3.1   Neck Observation

Typical SEM images of a contact point are shown in Fig. 2.9, where sintered necks between particles can be observed.   These samples were prepared keeping at (a) 923K and (b) 1123K for an hour.   In Fig. 2.10 it is shown how heat treatment
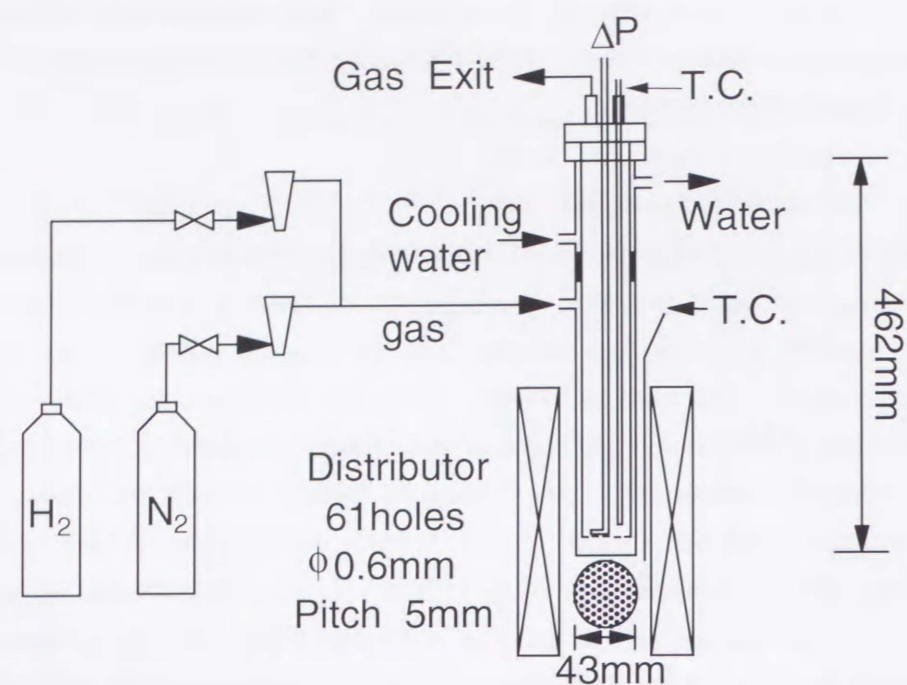
Fig. 2.8   Experimental apparatus for reduction and heat treatment in fluidized bed or fixed bed condition.

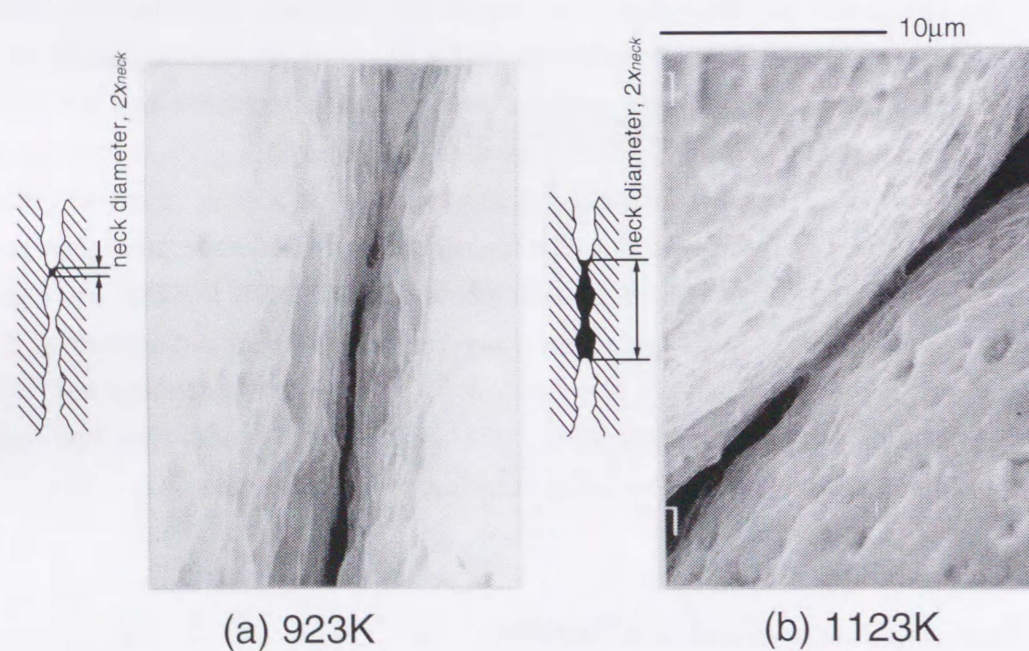(a) 923K   (b) 1123K

Fig. 2.9   SEM images of necks obtained at (a) 923K and (b) 1123K after 3600s contact.

temperature affected the neck diameter. The upper solid line in Fig. 2.10 shows the neck diameter calculated from the Kuczynski's surface diffusion model, Eq.(2.15), where D_s was predicted by Eq. 2.17. In the high temperature region (T > 973K) the observed neck diameters agreed well with those calculated. However, in the low temperature region the observed neck diameters were much smaller than those calculated for $d_p = 200\mu m$. This disagreement is attributed to the roughness of the surface of iron particles at relatively lower temperature (< 973K). Since the curvature radius for surface roughness is much smaller than the particle radius, the surface diffusion rate in the initial period of sintering should be determined by taking into account the surface roughness.

The curvature radius for surface roughness of iron particles was roughly estimated from SEM photographs as $10\mu m$. The lower line in Fig. 2.10 was calculated from the surface diffusion model for $a = 10\mu m$. The neck diameters calculated agreed fairly well with the observed ones. From practical viewpoints the evaluation of surface roughness appears to be an important parameter for estimating the defluidization behavior.

2.3.3.2   Diametral Compression Test

The observed tensile strength S_t of heat treated bed is shown in Fig. 2.11. The tensile strength S_t became stronger when heat treatment temperature increased. For a contacting point, the cohesion force predicted from Eq. (2.23) and S_t data from Fig. 2.11 is shown in Fig. 2.12. The cohesion force of a neck F increased with heat treatment temperature. The cohesion force per unit cross section of a neck $F/\pi x_{neck}^2$ was estimated from the values of F in Fig. 2.12 and average values of observed neck diameters. The results are shown in Fig. 2.13. Below 1200 K, $F/\pi x_{neck}^2$ was almost constant. This implies that the increase of cohesion can be explained by the neck growth due to surface diffusion. $F/\pi x_{neck}^2$ should be equivalent to the tensile strength of a neck σ_{neck}. The value of σ_{neck} determined by bed breaking velocity below 1200K was 20MPa. This value is 1/20 of the tensile strength of the bulk steel shown in Fig. 2.5. Since at low temperature or in the initial sintering period, the neck region was supposed to have contained more lattice defects, the tensile strength of a neck should have been lower than that of the bulk region. On the other hand, $F/\pi x_{neck}^2$ increased above 1200K. This implies an increase of the neck tensile strength. It can be considered as the neck tensile strength would increase with the movement of grain boundary due to volumetric atom exchange caused by the additional contribution of volume diffusion.
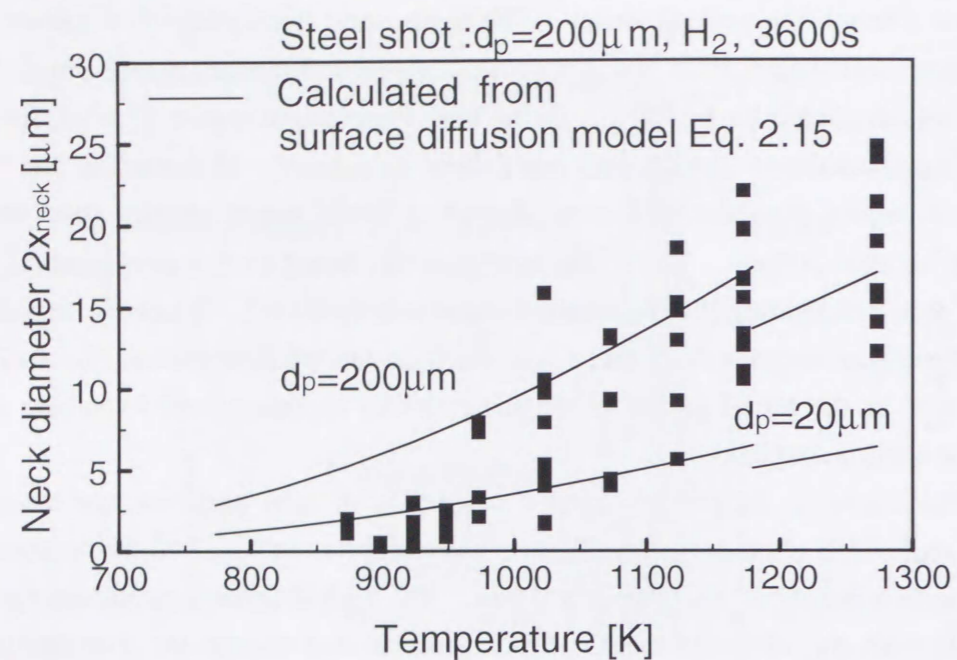
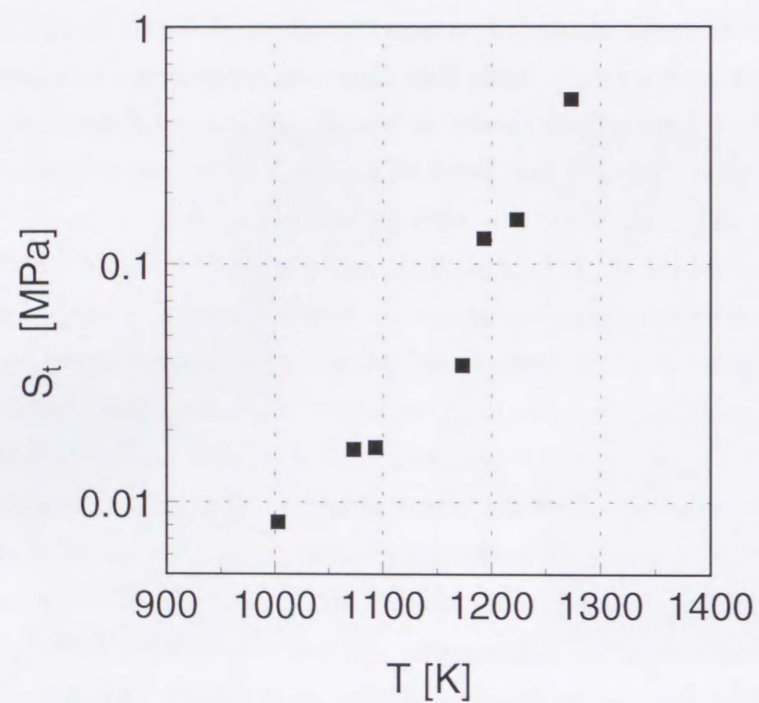Fig. 2.10 Neck diameter determined from SEM images after heat treatment in H_2 atmosphere.

Fig. 2.11 Tensile strength of steel shot beds after heat treatment for 3600s.
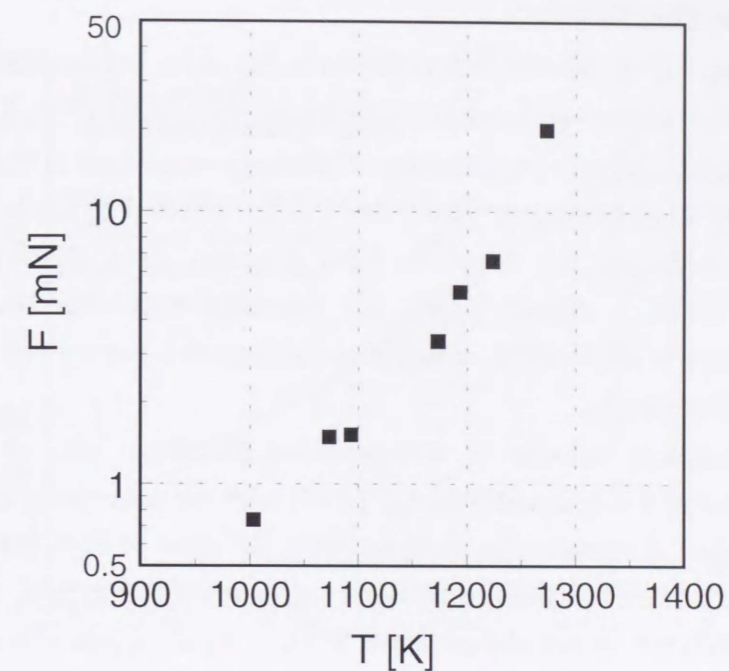
Fig. 2.12 Cohesion force for a contact point determined by Eq.(2.23) as a function of heat treatment temperature.
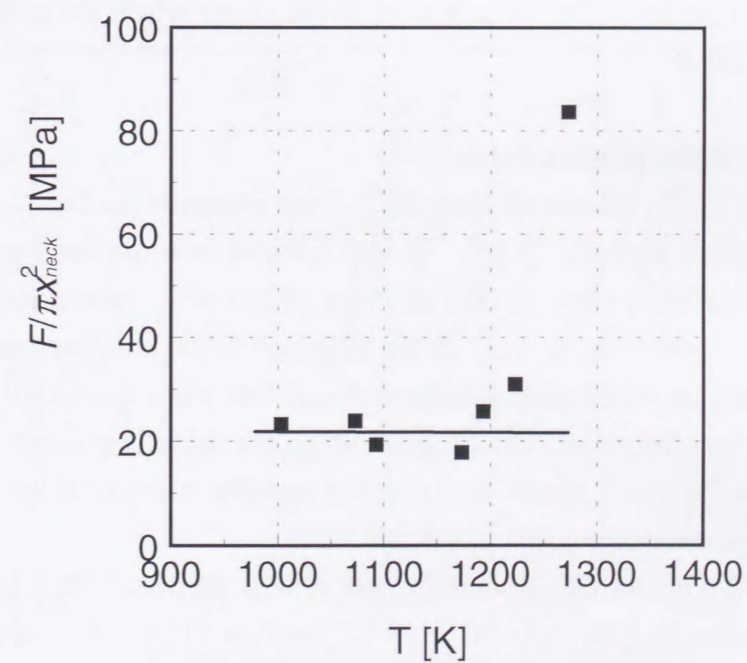
Fig. 2.13 Cohesion force divided by neck cross section area estimated from the surface diffusion model Eq. (2.19) a function of heat treatment temperature.

2.3.3.3 Bed Breaking Velocity

A typical u_0 - ΔP curve obtained is shown in Fig. 2.14.   The effect of the heat treatment temperature on the bed breaking velocity, u_{bb}, is shown in Fig. 2.15.   When the heat treatment temperature was below 723K, u_{bb} was equal to the minimum fluidization velocity u_{mf} at room temperature and was not affected by the heat treatment temperature.   Accordingly, the cohesion force between steel shots was almost negligible below 723K.   Above 773K, u_{bb} increased with the heat treatment temperature.   Moreover above 923K, it was even difficult to break the bed by gas flow and it was unable to obtain u_{bb}.

The bed breaking velocity u_{bb} was predicted for 200μm steel shot from Eq. (2.31) with the value of F calculated from Eq. (2.19) with the assumption of $\sigma_{neck} = \sigma_t = $ 400MPa for bulk steel at room temperature and with the value of neck radius obtained from Eq. (2.15) for surface roughness $a = 10$μm.   As shown in Fig. 2.15, predicted u_{bb} largely disagrees with the observed data above 573K.   As discussed above the tensile strength of a neck σ_{neck} should have been lower than that of the bulk region σ_t. Assuming that the tensile strength of a neck σ_{neck} is 20MPa, the calculated bed breaking velocity u_{bb} roughly agrees with the observed data.   This value of 20MPa agrees with the value of 20MPa obtained from the diametral compression test.

The temperature 773K at which the bed breaking velocity start increasing almost agreed with the lower limit temperature 873K above which the neck formation was confirmed by SEM.

2.3.3.4 Model of Fluidization Behavior

Buoyancy forces calculated from Eq. 2.7 are compared in Fig. 2.16 with the cohesion force predicted by Eq. (2.19).   In this calculation it has been assumed that below 948 K the curvature radius in Eq. (2.15) is 10 μm which also accounts for the surface roughness.   Since above 1173 K the cohesion force is almost always larger than the bubble buoyancy force, defluidization should take place quite easily.   Around 773 K the bubble buoyancy force can be greater than the cohesion force for about 100 seconds.   Even in the initial period, sintering can proceed in the dead space or in the region where the bubble frequency is less than 0.01Hz.

Fig. Fig. 2.6 shows the pressure drop of a steel shot bed ($D_t = 0.043$m, $L_f = $ 0.08m) fluidized with H_2 / N_2 (3:1) gas ($u_0 = 0.24$m/s) at 773K.   For these operating conditions the bubble diameter at the height of L_f / 2 was estimated by Mori - Wen correlation [29] as 0.019m ($D_{b0} = 0.0075$m, $D_{bm} = 0.055$m).   It can be seen that the pressure drop gradually decreased from the beginning, and the pressure fluctuation due to bubbling almost ceased at 3000s.   The force balance in Fig. 2.16 corresponding to t
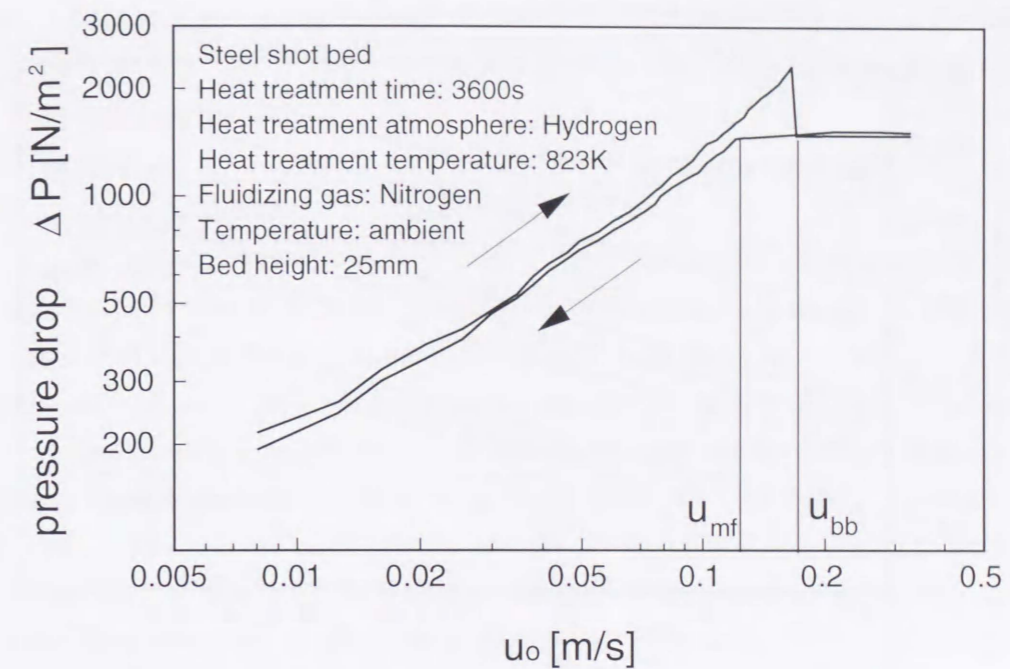

Fig. 2.14   Typical experimental curve of bed breakage and fluidization behavior by gas flow of a heat treated bed.
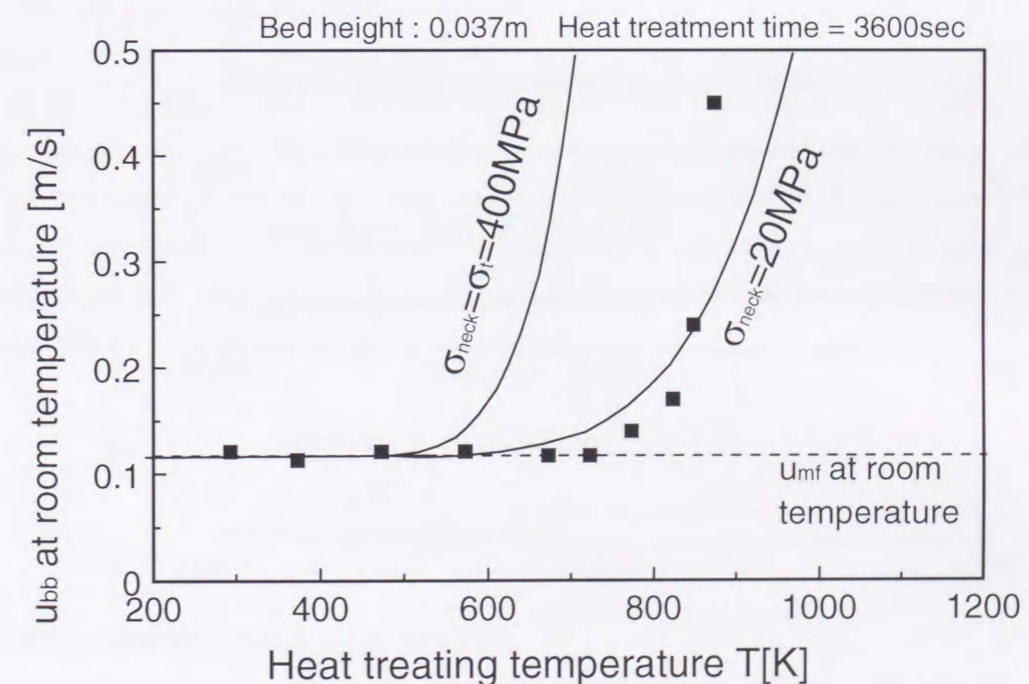

Fig. 2.15   Effect of heat treatment temperature on the bed breaking velocity.
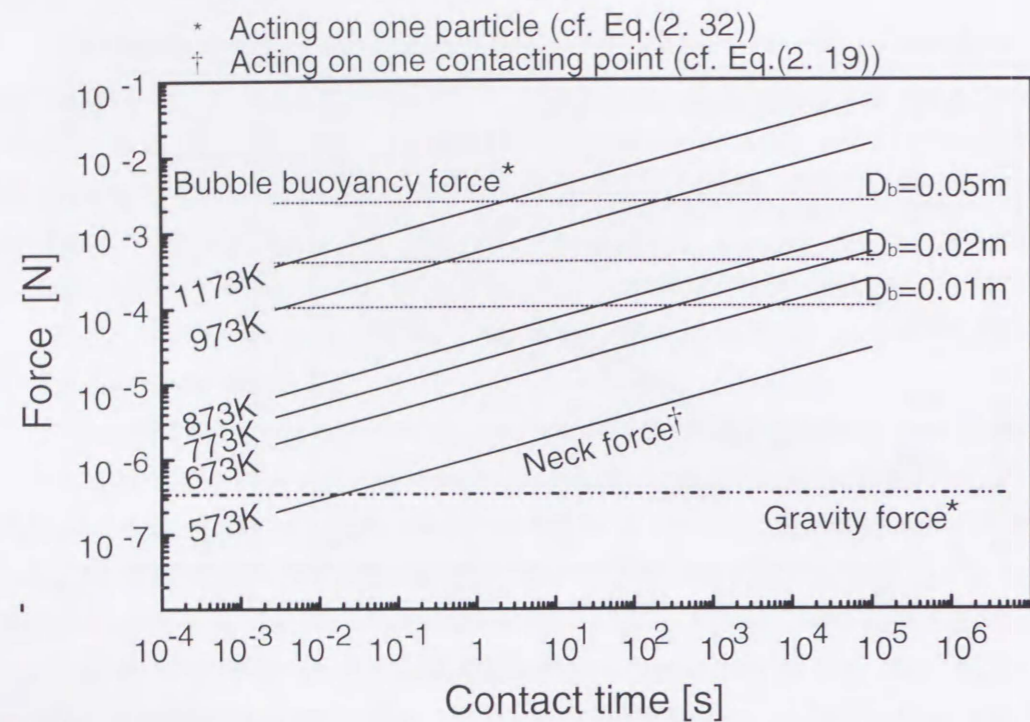
Fig. 2.16   Prediction of forces acting in a fluidized bed as a function of particle-to-particle contact time, bubble diameter and temperature.
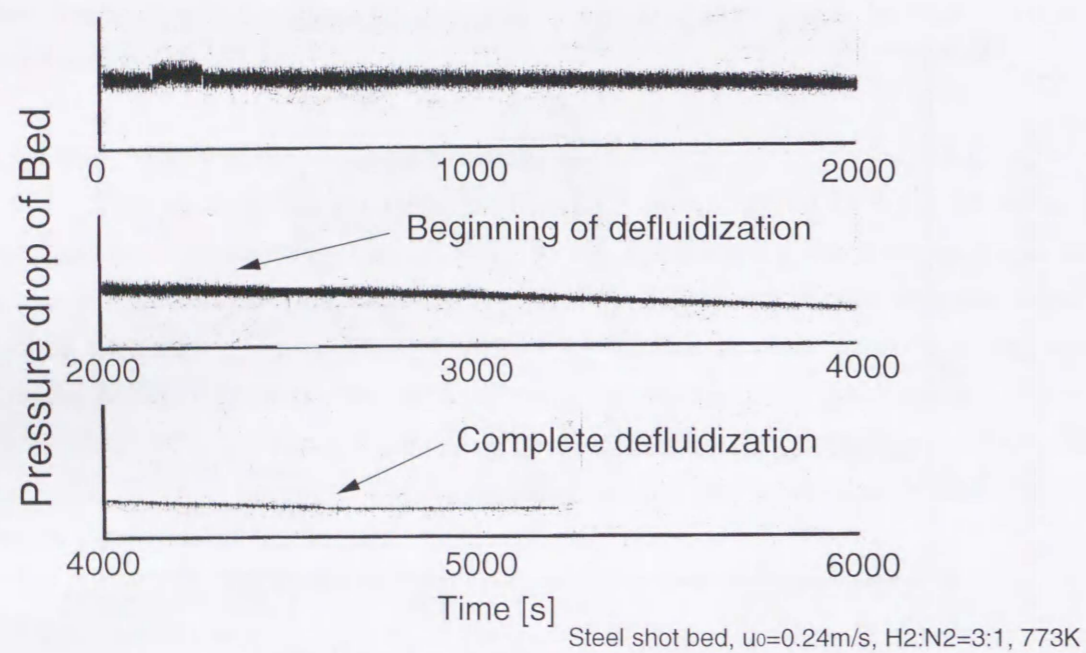

Fig. 2.17   Variation of bed pressure drop for steel shot fluidized bed by an experiment.

= 3000s indicates that the neck force is always larger than one half of the buoyancy force.   The bed was completely defluidized before 4500s because of no pressure fluctuation in Fig. 2.6.   Thus, the observation of Fig. 2.6 roughly agrees with the criterion based on Fig. 2.16.

2.4   CONCLUSIONS OF CHAPTER 2

Regression expressions for liquid bridge force and the critical rupture distance of neck formed between particles as well as between particle and wall, as a function of dimensionless liquid bridge volume ($1.0 \times 10^{-2} \sim 1.0 \times 10^{-5}$), distance between surface and contact angle ($\theta = 0 \sim 50°$), were developed based on the Laplace-Young equation.

Experimental investigation was carried out to determine solid bridge forces for a typical case of iron particles at high temperature and the following results were obtained.   The observed neck growth process below 1173 K was found to agree with the prediction by the surface diffusion model.   The cohesion force between iron particles depended also on particle-particle contact time as shown in Eq. (2.15).   The cohesion force of iron powder was measured by the diametral compression test and σ_{neck} was determined as 20MPa.   The bed breaking velocity u_{bb} of iron particles, which was equal to minimum fluidization velocity u_{mf} at temperatures below 723K, increased steeply with temperatures above 773 K.   The cohesion force due to solid bridge force can be described as a function of neck area and neck tensile strength.   The tensile strength of neck, σ_{neck}, predicted from the bed breaking velocity data below 1173K was about 20MPa, which agreed well with the data obtained from the diametral compression test.   Defluidization behavior was discussed based on the balance of force due to bubble buoyancy force and the neck tensile strength predicted by the surface diffusion model.   The defluidization behavior was discussed based on the balance of force due to bubble buoyancy and tensile force of neck.   The predictions have been successfully confirmed by the experiment.

REFERENCES

1) Fisher, R. A., On the capillary forces in an ideal soil; correction of formulae given by W. B. Haines. *J. Agric. Sci.* **16** (1926) 492

2) Mason, G. and Clark, W. C., Liquid bridge between spheres, *Chem. Eng. Sci.*, **20** (1965) 859

3) Ennis, B. J., Li, J., Tardos, G. I. and Pfeffer, R., The influence of viscosity on the strength of an axially strained pendular liquid bridge. *Chem. Eng. Sci.*, **45** (1990) 3071

4) Lian, G., Thornton, C. and Adams, M. J., A theoretical study of the liquid bridge forces between two rigid spherical bodies. *J. Colloid Interface Sci.* **161** (1993) 138

5) Hotta, K., Takeda, K. and Iinoya, K., The capillary binding force of a liquid bridge. *Powder Technol.* **10** (1974) 231

6) Mazzone, D. N., Tardos, G. I. and Pfeffer, R., The effect of gravity on the shape and strength of a liquid bridge between two spheres. *J. Colloid Interface Sci.* **113** (1986) 544

7) Erle, M. A., Dyson, D. C. and Morrow, N. R, Liquid bridges between cylinders, in a Torus , and between spheres. *AIChE J*, **17** (1971) 115

8) De Bisschop, F. R. E., and Rigole, W. J. L., A physical model for liquid capillary bridges between adsorptive solid spheres: the nodoid of plateau. *J. Colloid Interface Sci.* **88** (1982) 117

9) Endo, Y, Y. Kousaka and Y. Nishie, *Kagakukouga-kuronbunsyu*, **19** (1993) 55

10) Agarwal, J. C. and W. L. Davis, Jr., *Chem. Eng. Prog. Symp. Ser.*, **62**, No.67 (1966) 101

11) Grandsen, J. F., J. S. Sheasby and M. A. Bergougnou, *Chem. Eng. Prog. Symp. Ser.*, No. 105, **66** (1070) 208

12) Kondo, S., N. Miyasaka and T. Sugiyama, "The Direct Reduction of Fine Iron Ores in a Self-Agglomerating Fluidized Bed," *Tetsu to Hagane*, **53** (1967) 22

13) Langston, B. G. and F. M. Stephen, Jr., "Self-Agglomerating Fluidized Bed Reduction," *J. Metals*, **12** (1960) 312

14) Kobayashi, M, H. W. Gudenau, W. G. Burchard and H. C. Schaefer, "Fibrous Growth of Iron Precipitates during Reduction of Iron Ores by CO Gas," *Tetsu to Hagane*, **71** (1985) 44

15) G. C. Kuczynski, Trans. AIME, **185** (1949) 169.

16) A. L. Pranatis, L. S. Castleman and L. Siegel, in W. Leszynski (ed.), *Powder Metallurgy,* Interscience, (1961) 53

17) H. Fischmeister, and R. Zahn, in H. H. Hausner (ed.), *Mod. Dev. Powder Metallurgy: 2,* Plenum Press (1966) 12

18) G. Matsumura, *Acta Metallurgica*, **19** (1971) 851

19) G. Tardos, D. Mazzone and R. Preffer, *Can. J. of Chem. Eng.*, **63** (1985) 377

20) H. Rumpf, K. Sommer and K. Steier, *Chem. Ing. Techn.* **48** (1976) 300

21) J. Kucera, B. Million, J. Ruzickova, V. Foldyna and A. Jakobova, *Acta Metallurgica*, **2** (1974) 135

22) H. W. Mead and C. E. Birchenall, *Trans. AIME*, **206**, 1336 (1956)

23) Kouhan Manual, The Iron and Steel Institute of Japan (1969) 18

24) T. Akazawa, *J. Japan Soc. Civil Engrs,* **29** (1943) 777

25) H. Rumpf, *Chem. Ing. Techn.*, **42** (1970) 538

26) W. O. Smith, P. D. Foote and P. F. Busang, *Physic. Rev.* **34** (1929) 1271

27) K. Nishii and M. Horio, *Kagaku Kougaku Ronbun-syuu*, **20** (1994) 387

28) Wen, C. Y. and Y. H. Yu, 'A generalized method for predicting the minimum fluidization velocity,' *AIChE J.*, **12** (1966) 610

29) S. Mori and C. Y. Wen, *AIChE J.*, **21** (1975) 109

CHAPTER 3

DEVELOPMENT of SAFIRE MODEL and ANALYSIS OF COHESIVE POWDER FLUIDIZATION

CHAPTER 3

DEVELOPMENT of SAFIRE MODEL and ANALYSIS of COHESIVE POWDER FLUIDIZATION

3.1   INTRODUCTION

The importance of cohesive powder fluidization has been recognized by industrials and academics. It is now necessary to analyze the cohesive force of different kinds and to construct a mechanistic model taking into account all mechanical events that take place in fluidized beds. The numerical approach, has become recently quite popular in particle technology and it is a powerful tool to investigate in detail the various phenomena in fluidized beds of cohesive particles. No report has been published to date on the numerical simulation of cohesive powder fluidization because the simulation of dry non-cohesive powders has been the major subject of interest during the past few years.

The ability and the possibility for the direct numerical simulation of the cohesive fluidized bed by a SAFIRE model (Simulation of Agglomerating Fluidization for Industrial Reaction Engineering) was investigated taking into account the liquid bridge and the solid bridge forces which have been already discussed in Chapter 2.

3.2   DEVELOPMENT OF SAFIRE MODEL

3.2.1   Assumptions

The assumptions are enumerated as follows,

1.   Gas is inviscid except for fluid-particle drag force.

2.   The soft sphere interaction of particles consists of a linear spring (Hooke type) and a dash pot (Fig. 3.1) have been assumed allowing multiple particle contact and a Coulomb type friction condition has been also postulated like Tsuji et al.[1].

3.   In order to take into account the cohesion forces another spring, dash pot and rupture joint have been introduced into Hooke type particle contact and interactions in a series.

4.   Particles are spherical in shape and uniform in diameter.

5.   The bed is a two-dimensional fluidized bed having thickness equivalent to one particle diameter with frictionless front and back walls as assumed for the SAFIRE model. On the contrary, the SAFIRE 3D model for three-dimensional object takes into account every frictional wall.

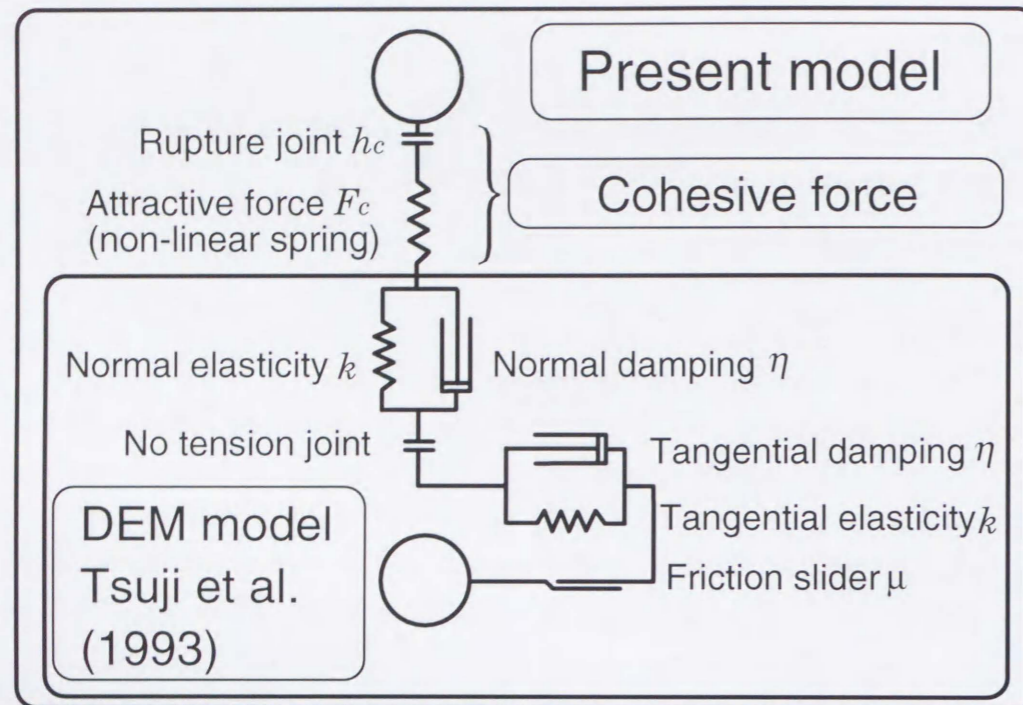The main program routine of SAFIRE model consisted of four parts, viz. i) voidage

Fig. 3.1 Particle interaction model for cohesive powder fluidization
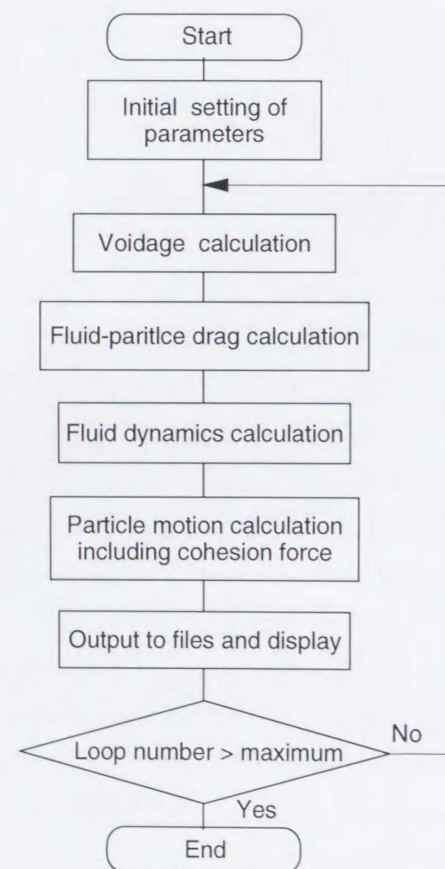

Fig. 3.2 Computing logic flow chart for development of SAFIRE model

calculation, ii) fluid-particle drag calculation, iii) fluid dynamic calculation and iv) particle motion. The flowchart of the SAFIRE model is shown in Fig. 3.1

3.2.2 Governing Equations and Algolithm

Voidage calculation

The voidage is defined at the center of each fluid cell (Fig. 3.3) and calculated from the ratio of the cell volume to the volume not occupied by the particles (Eq. 3.1).

$$\varepsilon = \frac{\delta x \delta y \delta z - \sum V_p}{\delta x \delta y \delta z} \qquad (3.1)$$

As the voidage significantly affects the fluid behavior, the volume of particles has been determined carefully. The volume of a particle located on the border of the fluid cell is divided into several parts.

Fluid-Particle Interaction

For a cell being in a dense condition ($\varepsilon < 0.8$), the well known pressure drop equation of Ergun[2] is used to estimate the force acting on a fluid cell, F_i (Eq. 3.2).

$$F_i = \left(150 \frac{(1-\varepsilon)^2}{\varepsilon} \frac{\mu_f (\mathbf{u} - \overline{\mathbf{v}})}{d_p^2} + 1.75(1-\varepsilon) \frac{\rho_f (\mathbf{u} - \overline{\mathbf{v}}) |\mathbf{u} - \overline{\mathbf{v}}|}{d_p} \right) \delta x \delta y \delta z , \qquad (3.2)$$

where μ_f is the gas viscosity, $\mathbf{u}$ is gas velocity and $\overline{\mathbf{v}}$ is the average particle velocity in a fluid cell. The force, F_{pi}, acting on a single particle in that fluid cell, is obtained using F_i and effective buoyancy force as follows:

$$F_{pi} = F_i / n - \frac{dp}{dx} V_p = \frac{F_i}{\varepsilon n} . \qquad (3.3)$$

where n is number of particle in a fluid cell and V_p is volume of a particle. For a cell being in a dilute condition ($\varepsilon > 0.8$) the modified Stokes type single particle drag force (Wen-Yu[3]) is used for the force $F_{pi, l}$ acting on particle l in a cell i.

$$F_{pi,l} = \frac{\pi}{8} C_D' \rho_f \varepsilon^2 (\mathbf{u} - \mathbf{v}_l) |\mathbf{u} - \mathbf{v}_l| d_p^2 \qquad (3.4)$$

$$C_D' = \varepsilon^{-4.65} C_D \qquad (3.5)$$

$$C_D = \frac{24}{Re} \left(1 + 0.15 Re^{0.687}\right) \quad Re < 1000$$

$$= 0.44 \qquad\qquad Re \geq 1000 \qquad (3.6)$$

Where, $Re = (\rho_f \varepsilon d_p |\mathbf{u} - \mathbf{v}_l|) / \mu_f$, d_p is the particle diameter, C_D is the drag coefficient for an isolated single particle, C_d' is the modified drag coefficient, and $\mathbf{v}_l$ is the velocity of particle l. The summation of the force acting on all particles ($l = 1 \sim n$) in a fluid cell i is adopted for $\mathbf{f}_i$ in the fluid dynamic calculation.
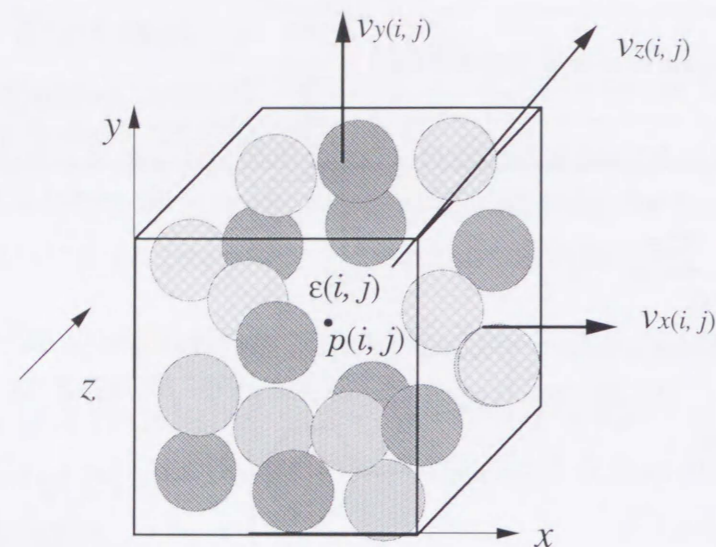
$v_y(i, j)$

$v_z(i, j)$

y

$\varepsilon(i, j)$

$\cdot p(i, j)$

$v_x(i, j)$

z

x

Fig. 3.3 Variables defined for a cell

$$F_i = \varepsilon \sum_{l=1}^{n} \frac{\pi}{8} C'_{Dl} \rho_f \varepsilon^2 (\mathbf{u} - \mathbf{v}_l) |\mathbf{u} - \mathbf{v}_l| d_p^2 \tag{3.7}$$

Fluid Phase

In two fluid models particles are assumed as a continuum like a fluid, and local Navier-Stokes equation are solved not only for fluid but also particle phase.   Navier-Stokes equation for a single phase is defined at every point.   In reality, the equation of motion for a multi-phase cannot be defined at every point of the system because in the gas or particle quantities of the opposite phase can not exist.   Relating point values to locl averaged values Anderson and Jackson[4] derived the local averaged Navier-Stokes equation for multiphase flow.   The point values of voidage, velocity and pressure were averaged over a region where scale is sufficiently larger than the particle diameter and smaller than the bed scale.   The local averaged voidage and the local averaged velocity are defined as follows:

$$\varepsilon(\mathbf{x}, t) = \int_{V_{f\infty(t)}} g(\mathbf{x} - \mathbf{y}) dV_y \tag{3.8}$$

$$\varepsilon(\mathbf{x}, t) u(\mathbf{x}, t) = \int_{V_{f\infty(t)}} u'(\mathbf{y}, t) g(\mathbf{x} - \mathbf{y}) dV_y \tag{3.9}$$

where $V_{f\infty(t)}$ is the total volume occupied by fluid at time t, u' is the point value of gas velocity and $g(r)$ is the weight function which is defined for $x > 0$ and have the following properties:

$$\int_{V\infty} g(r) dV = 4\pi \int_0^\infty g(r) r^2 dr = 1. \tag{3.10}$$

In the SAFIRE model the following local averaged equations are used.   These have been derived by local averaging of the point Navier-Stokes equation where the Reynolds stress term and the viscous diffusion term have been neglected assuming that the particle fluid interaction is overwhelming:

Continuity equation:

$$\frac{\partial \varepsilon}{\partial t} + \frac{\partial (\varepsilon u_i)}{\partial x_i} = 0 \tag{3.11}$$

Momentum balance:

$$\rho_f \frac{\partial (\varepsilon u_i)}{\partial t} + \rho_f \frac{\partial (\varepsilon u_i u_j)}{\partial x_i} = -\varepsilon \frac{\partial p}{\partial x_j} - F_i \tag{3.12}$$

where p is the fluid pressure.   The SIMPLE (Semi-Implicit Method for Pressure-Linked Equations) scheme of Patanker[5] is adopted to solve the equations (Eq. (3.11) and (3.12)) iteratively.   The detailed equations for coding are shown in APPENDIX A.

Particle Motion

Motion of each particle is expressed by the Newton's equation of motion as follows:

for transnational motion

$$m\frac{dv}{dt} = F_{pi} + mg + F_{collision} + F_{wall} + F_{cohesive},$$ (3.13)

for rotational motion

$$I\frac{d\omega}{dt} = M_{collision} + M_{wall} + M_{pi}.$$ (3.14)

where, m is the particle mass[kg], F_{pi} is fluid-particle interaction force acting on a particle[N], g is gravity acceleration[m/s^2], $F_{collision}$ is particle-particle interaction force acing on a particle[N], F_{wall} is particle-wall interaction force acting on a particle[N], $F_{cohesive}$ is cohesion force[N], I is moment of particle inertia[kgm^2], ω is angular velocity [1/s], $M_{collision}$ is moment induced by particle-particle collision[kgm^2/s], M_{wall} is moment induced by particle-wall collision[kgm^2/s] and M_{pi} is moment induced by particle-fluid interaction[kgm^2/s]

Particle interaction

In the SAFIRE model for the particle collision we used a simple model incorporating the principle of Hooke's simple linear spring and dashpot for both normal and tangential components following Tsuji et al.[1] assuming Coulomb's law of friction.

Normal soft sphere interaction force of contact:

$$F_n = k_n \Delta x_n - \eta_n \frac{dx_n}{dt}$$ (3.15)

Tangential soft sphere interaction force of contact:

$$F_t = k_t \Delta x_t - \eta_t \frac{dx_t}{dt} \qquad \text{if } |\mathbf{F_t}| \le \mu|\mathbf{F_n}|$$ (3.16)

$$F_t = \mu|\mathbf{F_n}|\frac{\mathbf{x_t}}{|\mathbf{x_t}|} \qquad \text{if } |\mathbf{F_t}| > \mu|\mathbf{F_n}|$$ (3.17)

The damping coefficient η is determined in terms of the restitution coefficient e. The duration of collision contact td is obtained approximately by solving a simple equation of motion for a spring and mass system as follow:

$$\eta = 2\gamma\sqrt{km}, \quad \gamma = \frac{(\ln e)^2}{(\ln e)^2 + \pi^2}$$ (3.18)

Therefore, particle size, mass and spring constant are the major factors determining the computation burden, except for the total number of particles.

3.2.3 Computation Conditions

Boundary Conditions

Situations of a fluid cell in the calculation domain are distinguished by the value of the cell flag for various boundary conditions including gas nozzles. The boundary conditions were specified for gas flow as follows:

1) The horizontal gas velocity on a sidewall is set to zero.

2) The vertical gas velocity at the bottom plate is set to zero.

3) The inlet gas velocity through an orifice is set at a specified value.

4) Pressure gradient and velocity gradient in the vertical direction are assumed at zero in a topmost cell.

Time Step and cell size

The calculation time step is an important parameter because computation time will be wasted for small time step. On the other hand, for large time step we face numerical instability and end up in unreasonable results. Tsuji et al. [1] investigated that 20% of duration of collision contact T_d is suitable for soft sphere DEM simulations. In the SAFIRE model the same principle is adopted for computation time step.

The duration of collision contact T_d is obtained approximately by solving a simple equation of motion for a spring and mass system as follows:

$$T_d = \pi\sqrt{m/k_n} = \sqrt{(\pi d_p)^3 \rho_p / 6k}$$ (3.19).

Therefore, particle size, mass and spring constant are the major factors determining the computation burden, except for the total number of particles. In The SAFIRE code the particle stiffness is fixed to 800N/m which is smaller than the real stiffness of materials from the viewpoint of computation efficiency. The spring constant affects the maximum overlap distance at every collision. The dimensionless maximum overlap distance $\Delta x/d_p$ is given by the balance between kinetic energy and elastic energy:

$$\Delta x / d_p = (\pi d_p \rho_p / 6k)^{1/2} u_{rel}.$$ (3.20)

Assuming that the particle relative velocity is of the same order of magnitude as superficial gas velocity, we can obatin the apparent Young modulus E_{ap} by using the approximate collision period T_d from Eq. (3.19) and maximum overlap distance from Eq. (3.20) as follows:

$$E_{ap} = k / [\pi d_p \{\Delta x / d_p - (\Delta x / d_p)^2\}]$$ (3.21)

The effect of using quite softened stiffness on simulation results has been discussed in Section 3.2.

The fluid cell size for computation should be carefully determined because the concept of local mean average of fluid characters is failed for too small cell size. On the other hand, for large cell size detail of fluid motion and accuracy are lost. The cell size of $3.5d_p$ is used in the SAFIRE model and the effect of cell size has been also discussed in Section 3.2.

Visualization of calculated results

The calculated result of particle location was displayed on the screen one by one during computation. The files of calculated results were stored in Magneto Optical (MO) 5inch disk (1.3 or 2.6Gbytes). After calculation, the results of particle location, voidage, gas velocity, solid velocity, granular temperature (defined in 3.3) and gas pressure are visualized by AVS (Advanced Visual System) software. To make digital video animations DISKUS (Made in USA) digital video recording system was used.

Initial Conditions

Computations were performed using a workstation (Hewlett Packard HP9000 C110 and C180). To compose the initial static bed, particles were located from the bottom with random location and velocity and were let sediment without fluid-particle interaction. Accordingly, the initial conditions were not exactly same for different conditions of particle-particle interaction.

Outputs

The SAFIRE code can provide the following out put files,

- Location of all particles
- Velocity of all particles
- Voidage map
- Gas pressure map
- Fluid velocity vector map
- Cell averaged particle velocity map
- Granular temperature map
- Bed pressure drop
- Wall pressure caused by particle collisions

3.3 NUMERICAL SIMULATION OF NON-COHESIVE PARTICLES

Numerical simulation of fluidization behavior of non-cohesive powder was carried out with SAFIRE model and the effects of various parameters on the fluidized bed performance were investigated.

3.3.1 Fluidization Behavior of Non-Cohesive Particles

Fig. 3.4 shows typical snapshots of a single bubble rising behavior in a two dimensional (2D) fluidized bed calculated for a non-cohesive powder. Computation conditions are shown in Table 3.1. The fluidized bed was supposed to have a porous plate distributor and one gas inlet nozzle at the center. In this computation the amount of gas necessary for a minimum fluidizing condition was introduced informing at the bottom of the bed and an additional gas was injected through the nozzle to generate a single bubble. The initiate bubble formation, its shape including wake, rising and eruption were all found to be sufficiently realistic.

Recently, the concept of the granular temperature (Chapman and Cowling, 1970[6] has been introduced by the kinetic theory as considered as the key factor concerning the kinetic state of a fluid-particle system. The granular temperature Θ is defined as follows:

$$\Theta = \left(\frac{1}{3}\right)\langle(v - \langle v\rangle)^2\rangle. \tag{3.22}$$

Although it is difficult to measure directly the granular temperature in a fluidized bed by experiment, it is possible to predict it by the discrete element model. In the present work the granular temperature Θ was roughly estimated from the ensemble average of the fluctuation velocity, v - $<v>$, of particles in each fluid cell which can, however, contain on a maximum 14 particles.

In Fig. 3.4 the computed transient behavior of the granular temperature, the bed voidage and the gas pressure for the dry particles are also shown. The high granular temperature area is found both above a forming bubble, and below a rising bubble. The latter indicates that during bubble rising a significant number of particle collisions take place in and around the wake.

Fig. 3.5 shows example of snapshots of the 2D bubbling fluidization behavior as calculated by SAFIRE for a non-cohesive powder (particle diameter: 1mm, density: 2650kg/m^3) at the ambient condition. A fluidized bed was supposed to have six inlet nozzles and the superficial gas velocity chosen was 1.2m/s. Fig. 3.6 shows the bed pressure drop with time when u_0 was changed during fluidization. The bubble formation, coalescence, eruption and particle circulation were all found to be sufficiently realistic. Furthermore, the simulation results are also realistic with respect to the acceleration and elongation of a bubble when it is closely located below another

Table 3.1	Computation Conditions
Particles	
Number of particles	14000
Particle density	$2650kg/m^3$
Particle diameter	$1000\mu m$
Restitution coefficient	0.9
Friction coefficient	0.3
Spring constant	800N/m
Bed	
Bed size	0.154 x 0.3825m
Number of nozzles	6 or 1(for single bubble)
Opening diameter of a nozzle	3.7mm (equivalent to a cell width)
Time step	$2.58 \times 10^{-5}s$ $(1/5T_d)$
Others	
Gas : Air	
Viscosity	1.75×10^{-5} Pa s
Density	$1.15kg/m^3$
Number of cells	41 x 105
Geldart group	D

Time interval: 0.05s   Restitution coefficient: 0.9   Number of fluid cells: 41 x 105
Spring const.: *k*=800N/m   Friction coefficient: 0.3
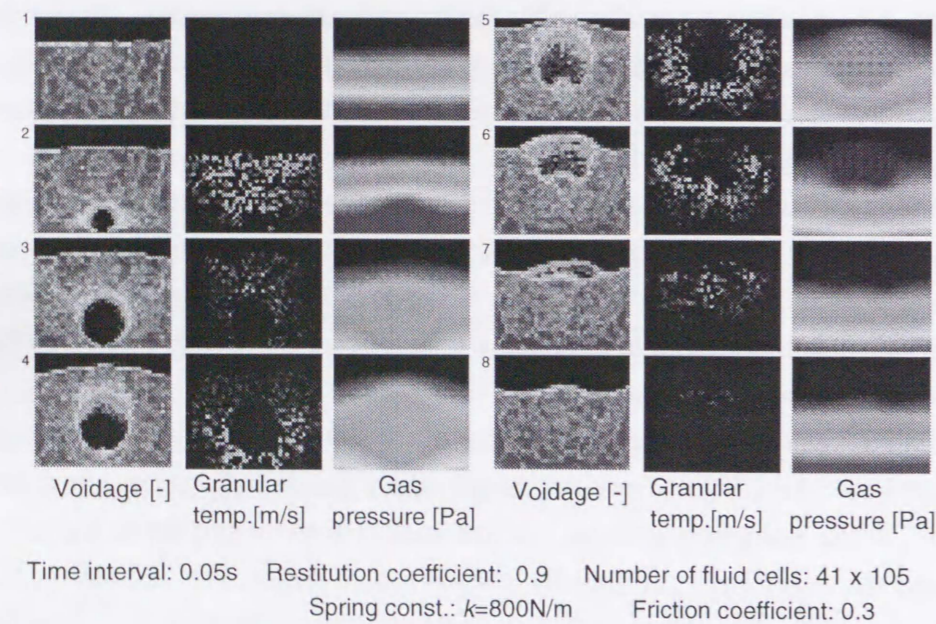
Fig. 3.4 Single bubble rising in a fluidized bed as computed and simulated by SAFIRE
model (Snap shots 1 to 8 are shown for increasing time steps of 0.05s)
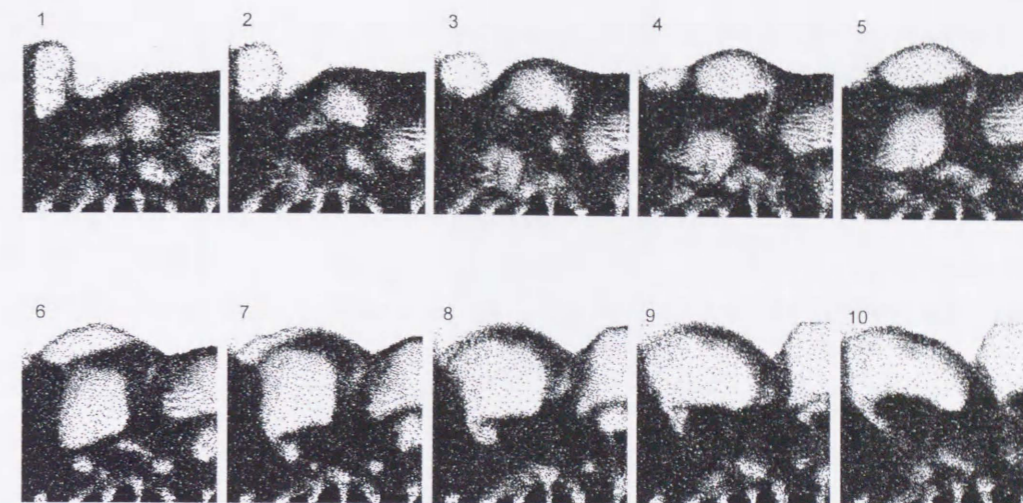
Fig. 3.5 Fluidization behavior of dry (non-cohesive) particles in snapshots (u_0 = 1.2m/s,
d_p = 1.0mm)
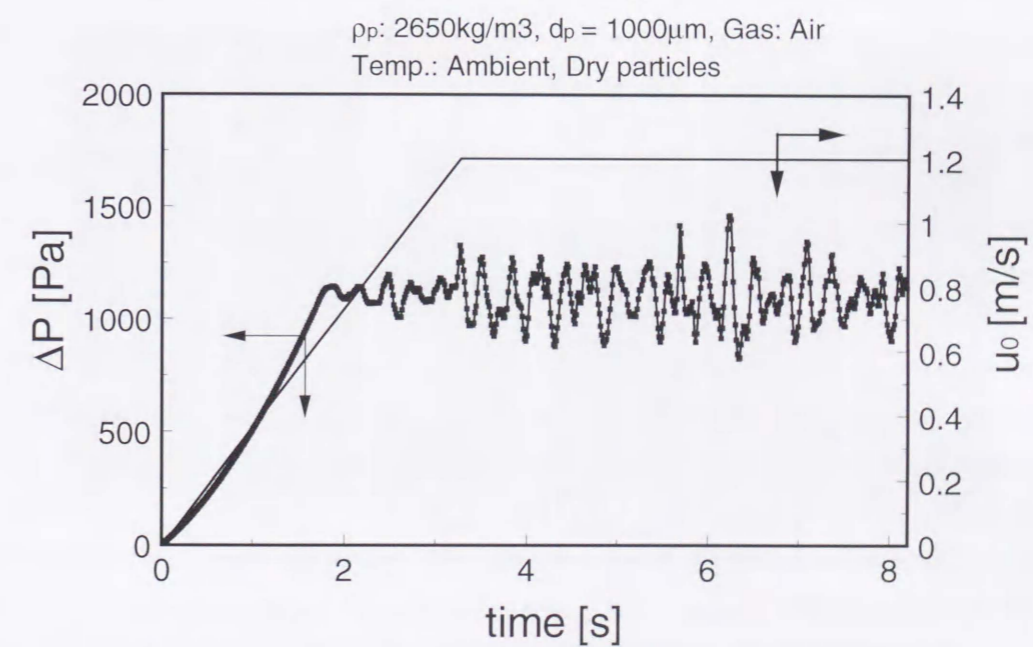
Fig. 3.6 Pressure drop of a bed during fluidization of dry particles

bubble. The "fingering" phenomena, i.e. particle falling in bubbles in the form of fingers or knives, which may correspond to Rayleigh-Taylor instability (Fig. 3.5 10frame).

The minimum fluidization velocity u_{mf} is one of the most important fundamental parameters in fluidization. In order to determine u_{mf} by the computer experiment, the superficial gas velocity u_0 was decreased gradually from 1.2m/s to zero in about 13s. The bed pressure drop was plotted against the superficial gas velocity as delineated in Fig. 3.7. For non-cohesive particles the typical u_0 -ΔP curve was obtained from which u_{mf} was determined at 0.68m/s. The calculated value agreed well with empirically obtained value 0.56m/s by Wen-Yu correlation whose accuracy is within ±30% error.

3.3.2 Effect of Model Parameters on Simulation Results

Now, let us examine the sensitivity of computed results on the model parameters, i.e. cell size, the spring constant and the restitution coefficient. Figs. 3.8 and 3.9 show the bed behavior of the same powder calculated with large fluid cells (number of fluid cells: 21 x 53, size 7.3 x 7.2mm) and small fluid cells (number of fluid cells: 82 x 210, size 1.9 x 1.8mm) respectively. In each condition a fluid cell contains 52 and 3.5 particles in its maximum. As can be seen, the result using small fluid cells is almost similar with Fig. 3.4 (number of fluid cells: 41 x 105, size: 3.8 x 3.6mm), on the other hand, the result using small cells is not reliable as demonstrated by the unreasonable pressure profiles (Fig. 3.9). In principle, the fluid cell should contain more than 10 particles to avoid computational error that would result by improper local averaging of bed properties.

The computations have been carried out varying spring constant, k, from 8 to 80000N/m in steps of 10 times the preceding value and the restitution coefficient, e, was chosen at 0.8, 0.9 and 0.95. These values of k and e have been chosen arbitrarily to achieve computation economy and also to study the influence of these variables on computation time. As has been discussed earlier in Section 3.2.3, the collision time T_d is a function of mass of particle, m, and the spring constant, k. The time interval, Δt, for computation should be sufficiently small to arrive at a meaningful result and it should be less or equal to one fifth of T_d (Tsuji et al. [1]). Apart from total number of particles, computation burden is determined by other major factor such as particle size, its mass and spring constant.

If both duration of contact T_d and maximum overlap distance at collision $\Delta x/d_p$ are sufficiently small in the computation as well as in the real system, parameter k may be rather arbitrarily taken. As long as sufficient collisions between particles exist frequently, they behave like a fluid. Hence the difference in k or restitution coefficient
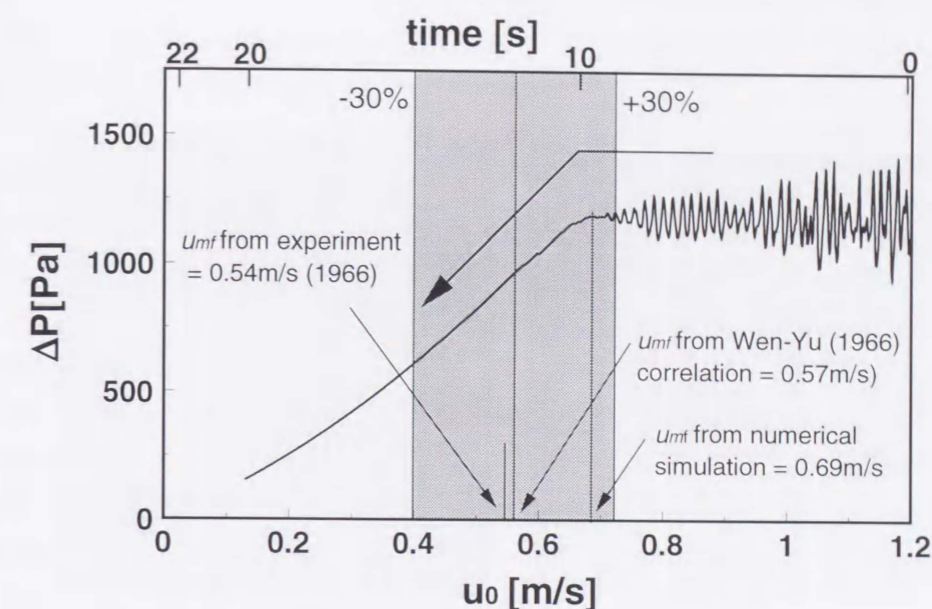

Fig. 3.7 Measurement of minimum fluidization velocity (Shaded area is within ±30% of u_{mf} predicted by Wen-Yu (1966) correlation)
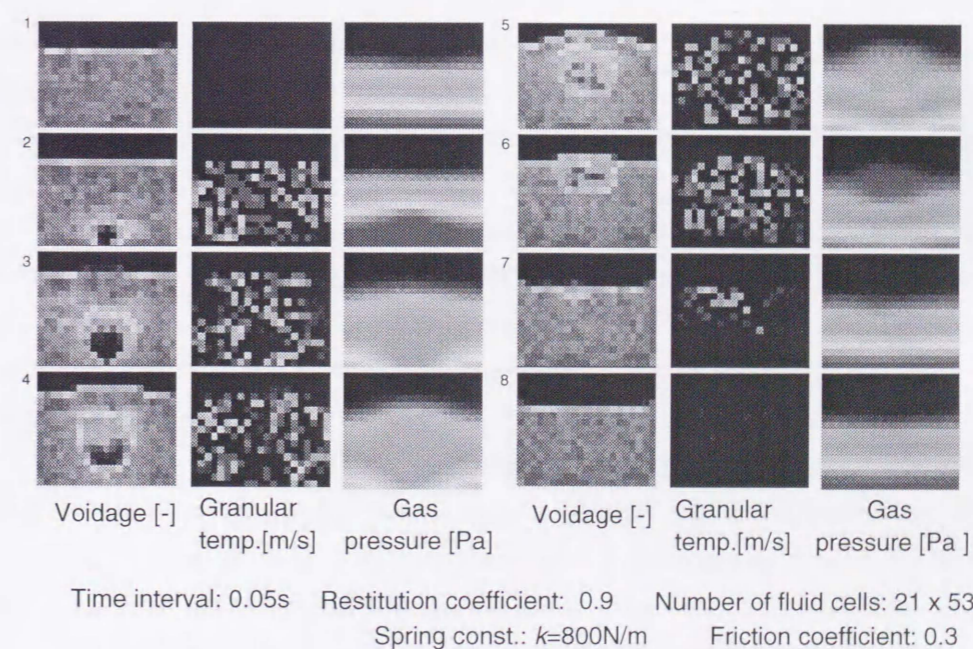

Time interval: 0.05s   Restitution coefficient: 0.9   Number of fluid cells: 21 x 53
Spring const.: k=800N/m   Friction coefficient: 0.3

Fig. 3.8 Single bubble rising in a fluidized bed (Number of fluid cells 21 x 53)

| Voidage [-] | Granular temp.[m/s] | Gas pressure [Pa] | Voidage [-] | Granular temp.[m/s] | Gas pressure [Pa] |

Time interval: 0.05s   Restitution coefficient: 0.9   Number of fluid cells: 81 x 210
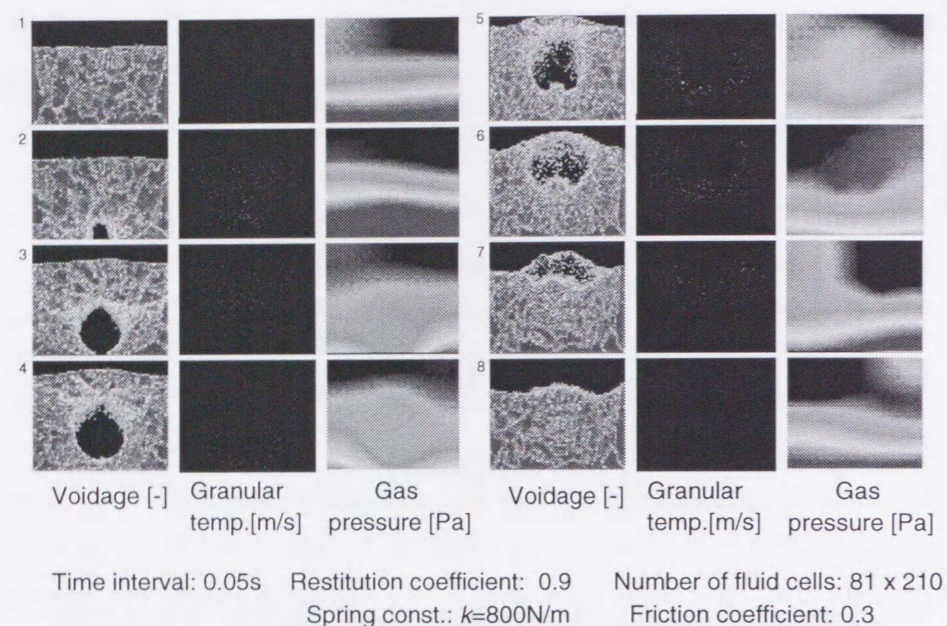Spring const.: k=800N/m   Friction coefficient: 0.3

Fig. 3.9 Single bubble rising in a fluidized bed (Cell size 82 x 210)

e may not affect the meso / macro scale behavior of bed particles and bubbles.   In the lean suspension these parameters may become more important.   This is a matter of particle density, diameter and gravity.

Fig. 3.10 and 3.11 show single bubble rising behavior and bubbling behavior of a fluidized bed having 6 nozzles using spring constant k = 80N/m was used.   In former computation the amount of gas necessary for a minimum fluidizing condition was introduced from the bottom of the bed uniformly and an additional gas was introduced from the center of the bottom periodically to inject single bubbles.   Figs. 3.12 and. 3.13 show those for k =80000N/m which requires 10 times as big CPU time as for k = 800N/m.   Fig. 3.14 shows the calculated pressure drop of the bed for different spring constants.   The calculated pressure fluctuations (Fig. 3.12 and Fig. 3.13) at 80000N/m are not much different from the result for 800N/m (Fig. 3.4 and Fig. 3.5).   The fluidization behavior was also not significantly changed.   However, when k = 80N/m was used, the pressure drop fluctuation is larger than that for k = 800N/m and k = 80000N/m.   In addition to this, when k = 8N/m was used, the computation was not feasible due to the numerical difficulty (unrealistic particle repulsion).

It is now interesting to discuss why in the case of small spring constants the computation became impossible.   Contact duration (Eq. (3.19)), maximum overlap distance (Eq. (3.20)) and apparent Young modulus (Eq. (3.21)) are listed in Table 3.2 for the three cases examined.   Apparently, an overlap distance larger than 10% of particle diameter cause computational troubles (unrealistic repulsion).   When the fluidized bed behavior of much softer particles is to be simulated in the future with taking into account the shape modification of liquid bridges associated with particle deformation, we will have to pay more attention on k, corresponding Young modulus and geometry of multi particle collisions.

The contact periods in all three cases are much smaller than fluctuation time scales of the ordinary bubbling beds (< 100Hz).   This may be another reason why the inter-particle non-cohesive interaction parameters did not affect the bed behavior.   Accordingly, in the present case the reduction of spring constant down to several hundred N/m seems allowable.

Figs. 3.15 and 3.16 are the computed results when friction coefficient is changed from 0.8 to 0 at single bubble rising condition.   The formed bubble diameter was affected by the friction coefficient and small friction coefficient made a large bubble.   It seems that tangential friction has a important role in fluidization.

In order to investigate the effect of restitution coefficient, the pressure drop obtained by computer experiments during fluidization for restitution coefficients 0.8 and 0.95 are shown in Fig. 3.17 in comparison with that of 0.9.   The restitution coefficient was found not to affect the fluidization behavior significantly at least for the fluidization
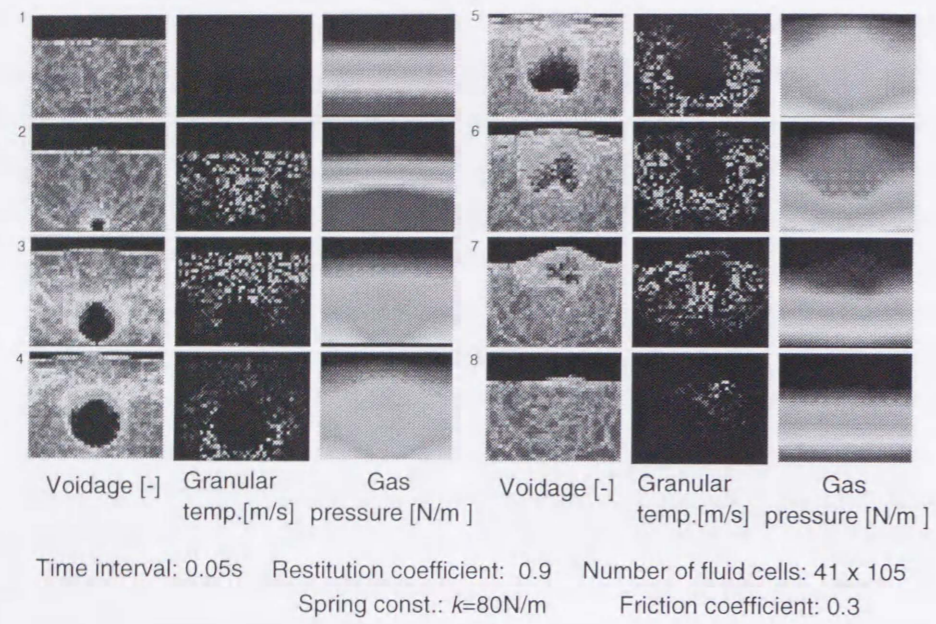
Voidage [-] Granular temp.[m/s] Gas pressure [N/m] Voidage [-] Granular temp.[m/s] Gas pressure [N/m]

Time interval: 0.05s   Restitution coefficient: 0.9   Number of fluid cells: 41 x 105
Spring const.: k=80N/m   Friction coefficient: 0.3

Fig. 3.10 Single bubble rising in a fluidized bed (spring const. k = 80 N/m)

Voidage [-] Granular temp.[m/s] Gas pressure [Pa] Voidage [-] Granular temp.[m/s] Gas pressure [Pa]

Time interval: 0.05s   Restitution coefficient: 0.9   Number of fluid cells: 41 x 105
Spring const.: k=80000N/m   Friction coefficient: 0.3

Fig. 3.12   Single bubble rising in a fluidized bed (spring const. k = 80000 N/m)

Fig. 3.11   Snapshots showing fluidization behavior of dry particles
(spring constant k = 80N/m, timeinterval = 0.0516s)
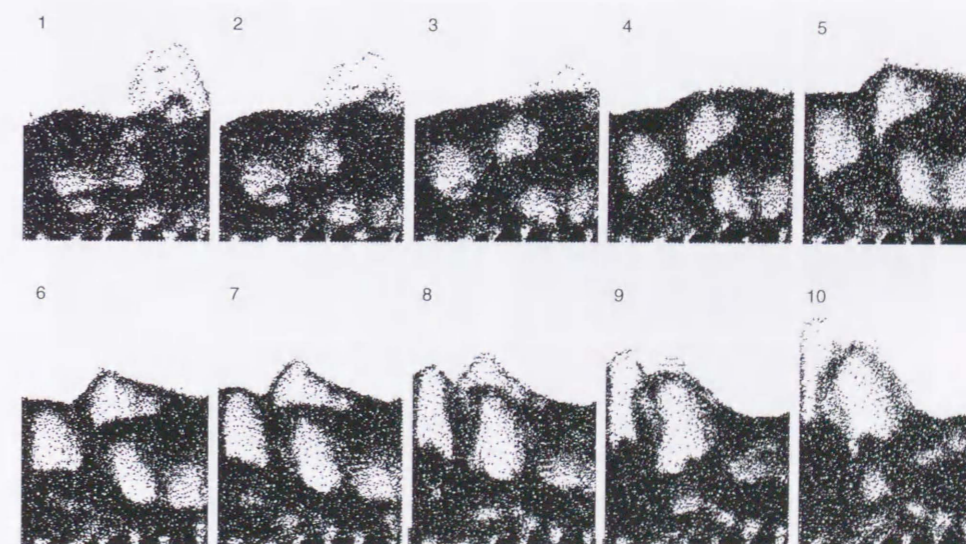
Fig. 3.13   Fluidization behavior of dry particles in snapshots
(spring constant k = 80000N/m, time interval = 0.0516s)
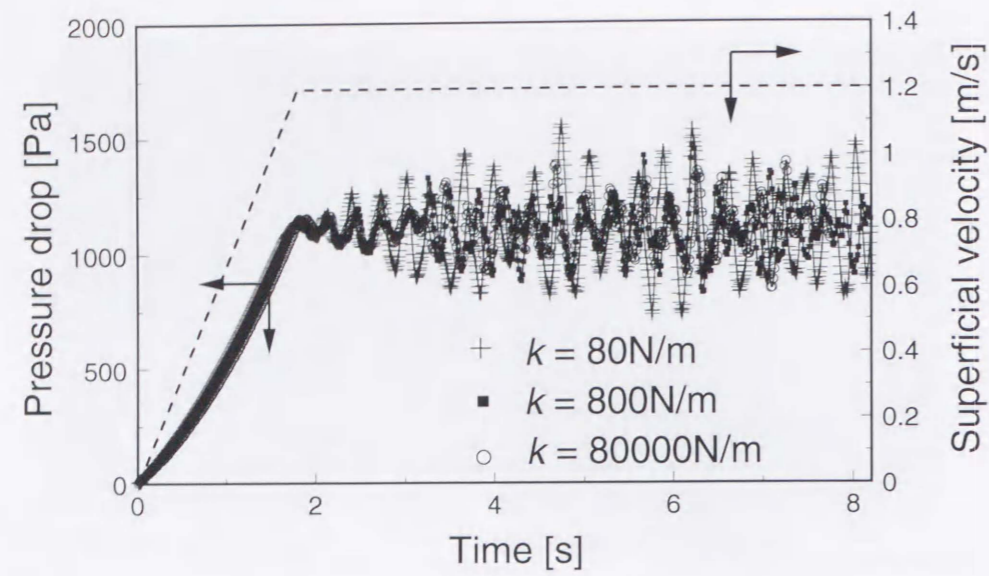
Fig. 3.14   Pressure drop of fluidized beds (spring constant k = 80, 800 and 80000N/m)

Table 3.2 Effect of spring constant

Spring const. k [N/m]	Maximum overlap distance $\Delta x/d_p$ [-]	Apparent Young modulus E_{ap} [N/m^2]	Duration of contact T_d [s]
8	0.42	1.05×10^4	1.30×10^{-3}
80	0.13	2.25×10^5	4.13×10^{-4}
800	0.042	6.33×10^6	1.30×10^{-4}
80000	0.0042	6.09×10^9	1.30×10^{-5}

Assumptions: Particle-particle relative velocity before collision = u_0 (1.0m/s). Apparent Young modulus is calculated assuming that particles are circular rods of the same diameter as the maximum overlap circle.

Voidage [-]   Granular temp.[m/s]   Gas pressure [Pa]   Voidage [-]   Granular temp.[m/s]   Gas pressure [Pa]

Time interval: 0.05s   Restitution coefficient: 0.9   Number of fluid cells: 41 x 105
Spring const.: k=800N/m   Friction coefficient: 0.8
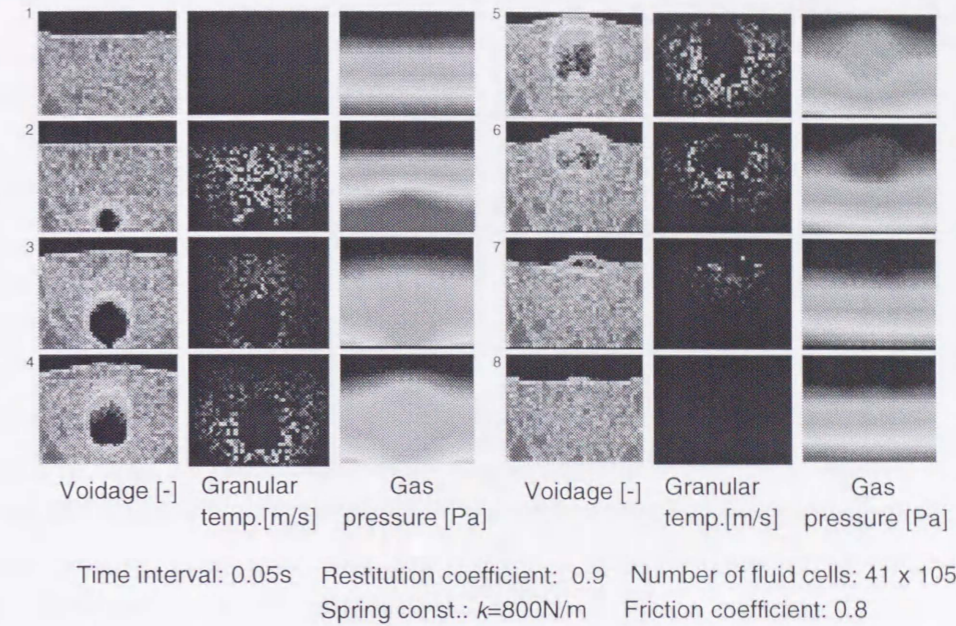
Fig. 3.15   Single bubble rising in a fluidized bed (friction coefficient e = 0.8)

Voidage [-]   Granular temp.[m/s]   Gas pressure [Pa]   Voidage [-]   Granular temp.[m/s]   Gas pressure [Pa]

Time interval: 0.05s   Restitution coefficient: 0.9   Number of fluid cells: 41 x 105
Spring const.: k=800N/m   Friction coefficient: 0.0
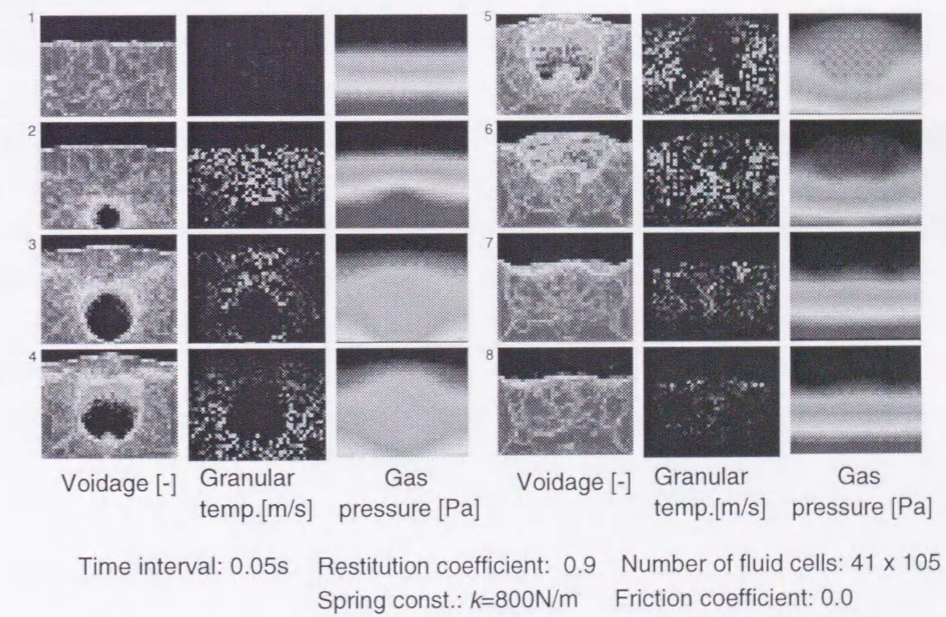
Fig. 3.16   Single bubble rising in a fluidized (friction coefficient μ = 0.0)
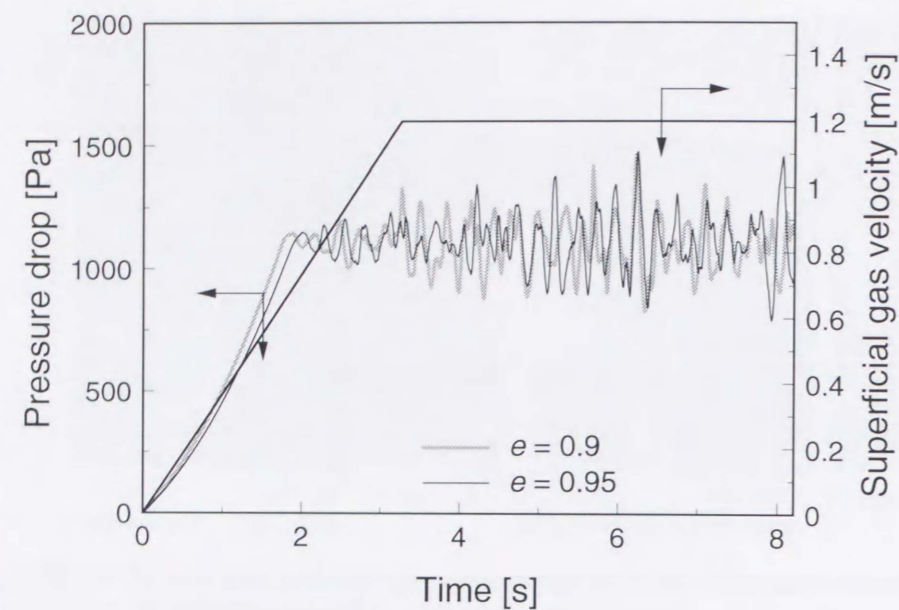
Fig. 3.17   Pressure drop of a fluidized bed for various restitution coefficient *e*
= 0.8, 0.9 and 0.95)

of dry particles.

3.3.3   Fluidization Behavior of Three-Dimentional Fluidized Beds

The numerical simulation, SAFIRE model, has been extended to the three dimensional bed and it is coded as SAFIRE-3D.

Computation conditions

Computations were carried out for the conditions shown in Table 3.3 with a workstation (Hewlett Packard HP9000 C180).   The CPU time required for computation of real 1s was 4.8days for non-cohesive particles.

Fluidization behavior of non-cohesive particles

Fig. 3.18 shows typical snapshots on vertical center cross section of the 3D bubbling fluidization behavior calculated for a non-cohesive powder (particle diameter: 1000μm, density: 2650kg/m^3, bed size 0.050m x 0.050m square cross section) at the ambient condition.   The fluidized bed was assumed to have a porous distributor.   The superficial gas velocity chosen was 1.2m/s.   Bubble formation, coalescence, eruption and particle circulation were all found to be sufficiently realistic.   Fig. 3.19 shows the pressure drop of the bed obtained by computation.   The bed showed slugging behavior because of the small bed cross section.   The minimum fluidizing velocity was obtained by the numerical experiment by decreasing gas velocity as shown in Fig. 3.20.   The u_{mf} is 0.68m/s and close to the same as the one obtained for two-dimensional bed (0.69m/s).

The vertical cross section of the voidage, the granular temperature and the gas velocity vector are shown in Fig. 3.21.   The presence of higher granular temperature region below a bubble was observed in the previous section in a two-dimensional fluidized bed.   In the present case of three-dimensional simulation, the high granular temperature region was also found below a bubble.

Fig. 3.22 shows the solid mixing by a rising bubble.   The particles initially located at the bottom region were colored with black.   The wake particle lifting first found by Rowe et al.[7] can be confirmed obviously in vertical and horizontal cross sections.

Table 3.3 Computation conditions for three dimensional fluidized beds

Particles	A	B
Number of particles	150000	500000
Particle density	2650kg/m³	
Particle diameter	1.0mm	
Restitution coefficient	0.9	
Friction coefficient	0.3	
Spring constant	800N/m	
Bed		
Bed scale	0.05 x 0.05 x 0.12m	0.09 x 0.09 x 0.27m
Number of nozzles	porous or 9	16
Opening diameter	4.2mm	
Number of fluid cells	12 x 12 x 30	21 x 21 x 63
Time step	2.58×10^{-5} s $(= 1/5T_d)$	
Others		
Gas : Air		
Viscosity	1.75×10^{-5}Pa s	
Liquid : Water		
Surface tension	0.073N/m	

Fig. 3.18   Vertical cross sections of fluidization behavior of dry powders in a three dimensional bed (d_p = 1.0mm, ρ_p = 2650kg/m³, u_0 = 1.2m/s)
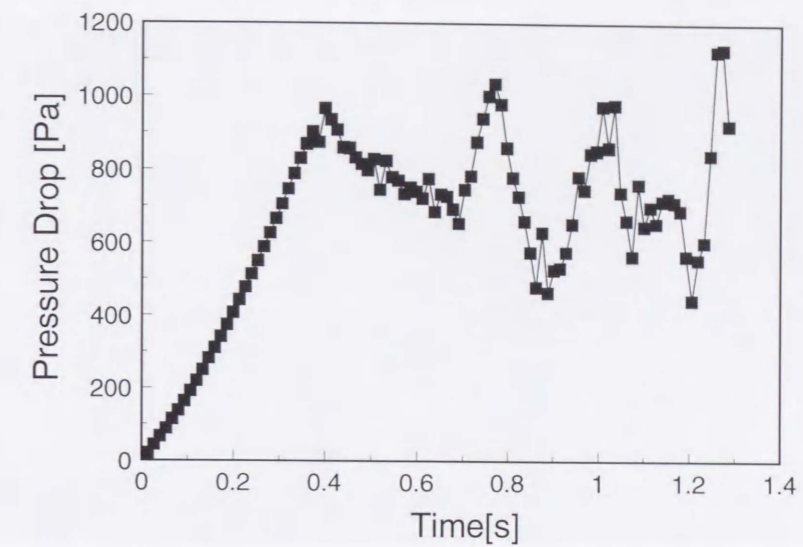
Fig. 3.19   Pressure drop of the bed during fluidization for three-dimensional bed (d_p = 1.0mm, ρ_p = 2650kg/m³)
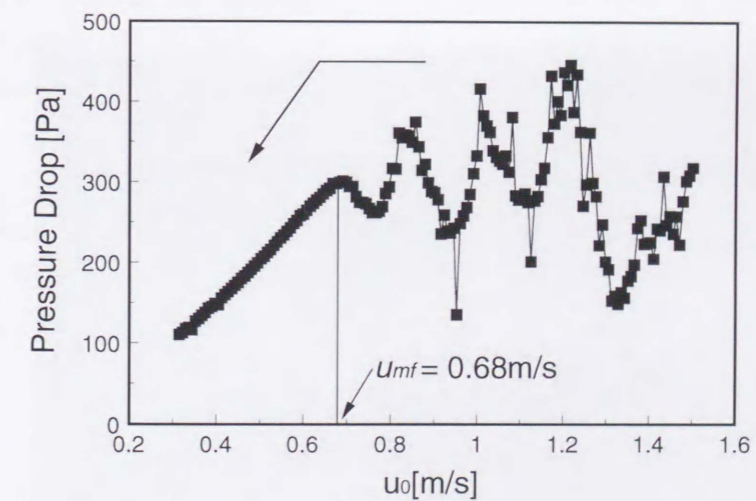
Fig. 3.20   Minimum fluidization measurement of non-cohesive particles for three-dimensional bed (d_p = 1.0mm, ρ_p = 2650kg/m³)
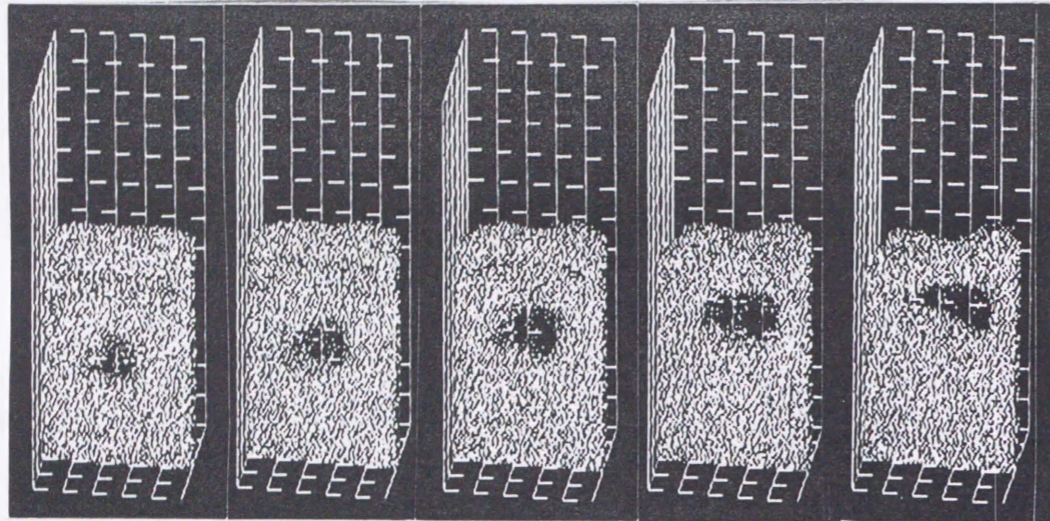
Fig. 3.21   Vertical center cross section of a three dimensional bed showing voidage, granular temperature and gas vector for the bed fluidized at $u_0 = 1.2$m/s at ambient condition
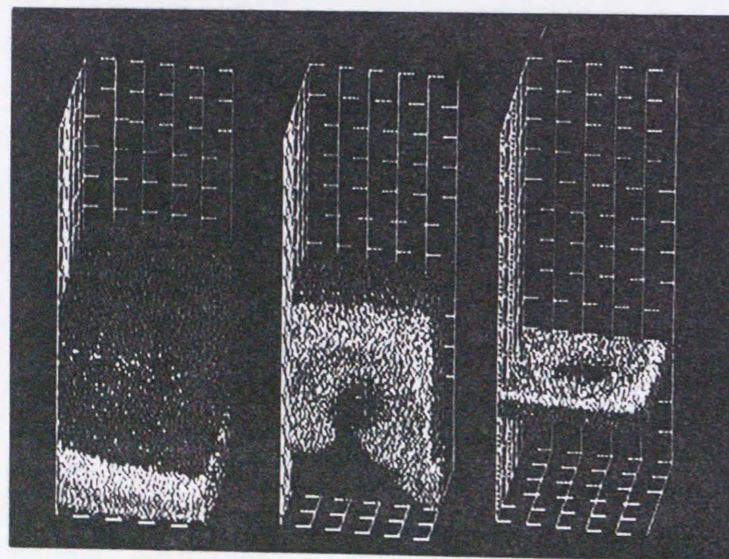
Fig. 3.22   Particle mixing behavior of non-cohesive particles for three dimensional bed (condition is same as Fig. 3.18)

3.4   NUMERICAL SIMULATION OF LIQUID BRIDGING PARTICLES

3.4.1   Model for Liquid Bridging Particles

The following assumptions are made for the simulation of liquid bridging particles:

1. Each particle is supposed to have a liquid film of a volume equivalent to six half bridges (one bridge volume is $\hat{V}$) for SAFIRE and twelve half bridges for 3D SAFIRE. Each particle can have as many liquid bridges as the coordination number n_k, which is six in a single-layer 2D fluidized bed at maximum as shown in Fig. 3.23 and twelve in a three-dimensional geometry. The liquid volume that bridges neither evaporate nor grow by condensation and coalescense.

2. The dynamic force due to viscosity is negligible compared with the static liquid bridge force due to surface tension. Accordingly, the drops can move tangentially without viscous resistance.

3. When a particle comes into contact with other, a steady pendular liquid bridge of a given volume is instantly formed at the contact point.

4. While one particle stays in contact with the other, the forces due to the Hooke repulsive interaction and the cohesive or attractive interaction act between the particles.

5. When particles are bonded by a liquid bridge without direct contact, only the cohesive force due to the liquid bridge acts on the particles, in question.

6. If the separation distance h between particle surfaces exceeds the critical rupture distance h_c (defined in Section 2.2) for a given liquid bridge volume, the liquid bridge ruptures and the liquid returns back to the parent particle surfaces.

7. The interaction between a particle and a wall can be treated in the same manner as above.

3.4.2   Fluidization Behavior of Wet Particles

Fig. 3.24 shows the snapshots of bubbling behavior when the powder ($d_p = 1$mm, $\rho_p = 2650$kg/m^3) was wet by with 0.27 wt% water. The relation between water content, $w[wt\%(\text{dry-base})]$ volume of unit liquid bridge (twice of unit liquid drop) can be calculated from the following equation:

$$w = \frac{\frac{1}{2}\hat{V}(6+6)r_p^3 \rho_{liquid} n \;\; (liquid\; weight)}{\frac{3}{4}\pi r_p^3 \rho_p n \;\; (dry\; particle\; weight)} = \frac{9\rho_{liqudi}}{2\pi\rho_p}\hat{V} \tag{3.23}$$

The corresponding dimensionless liquid drop volume normalized by r_p^3 is 10^{-2}. Although the agglomerate formation and breakage are treated as reversible process in the present model, the calculated fluidization behavior of a wet powder seems
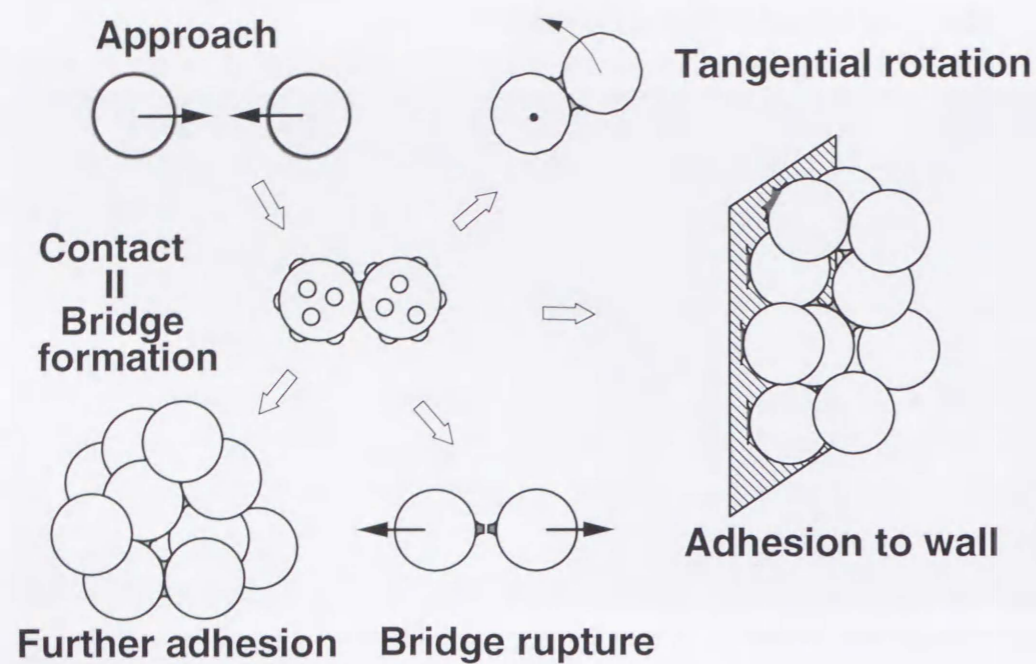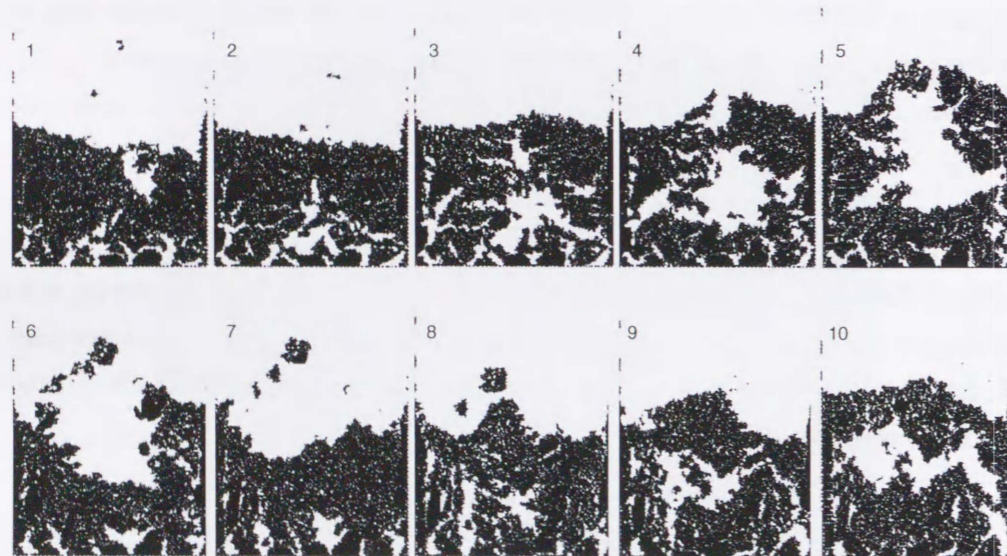
sufficiently realistic including formation, movement and splashing of agglomerates. It can be observed that in the region right above a bubble the liquid bridged dense phase was broken into fragments of agglomerated mass. The defluidized zones were formed between jets, near the walls and at the corner of the bed. In the region right above the gas orifices, a channel like structure exists. The computed pressure drops of the dry bed during bubbling are shown in Fig. 3.25 for both non-cohesive and cohesive powders (shallow bed condition, L = 100mm). The pressure fluctuation of the wet powder bed was larger than that of non-cohesive bed presumably due to the accumulation of energy by liquid bridges.

A single bubble rising behavior of liquid bridging particles ($\hat{V} = 1.0 \times 10^{-2}$) is shown in Fig. 3.26. In this case it was difficult to make a single bubble but a large bubble-like void was formed. With regard to the granular temperature higher granular temperature areas above the forming bubble and below the rising bubble were found and those tendency was similar to the non-cohesive powder bed. The granular temperature seems to be lower than that of dry particles presumably due to the cohesion force that suppresses the particle motion.

The CPU time required for computation of real time of 1 second is shown in Table 3.4 for both non-cohesive and liquid bridging particles. The computation of cohesive interactions increased the computation time slightly.

3.4.3 Effect of Model Parameters on Simulation Results

The effects of liquid bridge volume and the contact angle on the cohesive powder fluidization and the sensitivity of the computed results with the various model parameters, such as the spring constant, the restitution coefficient and the friction coefficient were examined for 2 dimensional cases.

Analysis have been carried out on the following:

1. Computations were performed for the three liquid bridges i.e. $\hat{V} = 1.0 \times 10^{-2}$, 10^{-3} and 10^{-4} (weight % 0.5%, 0.05% and 0.005%, respectively) for the case water and the root mean square (RMS) of pressure fluctuation was calculated for each to investigate the effect of liquid content. The minimum fluidizing velocity was also obtained by numerical simulation for all these cases.

2. In order to examine if the particle stiffness and the restitution coefficient, which have been often treated arbitrarily and modified from the view point of computation economy, affect the computed fluidization characteristics, the computation was performed for spring constant, k of 80, 800 and 80000N/m and for restitution coefficient, e of 0.8, 0.9 and 0.99.
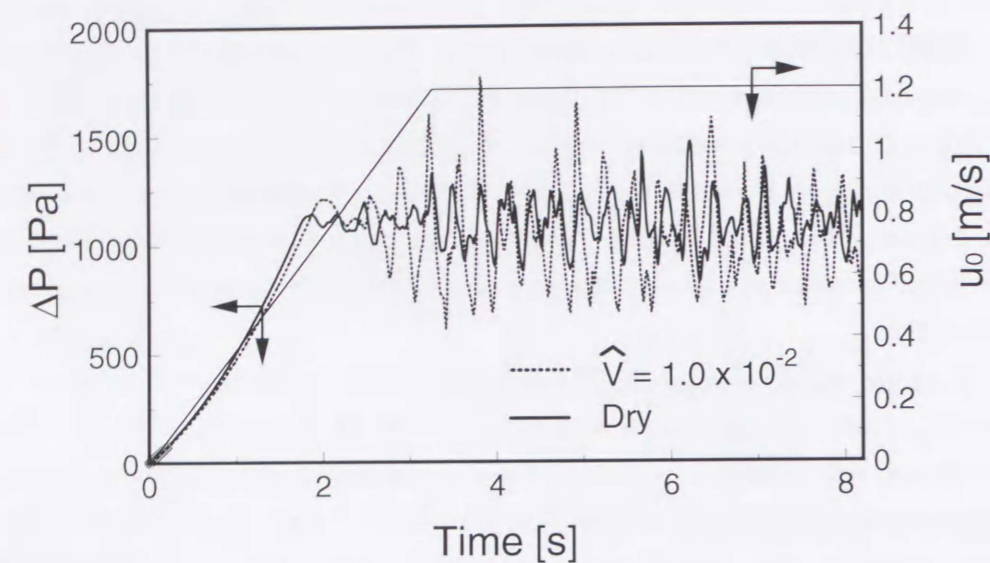

Fig. 3.23   Mode of particle adhesion, rotation and rupture

Fig. 3.24   Snapshots of the behavior of two dimensional (2D) fluidized bed of wet particles (u_0=1.2m/s, d_p=1.0mm, $\hat{V}$ = 1.0x10^{-2}, time interval = 0.0516s)

Fig. 3.25   Bed pressure drop in a 2D fluidized bed

Dimensionless liquid bridge volume V=1.0 x 10^{-2}
Time interval 0.05s   Friction coefficient: 0.3
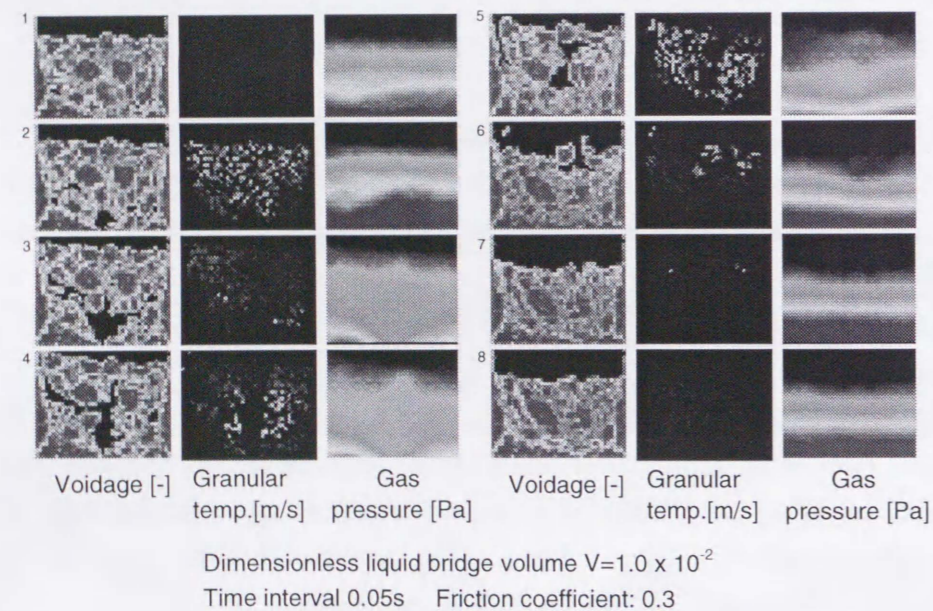
Fig. 3.26   Single bubble rising in a 2D fluidized bed of liquid bridging particles
(d_p=1.0mm, $\hat{V}$ = 1.0x10^{-2}, single orifice)

3. The effect of contact angle θ was investigated for $\theta = 40°$ with respect to $\theta = 0°$ where the dimensionless liquid volume $\hat{V}$ was kept at 0.01. The restitution coefficient and sprig constant used for this analysis were 0.9 are 800N/m respectively.

Fig. 3.27 shows the behavior of the bed when the dimensionless liquid bridge volume was chosen at 1.0 x 10^{-4}. It appears that the bed is fluidized more smoothly than the previous case ($\hat{V}$ = 1.0 x 10^{-2}, Fig. 3.24). The bed pressure fluctuations for the conditions of liquid content ($\hat{V}$ = 1.0 x 10^{-2}, 1.0 x 10^{-3}, 1.0 x 10^{-4} and 1.0 x 10^{-5}) are shown in Fig. 3.28. The pressure fluctuation (RMS) vs. the liquid bridge volume is compared with the RMS for the same powder under the dry non-cohesive condition as shown in Fig 3.29. The pressure fluctuation increased almost linearly with the liquid bridge volume.

In order to characterize the agglomeration of wet particles the minimum fluidization velocity u_{mf} can be used as an index for the test's. Computer experiments were performed to determine u_{mf} by decreasing the superficial gas velocity gradually from 1.2m/s to zero in about 13s. The computed bed pressure drop was plotted against the superficial gas velocity as delineated in Fig. 3.30 both for dry and wet particles. The minimum fluidization velocity obtained for the wet particles was 0.8m/s, which is higher than that of dry particles (0.68m/s) obviously due to agglomeration. In the case of the wet particles, the bed voidage was always higher than that of dry particles when the gas velocity was decreased below the minimum fluidizing velocity. This may be attributed to the wet particles are supported on the wall by liquid bridges, and, accordingly, the bed is suspended even under minimum fluidizing velocity having channels between agglomerates as shown in Fig. 3.31. Sudden stops of the decreasing pressure drop can be observed for the wet particles in Fig. 3.30 below the minimum fluidization velocity and their indicates the collapse of channels resulting in slight increase of pressure drop across the bed.

Fig. 3.32 depicts fluidization behavior of cohesive powder for $\hat{V}$ = 1.0 x 10^{-2} and $\theta = 40°$. The bed behavior was different from that for the contact angle 0° (Fig. 3.24). When contact angles were high, bubbles and pressure fluctuation became smaller and stable jets were formed in the grid zone.

In the preceding section, it has been confirmed that the behavior of non-cohesive powders was not much affected by the model parameters. However, since rupture condition may be affected by the history of a collision event, it is worthy examining the effect of these parameters carefully for the powders that formed liquid bridges. The equilibrium overlap distances Δx, was calculated by balancing the cohesion force and elastic force. The relevant equation is:

Table 3.4   CPU time on HP 9000 C110 for computation

	CPU time	real time
DRY	2.7 hour	1s
WET	3.6 hour	1s

Conditions: Number of particles: 14000

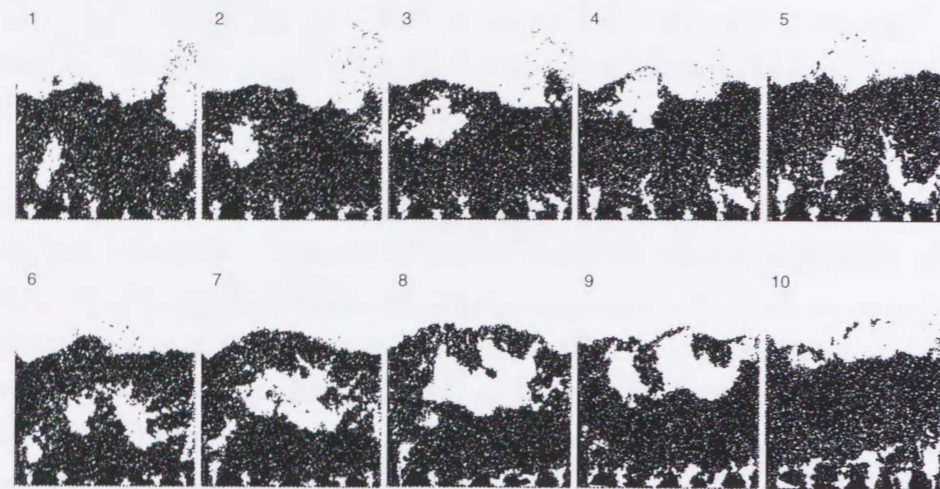Number of fluid cells: 41 x 105 = 4305

Computation time step: 25.9μs

Fig. 3.27   Fluidization behavior of wet particles in snapshots (u_0=1.2m/s, d_p=1.0mm, $\hat{V}$ = 1.0x10^{-4}, time interval = 0.0516s)
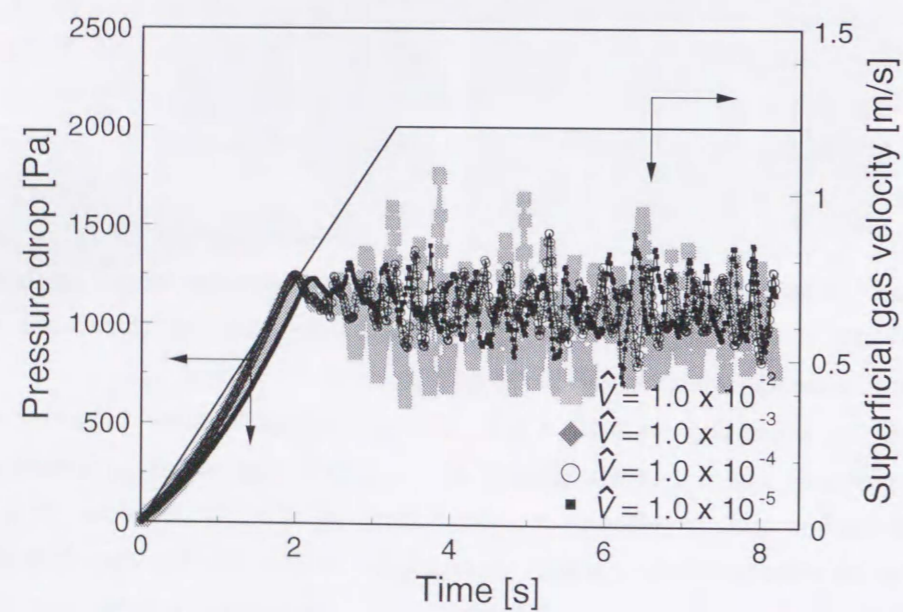

Fig. 3.28   Bed pressure drop of liquid bridging particles for $\hat{V}$ = 1.0x10^{-2}, 1.0x10^{-3}, 1.0x10^{-4} and 1.0x10^{-5}
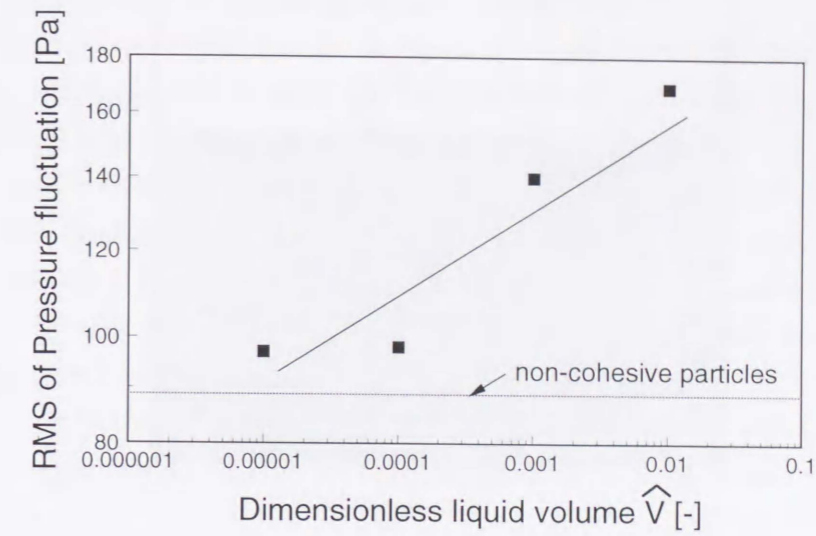
Fig. 3.29   Root mean square of the fluctuations in bed pressure drop for cohesive particles (u_0 = 1.2m/s, d_p = 1mm)
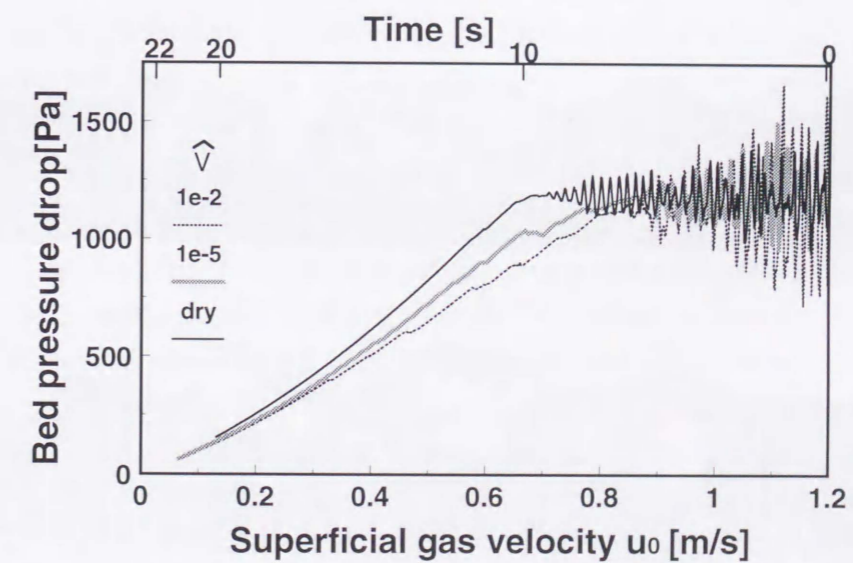
Fig. 3.30 u_0-Δp plot of the bed during decreasing gas velocity
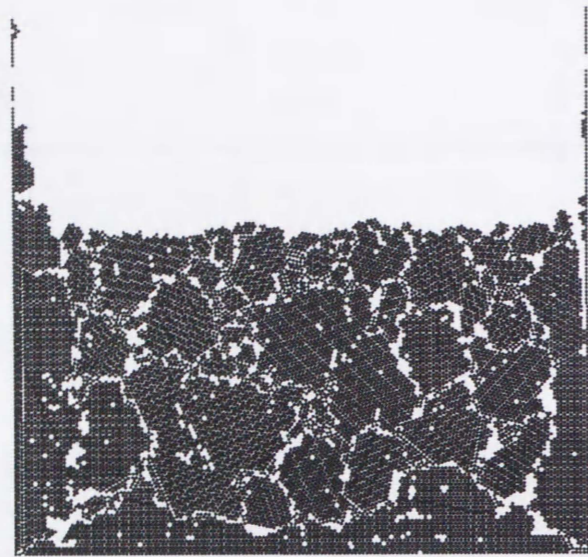
Fig. 3.31   A snapshot of wet particle fixed bed after fluidization in a 2D bed

($u_o = 1.2 \rightarrow 0.5$m/s, d_p=1.0mm, $\hat{V}$ =1.0x10^{-2})
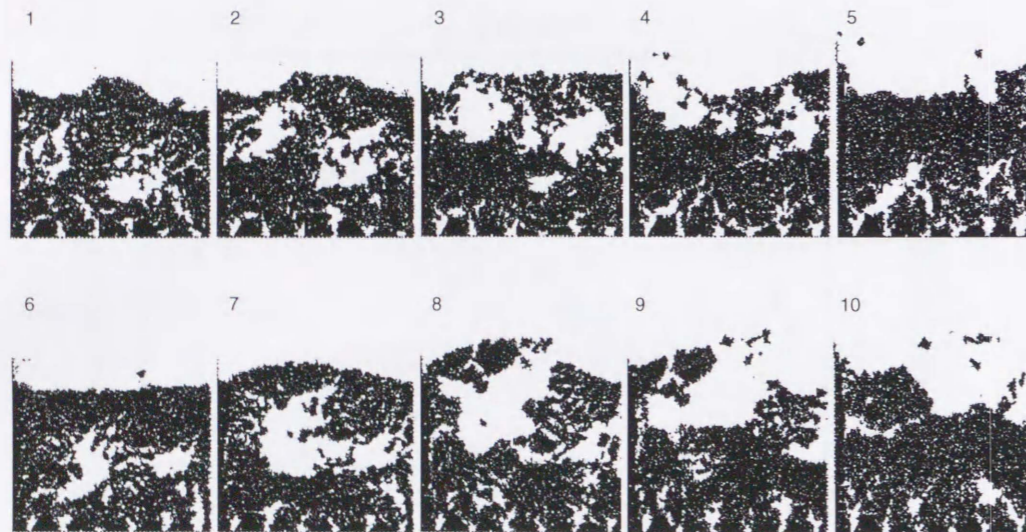
Fig. 3.32   Snapshots showing fluidization behavior of wet particles at u_o=1.2m/s,

d_p=1.0mm, $\hat{V}$ = 1.0x10^{-2}, contact angle = 40° in a 2D bed (time interval

= 0.0516s)

$$\Delta x = 3.5k / \pi d_p \gamma \qquad\qquad (3.24)$$

Comparing them with the maximum overlap distance in Table 3.2, we can see that the former is still one order of magnitude smaller than the latter.

Fig. 3.33 shows the calculated pressure drop of the bed for spring constant $k = 80000$N/m, which required 10 times CPU time of that obtained when using $k = 800$N/m. The calculated pressure fluctuations were not much different even if k was increased from 800 to 80000N/m. Thus the spring constant of the particles was found not affecting the fluidization behavior significantly even for the cohesive fluidization. However, when $k = 80$N/m was used, the computation was found unable because of the numerical difficulty (unreasonable particle motion). This tendency is similar to dry particle fluidization as discussed in the earlier section.

Fig. 3.34 shows the result when the restitution coefficient was varied from 0.8 to 0.95.   The simulation result is not much different for all these value.

3.4.4   Model validation by experiment

Computed result was validated by experiment using a 200mm diameter three-dimensional bed of grass beads (Particle diameter: 1.04mm, particle density: 2500kg/m^3 liquid: water, gas: air).   Measured minimum fluidization velocity, u_{mf}, of dry powder by experiment was 0.54m/s (Fig. 3.7).   Although the minimum fluidization velocity at dry condition obtained by experiment was less than numerically obtained one, the deviation was within 30% error.   This over-estimation of minimum fluidizing velocity of dry particles can be attributed to the difference in packing behavior between real 3D bed and one-layer bed of spheres.

The pressure fluctuation of dry powder by experiment (Fig. 3.35) was quite similar to the result obtained by the numerical experiment (Fig. 3.6).   The pressure fluctuation of shallow bed (L = 100mm) increased with the liquid content of powder beds (Fig. 3.35) and this tendency of liquid bridging powder was also well agreed with the numerical results using SAFIRE model.   However, experimentally obtained pressure fluctuation of a deep (L = 200mm) of wet powder bed were decreased with liquid content of the beds (Fig. 3.36).   The numerically obtained pressure fluctuation of deep bed for both dry and wet particles were delineated in Fig. 3.37.   SAFIRE model predicted almost similar tendency that the difference in pressure fluctuation between dry and wet particles was decreased with increasing bed height.   It was confirmed that the SAFIRE model can predict the fluidization behavior of dry and wet particles accurately.
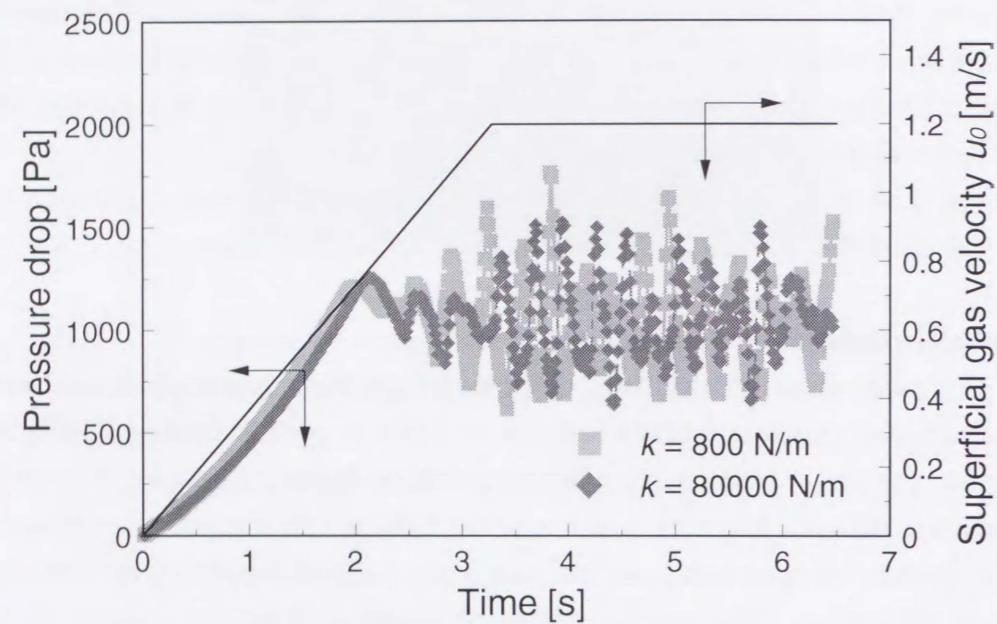
Fig. 3.33   Effect of spring constant on pressure drop of liquid bridging particles
($\hat{V} = 1.0 \times 10^{-2}$, $k = 800$, 80000N/m) in a 2D bed

Table 3.5 Effect of the spring constant on equilibrium overlap distance

spring const. k [N/m]	Equilibrium overlap distance $\Delta x/d_p$ [-]
8	9.90×10^{-2}
80	9.90×10^{-3}
800	9.90×10^{-4}
80000	9.90×10^{-6}
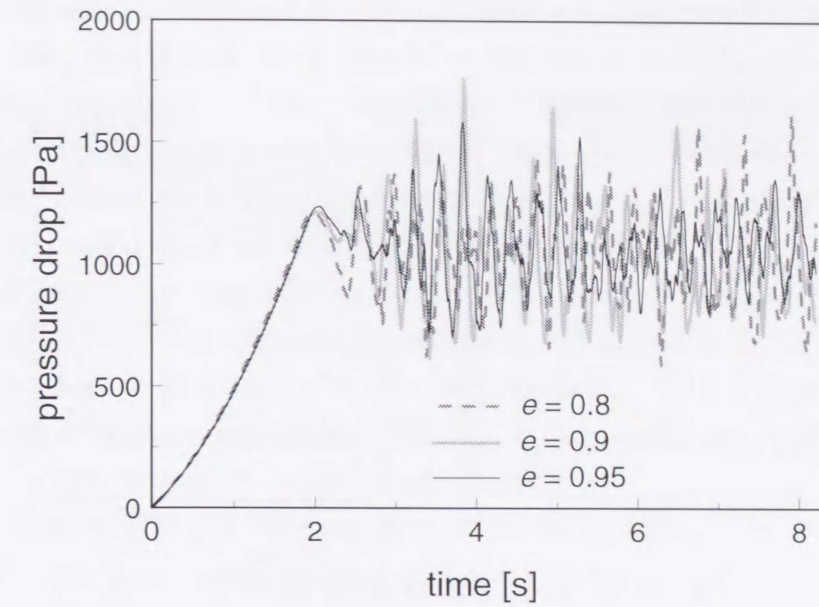
Fig. 3.34   Effect of restitution coefficient on pressure drop of liquid bridging
particles in a 2D fluidized bed ($\hat{V} = 1.0 \times 10^{-2}$, $e = 0.8$, 0.90 and 0.95, u_0
$= 1.2$m/s)
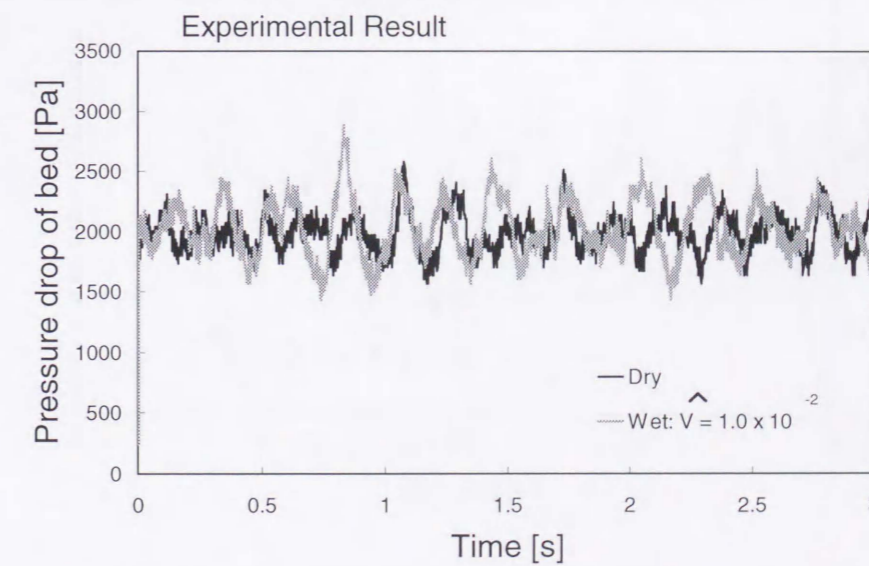
Fig. 3.35   Experimentally obtained pressure drop of grass bead beds at dry and
wet ($\hat{V} = 1.0 \times 10^{-2}$) conditions (particle diameter: 1040μm, particle
density: 2650kg/m³, bed height: 200mm, superficial gas velocity:
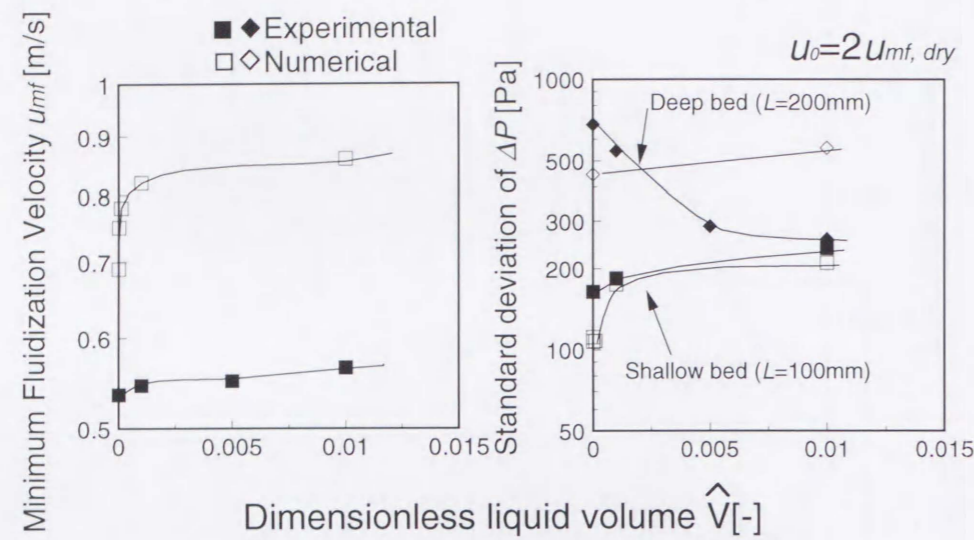$2.0u_{mf, dry}(= 1.08$m/s))

Fig. 3.36   Difference in the minimum fluidization velocity and standard deviation of pressure fluctuations between experimental and numerical obtained results
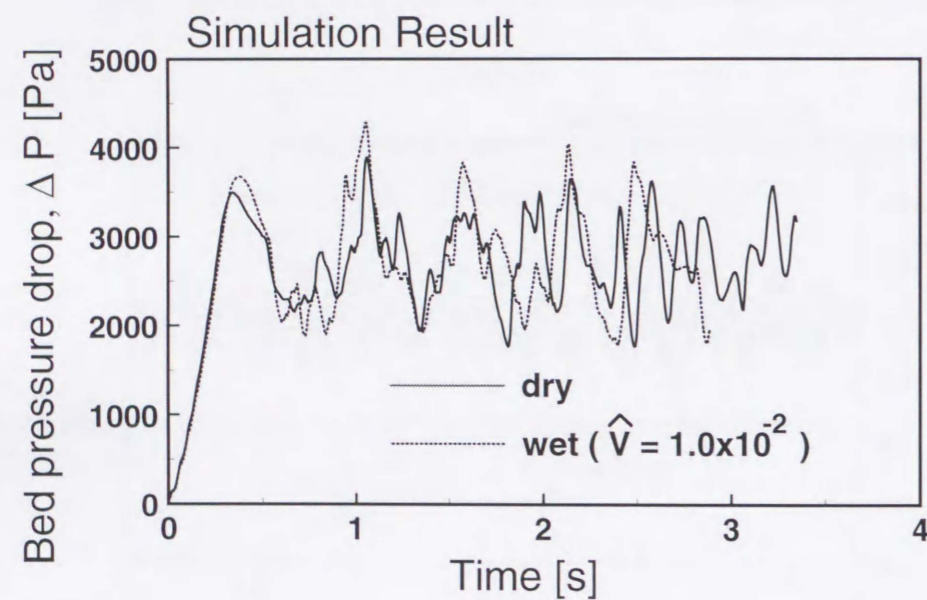

Fig. 3.37   Computed pressure drop of deep grass bead beds at dry and wet ($\hat{V}$ =1.0 x 10^{-2}) conditions (particle diameter: 1040µm, particle density: 2650kg/m³, bed height: 200mm, superficial gas velocity: $2.0u_{mf.\ dry}$(= 1.08m/s))

3.4.5   Numerical Simulation of Three Dimensional Fluidized Bed of Wet Particles

The objective of the section is to simulate a three-dimensional fluidization behavior of wet powders.   The computation condition is depicted in Table 3.6.   Two type of scale bed, A and B, which consist of 150000 and 500000 particles, respectively were simulated ant the bed is a three-dimensional fluidized bed having a square bottom and the side walls, which are assumed to be frictional.

Computation was performed with a workstation (Hewlett Packard HP9000 C180).   The CPU time required for computation of real 1s is shown in Table 3.7 for both non-cohesive (dry) and cohesive (wet) particles.   The computation of 90mm square bed took huge time for computation.   Only preliminary calculation can be carried out with the present computer technology.

Fig. 3.38 shows the snapshots of bubbling behavior in the fluidized bed "A" when the 1mm grass beads powder was wetted with 1.0×10^{-3} water (moisture content: 0.05wt%-dry base).   The large powder agglomerate rose in the column without major fragmentation or deformation of a plug.   A large bubble whose diameter was same as bed diameter had no capability of breaking the solid slug.   To simulate not slugging but bubbling behavior of wet powder fluidized bed, a simulation for the large cross section (0.09m x 0.09m) bed "B", which had 16 gas nozzles and contained 500000 particles, was carried out.   The snap shots of bed behavior contained the same amount of water as the previous condition are shown in Fig. 3.39.   At the onset of fluidization the channel formation on the nozzles and fracture of a agglomerate was successfully found.

Table 3.6 Computation conditions for 3-D calclulation of wet particles

Particles	A	B
Number of particles	150000,	500000
Particle density	2650kg/m^3	
Particle diameter	1.0mm	
Collision parameters		
Restitution coefficient	0.9	
Friction coefficient	0.3	
Spring constant	800N/m	
Computational grid parameters		
Number of fluid cells	12x12x30,	21x21x63
Time step	2.58 x 10^{-5}s	
Fluidized bed parameters		
Number of nozzles	Porous plate and 9,	16
Opening diameter	3.7mm	
Gas : Air		
Viscosity	1.75✕10^{-5}Pa s	
Liquid : water		
Surface tension	0.073N/m	

A 0.12m 0.05m 0.05m

0.27m 0.09m 0.09m B
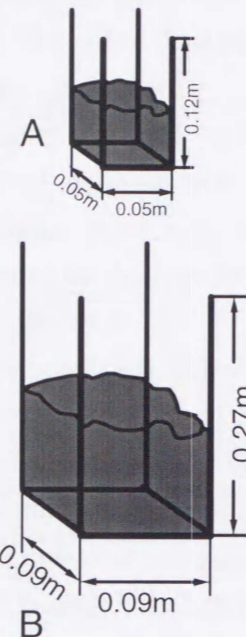
Table 3.7 CPU time on HP9000 C180 for computation of wet partiles

		CPU time	Real time
Dry	particle 150000 cell 0.5 x 0.5 x 0.12	**5 days**	**1 sec**
Wet	particle 150000 cell 0.5 x 0.5 x 0.12	**6 days**	**1 sec**
Wet	particle 500000 cell 0.9 x 0.9 x 0.27	**3 weeks**	**1 sec**

Time step : 25.8 μs
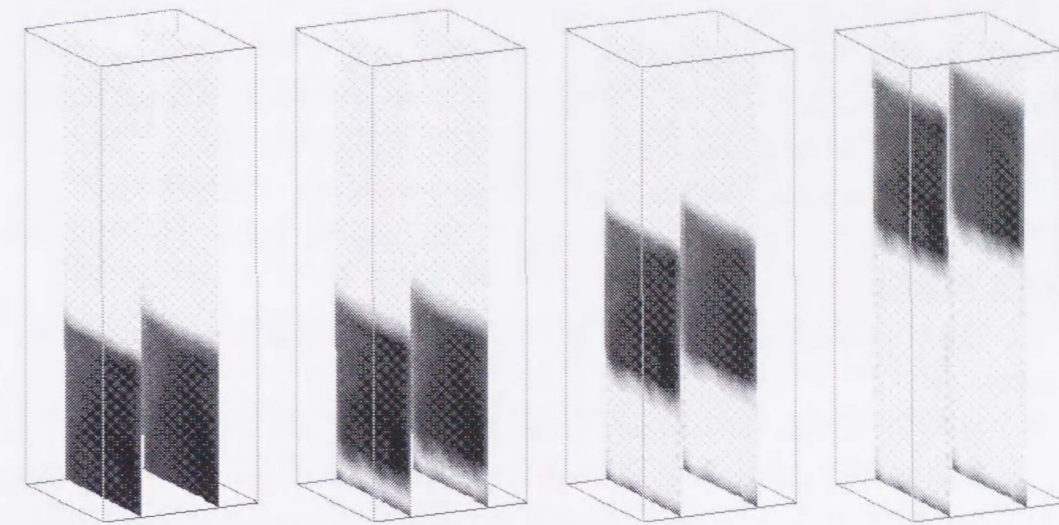

Fig. 3.38   Snapshot of fluidization behavior of the small bed "A" (Bed size: 0.05x0.05x0.12m, $\hat{V}$ =1.0x10^{-3})
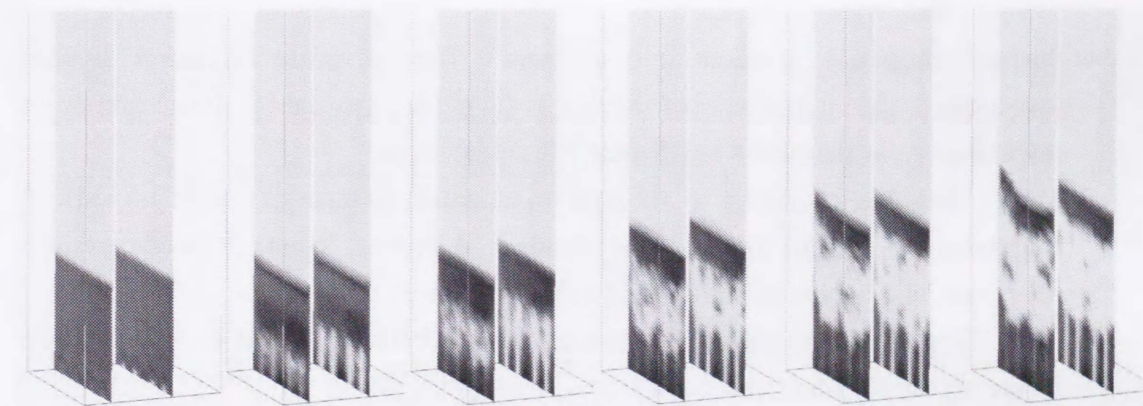

Fig. 3.39   Snapshots of fluidization behavior of large bed "B" (Bed size: 0.9x0.9x0.27m, $\hat{V}$ =1.0x10^{-3})

3.5   NUMERICAL SIMULATION OF SOLID BRIDGING PARTICLES

3.5.1   Model for Solid Bridging Particles

As has been discussed in Chapter 1, solid bridging force is also quite important factor in iron reduction process, ash agglomeration in pressurized fluidized bed combustion, poly-olefin gas phase polymerization and silicon chemical vapor deposition process.   The sintering phenomena is time dependent process so that fluidization behavior of solid bridging particles must be completely different form that of liquid bridging particles.   In this section high temperature fluidization of iron partices was modeled as case study.   In order to develop the model the following assumptions were made:

1. The spring constant of solid bridge for repulsion and ataction is the same as bulk materials.
2. A neck was formed between any contacting particles and neck diameter was estimated by Kuzynski's surface diffusion model (Eq. (2.15)) using contact time.
3. Duration of collision is overestimated because of adopting softened spring constant from the viewpoint of computation efficiency.   The duration of contact used for estimation of neck growth is calculated using practical value of Young modulus.

$$T_{d.Hertz} = 1.15\left(\frac{m^2}{\alpha^2 v}\right)^{1/5}$$ (3.25)

$$\alpha = \frac{E\sqrt{d_p}}{3(1-v)}$$ (3.26)

4. Surface roughness is taken into account.   The curvature radius of surface roughness apparent diameter of roughness (Fig.) are assumed to 10µm and 6µm, respectively , as measured in Chapter 2 for steel shots.
5. In the SAFIRE model it is difficult to calculate exact geometry of surface roughness on contact point.   The number of contact points between surface roughness at one contact is assumed to 9 as indicated Fig.
6. Neck breakage take place if interaction force between particles satisfies the following conditions:

$$F_n = \sigma_{neck,n} \sum A_{neck}$$ (3.27)

$$F_n = \sigma_{neck,n} \sum A_{neck} .$$ (3.28)

7. If neck breakage take place all necks at one contact point were broken.
8. Friction coefficient was assumed to be infinity to fix contact points.

3.5.2   Fluidization Behavior of Solid Bridging Particles

Computation condition is depicted in Table 3.8.   Long time computation for an hour in real time can not complete due to the pro   blem of computation time, temperature for computation condition was set to very high temperature to make the effect of cohesive force significant and to obtain sintering effect earlier.   The bed was fluidized at superficial gas velocity $u_0 = 0.26$m/s and bed aspect ration, L/D was 1.2. The cohesive force and sintering were not taken into account during first 0.5s, and then sintering phenomena was taken.   The fluidization behavior (Fig. 3.41) was completely different from that of liquid bridging particles.   In snapshots No. 2-8 agglomerating fluidization was found in upper region of the bed.   At the bottom region between nozzles where particle movement is not so strong, particles made agglomerates and channels formed on nozzles grown upward.   At the snapshot No. 10 the half particles below vertical center did not move and sintered.   The bed pressure drop was indicated in Fig. 3.42.   Both amplitude of pressure fluctuation and absolute value of pressure decreased with time.   The former decreasing correspond to decreasing of effective bed height to bubbling due to sintering of the bed bottom and the latter decreasing means gas flow through channels makes less pressure drop than through a powder bed.   The calculation result without surface roughness shows the same tendency to that with surface roughness and defluidization took place earlier for that with surface roughness. This kind of pressure drop profile agreed well with the experimental data (Fig. 2.17) obtained for the same condition for computation except temperature and bed size.
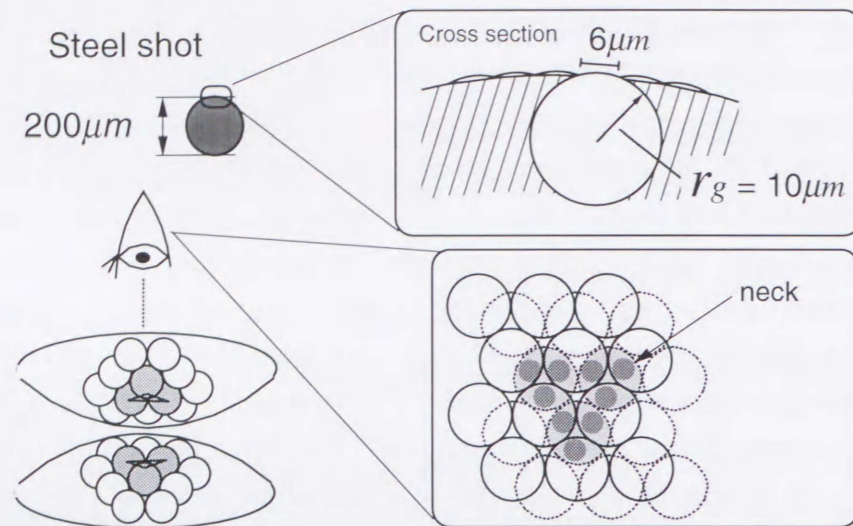
Steel shot

$200\mu m$

Cross section $6\mu m$

$r_g = 10\mu m$

neck

Fig. 3.40   Schematic diagram of surface roughness and magnification of contact point

Table 3.8   Computation conditions for solid bridging particles

Particles : Steel shot		Gas : H_2:N_2 = 3:1	
Number of particles	7000	Temperature	1273K
Particle density	7800kg/m^3	Viscosity	2.29×10^{-5} Pa s
Particle diameter	200μm	Density	9.67×10^{-2} kg/m^3
Young Modulus	8.0×10^{10} N/m^2	**Collision parameters**	
Poison ratio	0.28	Restitution coefficient	0.9
Tensile strength		Friction coefficient	0.3
Normal	4.0×10^6 Pa	Spring constant	800N/m
Tangential	1.6×10^7 Pa	**Computational grid parameters**	
Lattice constant	2.89×10^{-10} m	Number of fluid cells	21 x 82
Boltzman const.	1.38×10^{-23} J/K	Time step	1.00×10^{-6} s
Surface energy	1.72 N/m	**Fluidized bed parameters**	
		Bed size	0.0153 x 0.06m
		Number of nozzles	6
		Opening diameter	0.73mm

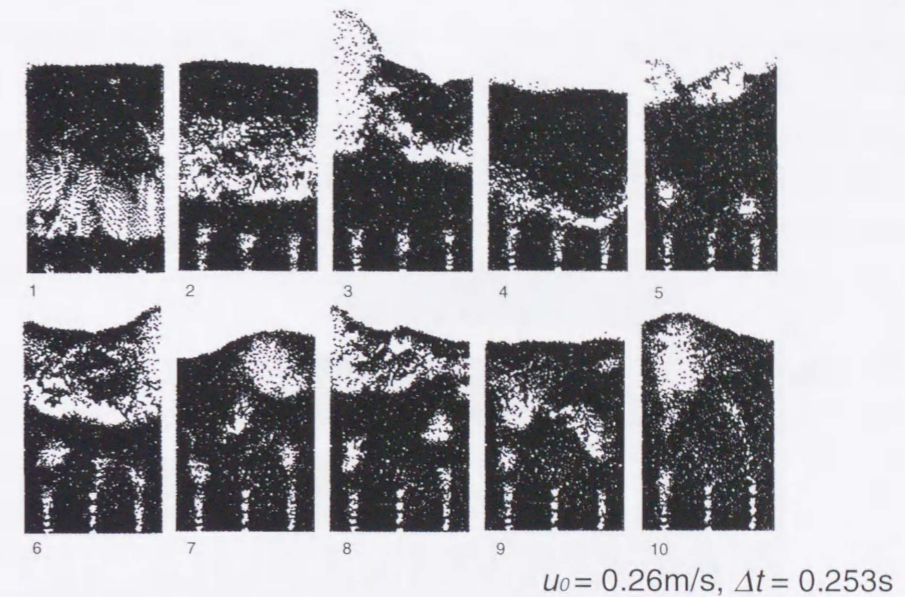
u_0 = 0.26m/s, Δt = 0.253s

Fig. 3.41   Snapshots showing fluidization behavior of solid bridging particles (1273K, u_0 = 0.26m/s, without surface roughness (curvature radius = 100μm)

With surface roughness
$a = 10\mu m$

Without surface roughness
$a = 100\mu m$

Pressure drop [Pa]
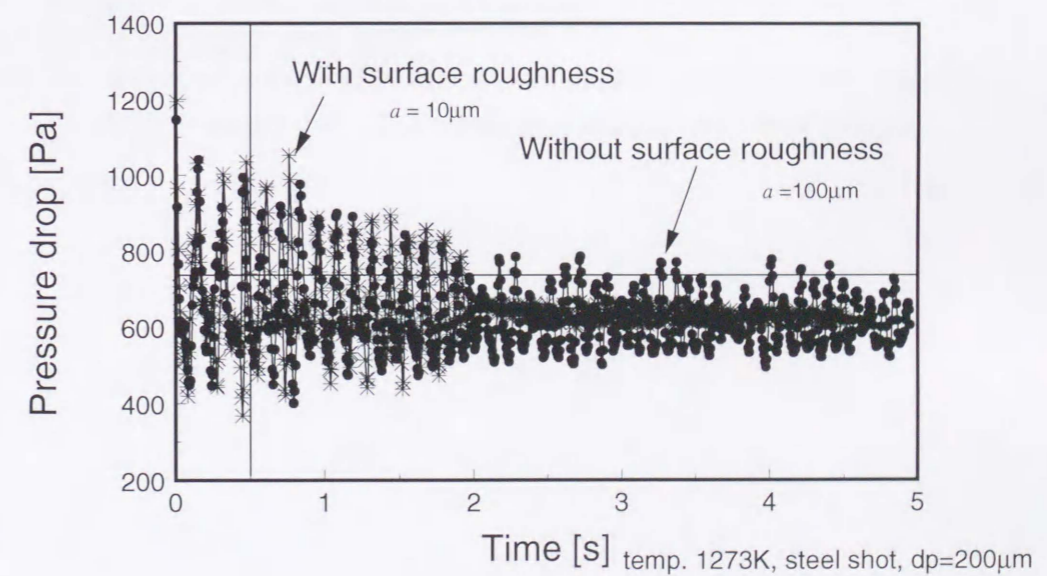
Time [s]   temp. 1273K, steel shot, dp=200μm

Fig. 3.42   Bed pressure drop of solid bridging particles (1273K, u_0 = 0.26m/s, with (curvature radius is 10μm) and without surface roughness (curvature radius = 100μm)
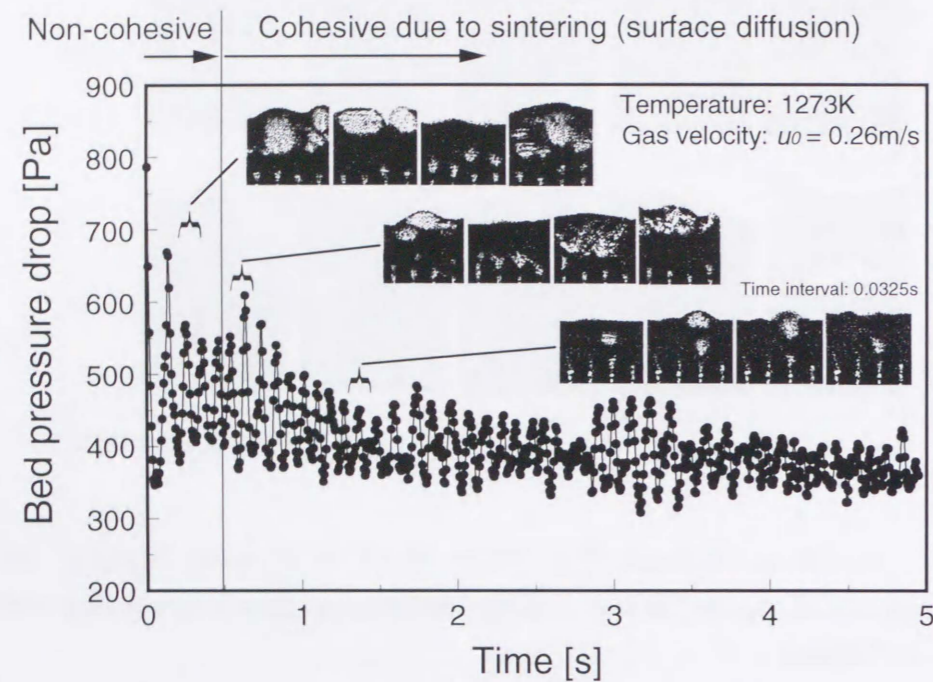
Fig. 3.43   Bed pressure drop of solid bridging particles at shallow bed condition and corresponding snapshots showing fluidization behavior (1273K, without surface roughness (curvature radius = 100μm)

3.6   CONCLUSIONS OF CHAPTER 3

A DEM simulation code (SAFIRE) based on the soft sphere interaction at particle collision was developed for the simulation of fluidization behavior of non-cohesive, liquid bridging and solid bridging powders.

The bubble formation, coalescence, eruption and particle circulation for non-cohesive powders obtained by the simulation were all found to be sufficiently realistic. The bed behavior predicted was not much affected by the change of spring constant and restitution coefficient as far as the maximum overlap distance is less than 10% of particle diameter.

Regression equations concerning the liquid bridge force and the critical rupture distance have been already developed for the liquid bridging particles in Chapter 2 and they were introduced into SAFIRE model. Fluidization behavior of liquid bridging particles was successfully reproduced. An increase in the volume of liquid that forms bridge between particle increased the pressure fluctuation in the bed, produced larger bubbles with more irregular shape. Jets on the distributor were unstable. The minimum fluidizing velocity for wet particles was higher than that for dry particles under identical condition. It was confirmed that the SAFIRE model can predict the fluidization behavior of dry and wet particles accurately from experimental validation.

The behavior of solid bridging particles in a fluidized bed was successfully demonstrated by SAFIRE model taking into account the cohesiveness of particles at high temperature and mechanism of solid bridging as per surface diffusion theory which has already discussed in Chapter 2.

REFERENCES

1) Tsuji, Y., T. Kawaguchi and T. Tanaka, 'Discrete Particle simulation of two – dimensional fluidized bed', *Powder Techonol.* **77** (1993) 79
2) Ergun, S., 'Fluid flow through packed columns', Chem. Eng. Progr. 48 (1952) 89
3) Wen, C. Y. and Y. H. Yu, 'Mechanics of fluidization', *Chem. Eng. Prog. Symp. Ser.* **62** (1966) 100
4) Anderson, T. B. and R. Jackson, "A Fluid Mechanical Description of Fluidized Bed," *Ind. Eng. Chem. Fundamentals*, **6** (1967) 527
5) Patanker, S. V., Numerical heat transfer and fluid flow, Hemisphere, New York (1980)
6) Chapman, A. and T. G. Cowling, "The Mathematical Theory of Non-Uniform Gases," 3rd ed., Cambridge Univ. Press, Cambridge (1970)
7) Rowe, P. N. and B. A. Partridge, "An X-Ray Study of Bubbles in Fluidised Beds," Trans. Inst. Chem. *Eng.* **43**, (1965) T157

CHAPTER 4

CONTROL OF AGGLOMERATION BEHAVIOR IN A FLUIDIZED PROCESS

—— A CASE STUDY: PRODUCTION OF IRON POWDER THROUGH SPONTANEOUS AGGLOMERATION AND SEDIMENTATION

——

CHAPTER 4
CONTROL OF AGGLOMERATION BEHAVIOR IN A FLUIDIZED PROCESS
—— A CASE STUDY: PRODUCTION OF IRON POWDER THROUGH SPONTANEOUS AGGLOMERATION AND SEDIMENTATION ——

4.1 INTRODUCTION

Powder metallurgy has been well known cost-effective and energy-saving manufacturing process for machine tool production more particularly in the automobile industries. Powder metallurgy processes require no melting and no machining to produce mechanical parts. The process can be used to produce porous materials shape that can be adopted for producing oil immersed axles. One highest cost of manufacturing powder metallurgy products is the price of raw iron powders [1]. Iron powder is conventionally produced using belt furnaces for reducing of iron oxide particles and their annealing. This process requires a large high-temperature zone even for reducing the very thin oxide layer. The reason for adopting such an energy-intensive and space-inefficient process is the high temperature cohesiveness of iron particles. The application of ordinary gas distributors or grates adds to the problem due to sintering of iron powder onto the distributor and also plugging of gas orifices by the cohesive iron powders. Hence, the reducing gas is supplied from the bed top. In such a case, the bed height must be shallow from the viewpoints of achieving rapid gas distribution and reducing the diffusion time. The development of an improved iron powder production process, using "fluidization" technique, is to taken up on a continuous scale and the gas-solid contacting efficiency is to be increased. Fluidized beds were once tested for direct iron ore reduction processes in many countries but abandoned because of the serious defluidization due to cohesiveness of metallic iron particles. However, it seems worth exploring the fluidized bed processes again, because the effects of cohesion forces in fluidization has been sufficiently understood now, and a variety of fluidization methods are now available to arrive at a satisfactory level of conversion. The cost of iron powder production is usually high [1] for the powder metallurgical applications.

As has already been discussed in Chapter 1, there are now several attempts to use fluidized beds to reduce iron ore particles. However, the cohesion force among the fine pure iron powder is very strong. Hence, a process that is more effective and reliable has to be developed for new iron powder production process.

For instance, the sintering due to the cohesion force of metallic iron can be

eliminated if particles were fluidized in a bed of inert material. Still certain agglomeration may take place. The agglomerates can be easily separated by segregation in the fluidized bed. Since there has been no study on such a process, the possibility of producing iron powder by a process that would bring in the spontaneous agglomeration and sedimentation is described in the following. Experimental studies carried out in a fluidized bed on a lab scale both a cold and hot conditions.

NOVEL METHOD

Fig. 4.1 illustrates a novel method of iron powder production through spontaneous agglomeration and sedimentation in a fluidized bed. Iron oxide particles are reduced in a bed of inert materials to prevent the reduced iron powder forming into extremely large agglomerates that can cause serious defluidization. In addition, the fine raw iron oxide particles remain in the upper region of the bed due to segregation and are reduced by the fluidizing gas until they exhibit strong cohesiveness typically of metallic iron phase. The reduced iron oxide particles tend to agglomerate and settle down to the bed bottom. Thus, a continuous reduction and separation became possible achieving a high gas conversion. The fluidized bed should have a bed height (aspect ratio) sufficient for finishing the reduction within the residence time of iron/iron oxide particles. In the bottom region agglomerates are discharged, cooled down, and deagglomerated, and then impurities are removed by a magnetic separator.

In order to evaluate the above process, it is necessary to confirm the following: 1) The possibility of segregating iron oxides particles of 120μm in the upper region of the inert bed itself, 2) The formation of agglomerates of reduced iron in the inert bed material, 3) The right choice of inert bed material that would create a conducive environment for agglomerate formation and 4) The sedimentation of agglomerated iron powders at the bottom without defluidization. In this work 1) and 4) have been examined by the cold model experiments and 1) ~ 4) by experiments in hot rigs.

4.2 COLD EXPERIMENT FOR SEGREGATION BEHAVIOR

4.2.1 Apparatus and Experimental Procedures

The fluidized bed cold model was made of a acrylate resin tube having an inner diameter of 49mm and a height of 462mm (Fig. 4.2). The water atomized raw iron particles (AT79), iron ore (OR79) or iron agglomerates (IA) of 5g were charged on the surface of the fluidizing bed instantly. After fluidizing the bed for some period, the gas flow was suddenly stopped by solenoid valve. Particles from the settled bed were collected at various sections of the bed by a vacuum cleaner. The weight fraction of
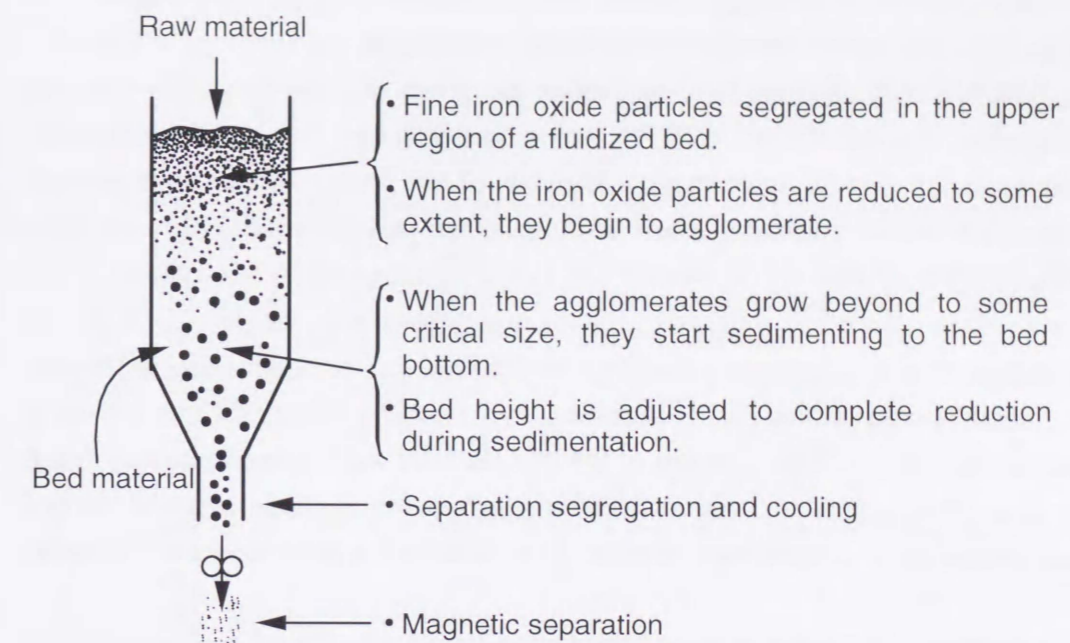
Fig. 4.1   A novel concept for continuous reduction of fine iron oxide powder using fluidized bed
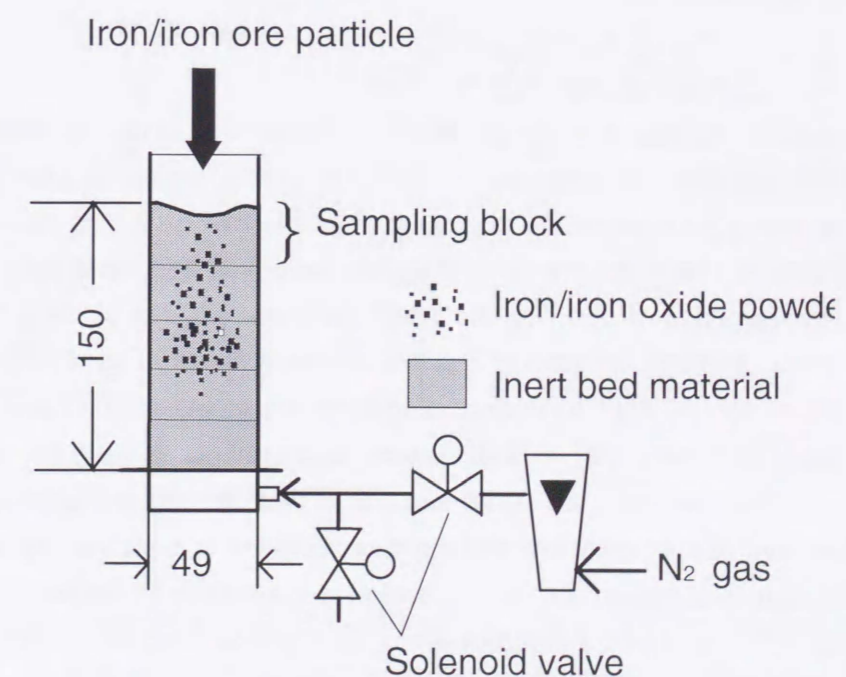

Fig. 4.2   Experimental apparatus for cold test

the iron oxide particles or iron agglomerates in each section of the bed was measured by sieving or magnetic separation depending on their particle size.

The bed materials and their properties are given in Table 4.1. For raw iron oxide particles, iron ore (Brazil) (OR79), water atomized raw iron powder which has oxidized layer of several micrometer) because of the water atomization at high temperature (AT36, 79), reduced water atomized iron particles (AT57R) were used. The reduced water atomized iron powder (AT57R) was subjected to sintering at 1073K for an hour, then cooled and crushed to obtain iron agglomerate samples (IAXX), XX stands for agglomerate diameters in μm unit for the segregation experiments in the cold model. Sand, silicon carbide (SiC), alumina (Al_2O_3) and Zirconia (ZrO_2) were used as the inert bed materials. The diameter of the bed material was chosen to be larger than the raw iron powder size of 100μm in order to avoid the agglomeration of the bed materials themselves. Hence, the diameter of bed materials was fixed at about 500μm.

4.2.2 Segregation Behavior of Raw Iron Oxide Particle and Iron Agglomerates in Various Bed Materials

The axial concentration profiles of the water atomized raw iron particles (AT36)) present in a silica sand bed are shown in Fig. 4.3(a). The ordinate is the bed height and the abscissa is the dimensionless weight fraction $X / \overline{X}$ where X is the weight fraction of iron particles in each section and $\overline{X}$ is the average weight fraction of iron particles in the whole bed.

$$\frac{X}{\overline{X}} = \frac{w_{inert} / (w_{bed} + w_{inert})}{\sum w_{inert} / (\sum w_{bed} + \sum w_{inert})} \tag{4.1}$$

When complete mixing is obtained, $X / \overline{X}$ is equal to 1 over the bed. The AT36 particles have tendency to segregate and move to the top region as exemplified in Fig. 4.3(a). In order to express the segregation quantitatively, let l_{50} denote the height above which half of the iron particles or agglomerates can be found. Fig. 4.3(b) shows the transient response of l_{50}/L for the AT36 particles. It can be seen from the Fig. 4.3(b) that the segregation quickly reached a steady state. Fig. 4.4 shows the axial distribution of the AT79, OR79 or iron agglomerates (IA) in the three kinds of bed material, sand, SiC and Al_2O_3. In all system the excess gas velocity ($u_0 - u_{mf}$) was set to 0.06m/s. In the sand bed, the AT79 and OR79 particles did not segregate sharply to the bed top and almost complete mixing was achieved at high gas velocity. The IA particle of diameters larger than 350μm settled at the bottom of the bed. In the case of SiC bed the AT79 and OR79 particles segregated well and moved to the top and the IA particles larger than 710μm sedimented to the bottom. The bed Al_2O_3 with the AT79 and OR79 particles strongly segregated in top region, and only IA particles of diameters. Fig. 4.5 shows the dimensionless average sedimentation distance l_{50}/L as a larger than

Table 4.1   Physical properties of powder

Iron or iron oxide

Code	d_p[μm]	u_{mf}[m/s]	ρ_p[kg/m³]	Remarks
AT36	36	0.015	6900	Unreduced water atomized raw iron powder
AT79	79	0.015	6900	Unreduced water atomized raw iron powder
AT57R	57	0.015	7800	Water atomized iron (reduced) powder
OR79	79	0.011	4900	Iron ore (Brazil)
IA	210-1410			Sintered agglomerates of AT79 at 1173K

Bed materials

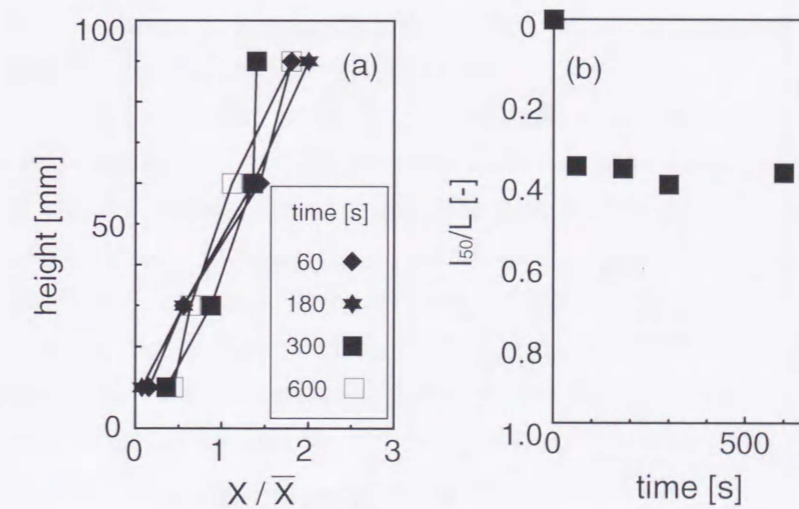| Code	d_p[μm]	u_{mf}[m/s]	ρ_p[kg/m³]
SiO_2	409	0.14	2650
SiC	522	0.42	3170
Al_2O_3	450	0.47	3990
ZrO_2	500		6050

Fig. 4.3 Segregation behavior of silica sand beds (a) Normalized weight fraction $X / \overline{X}$ vs. bed height, (b) Time vs. average sedimentation distance l_{50}/L (In silica sand bed, AT36, at $u_0 = 0.22$m/s)
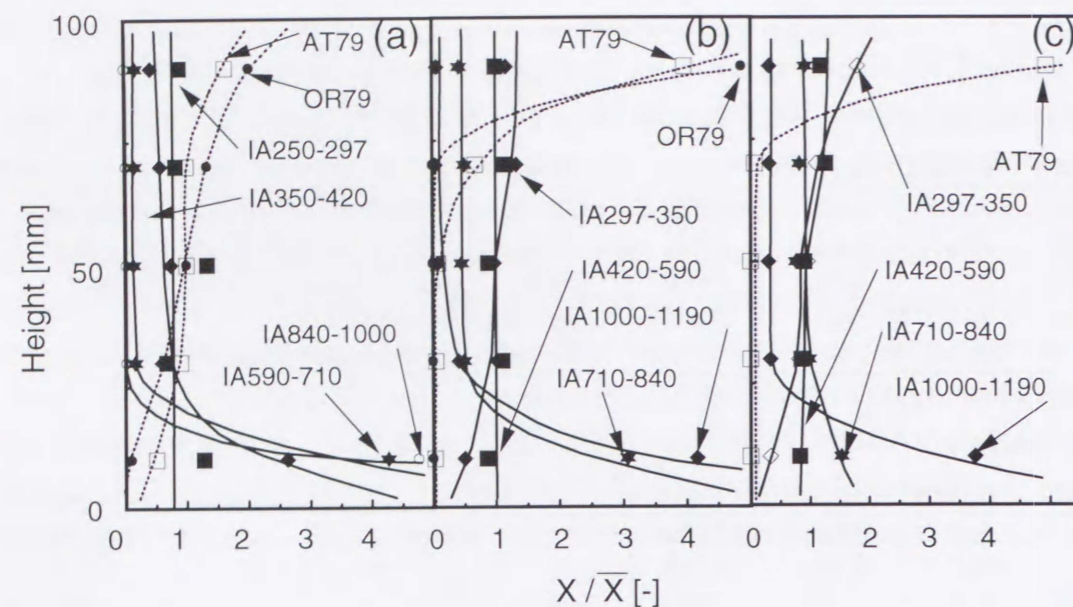
Fig. 4.4 Axial distribution of fines (AT79, OR79) and agglomerates (IA) in fluidized beds of (a) SiO_2 409µm, (b) SiC 522µm and (c) Al_2O_3 450µm after fluidization time of 180s (u - u_{mf} = 0.06m/s)
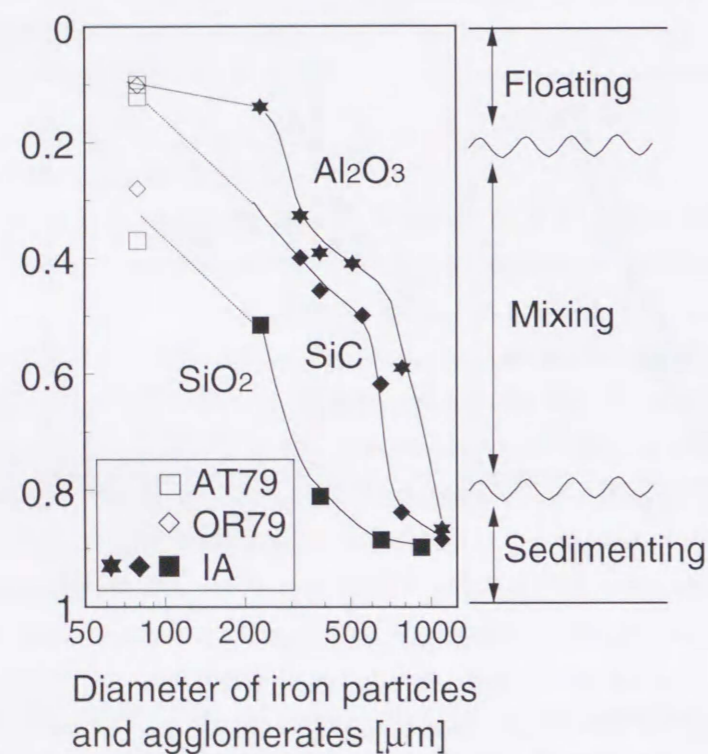

Fig. 4.5 Effect of particle diameter of raw iron oxide and iron agglomerates on segregation behavior

1000µm had tendency to sediment and settle at the bottom.

function of agglomerate size from data of Fig. 4.4. If l_{50}/L is less than 0.3, it can be assumed that particle is well segregated in the top region. When l_{50}/L is larger than 0.3 and less than 0.7, particle is supposed to be well mixed. If l_{50}/L is larger than 0.7 strong sedimentation tendency of particles occurred. When the particle density of bed materials (i.e. the floatation / sedimentation media) was increased, the diameter above which the agglomerates sediment increased. In the silica sand bed the AT79 and OR 79 particle did not segregate well and IA particles larger than 590µm sedimented to the bottom. The AT79 particle segregated well floating in the top region of the bed and the IA particles of larger than 710µm sedimented at the bed bottom, when SiC was used for the bed material. In the case of Al_2O_3 bed AT 79 and OR 79 particles also segregated to the top region well and IA particles of diameter larger than 1000µm was required to sediment them.

Agglomerates growing to a very large size should be avoided because it may cause defluidization and containment of bed materials in them. Moreover, raw iron materials have to be well segregated to the top region. Bed materials, SiC, of 500µm size is good this purpose. Accordingly, we selected the particle as the bed material for almost all over reduction experiments.

Fig. 4.6 shows the effect of superficial velocity on the segregation. Since l_{50}/L is close to 0.5, the silica sand bed did not show the signs of the segregating powder AT79. However, in the Al_2O_3 and the SiC beds the fluidizing gas velocity scarcely affected the segregation for both AT79 and IA

The sedimentation velocity was measured by the following methods. The gas flow was suddenly stopped to keep the situation of sedimenting particles in a fluidized bed at certain seconds after charging the iron agglomerates on the surface of the bed. The particles were then sampled from the several layers of the bed and weight fraction was obtained. The axial concentration profiles of iron agglomerates are shown in Fig. 4.7(a) as parameter of the switched off time, in which the sedimenting behavior can be clearly found. As demonstrated in Fig. 4.7(b), the sedimentation velocity was obtained from the slope of the average sedimentation distances calculated from the data of Fig. 4.7(b).

Fig. 4.8 shows the relation between the segregation velocity and the agglomerate diameter. The agglomerates of less than 500µm in diameter did not sediment to the bed bottom. The sedimentation velocity for agglomerates greater than 840µm are close to 1mm/s at u_0 = 0.47m/s. A significant finding here is that the sedimentation velocity is affected by the gas velocity u_0 and not relies much by the agglomerate diameter. Rowe et al. (1972)[2] stated that for the two-particle systems having not much difference between particle diameters, jetsam (heavy particles) tends to
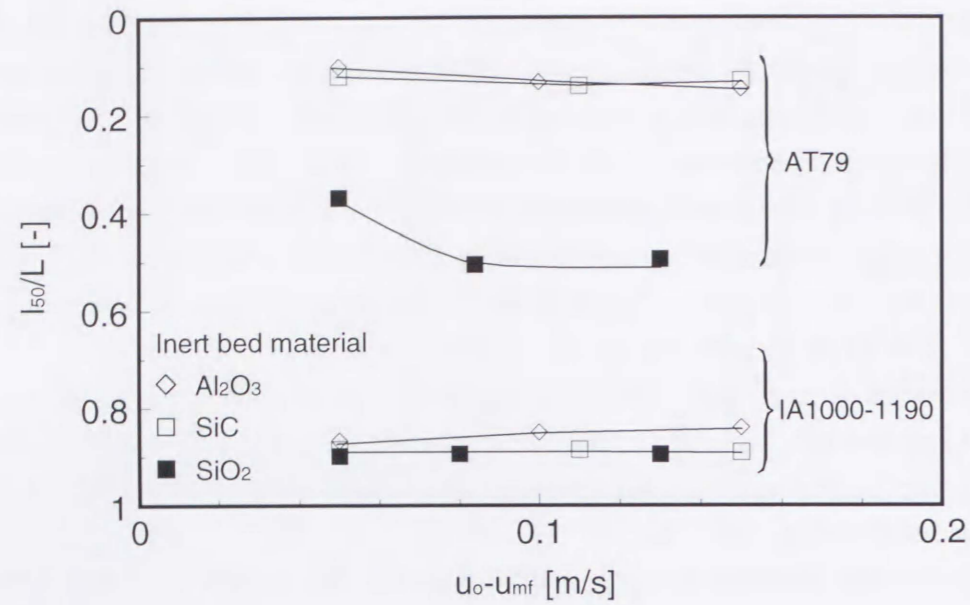
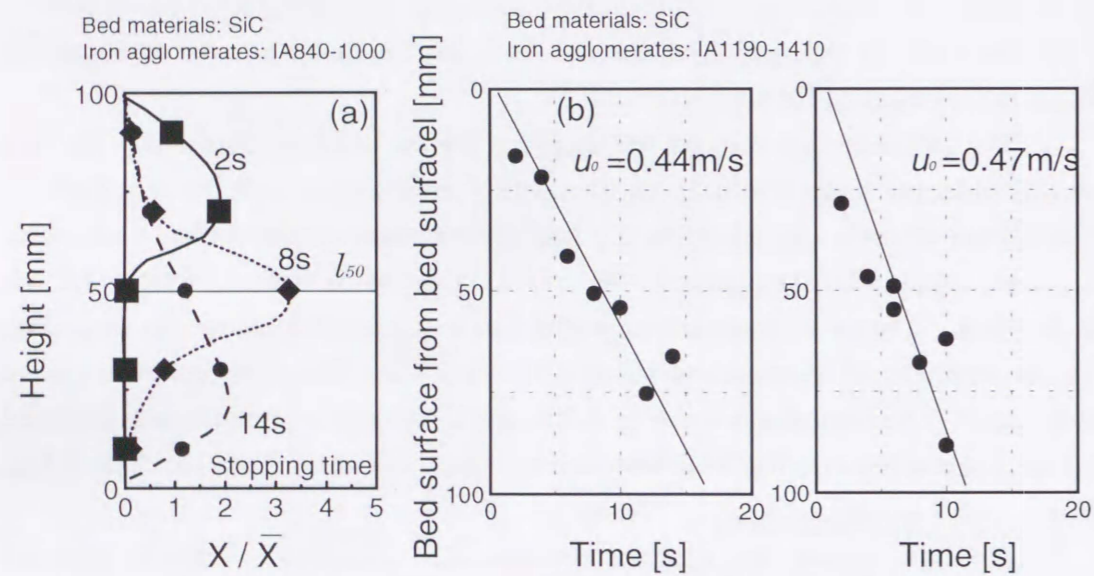Fig. 4.6 Effect of excess gas velocity on segregation

Fig. 4.7 Determination of sedimentation velocity, (a) transient response of axial distribution profile (Bed material: SiC, iron agglomerates: IA 840-1000) and (b) sedimentation distance of iron agglomerates (Bed material: SiC, iron agglomerates: IA 1190-1410)
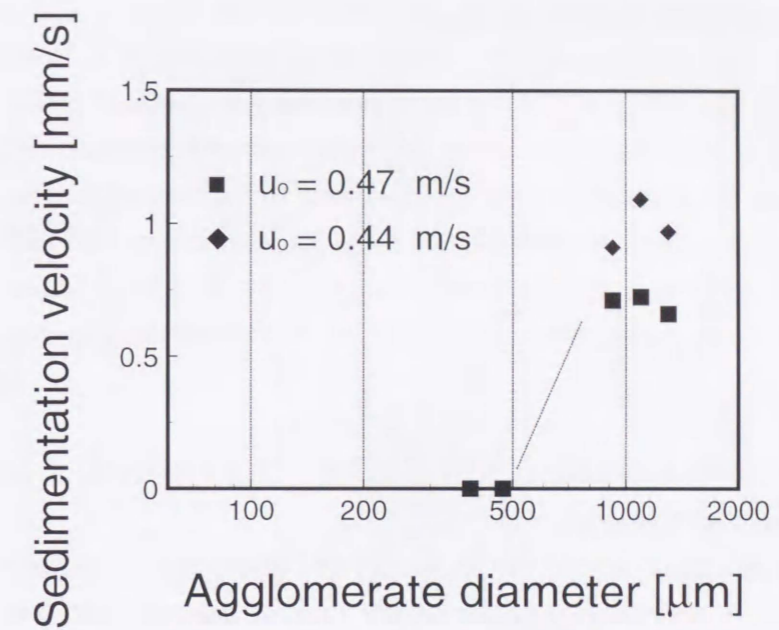
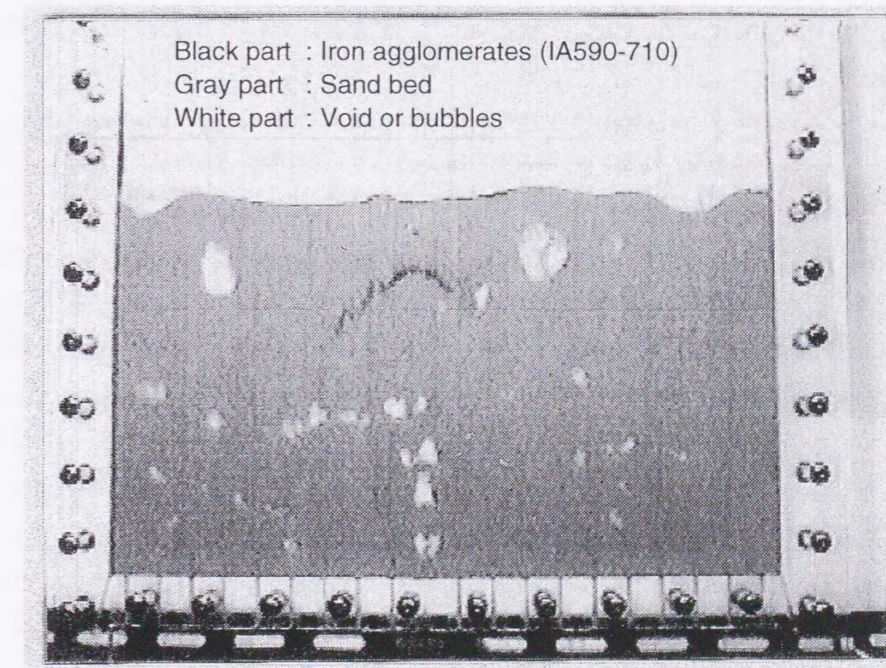Fig. 4.8 Sedimentation velocity of agglomerates obtained at $u_0 = 0.44$m/s and $u_0 = 0.47$m/s

Fig. 4.9 Photograph of sedimenting iron particles in a two-dimensional fluidized bed (400 x 5 x 200mm, $u_0 = 0.28$m/s)

sediment to the bottom making jetsam particle assembly called "islands," because jetsam can not penetrate flotsam (light particles) particle layers. The sedimenting behavior of iron agglomerates observed for a silica sand bed in a two-dimensional fluidized bed is shown in Fig. 4.9. The black part, the gray part and white part in Fig. 4.9 are iron agglomerate particles, silica sand bed and void, respectively. The iron agglomerates from the fluidizing surface sedimented to the bottom forming groups of islands. They sedimented intermittently but only at the time a bubble passes near the island. It is thought that the sedimentation velocity is mainly affected by not agglomerate size but by the bubble frequency which depend on the gas velocity.

4.3   BENCH SCALE EXPERIMENTS TO TEST THE PROPOSED MODEL

4.3.1   Apparatus and Experimental Procedures

A stainless steel fluidized bed of diameter of 43mm and height of 462mm was used (Fig. 4.10). A perforated plate having 61 holes of diameter of 0.6mm was used for the distributing of fluidizing gas. The bed fluidized by a mixture of Hydrogen: Nitrogen (= 3:1) was heated to specified temperatures. The mainly used bed material is SiC and the other materials (Al_2O_3 and ZrO_2) also used as bed materials. The unreduced water atomized iron particles (AT79, 0.02~0.05kg) were pneumatically fed on the surface of the fluidized bed using the fluidized bed elutriation feeder. Nitrogen gas was used for the pneumatic transportation. After the feeding the bed was fluidized for 1800sec.

Table 4.2 shows the chemical composition of raw iron particles and reduced agglomerates.

4.3.2   Particle Behavior of Iron Oxide and Iron Agglomerate during Reduction

Fig. 4.11 shows the schematic illustration of the bed of various bed materials after reduction. In the SiC bed, AT79 particle formed agglomerates and they sedimented to the bottom of the bed. In the case of Al_2O_3 bed, the agglomerates were found not to sediment at the bottom. With the ZrO_2 bed, all iron particle agglomerate sintered and floated on the bed surface. This tendency agrees well with the cold model test. The obtained agglomerate density, 4000kg/m³, is quite less than that of ZrO_2, 6050kg/m³. This is the reason for iron agglomerates not to settle down in the bed.

The temperature effect on the diameter of iron agglomerates in the case of SiC bed is delineated in Fig. 4.12. The mean diameter of iron agglomerates increased with temperature. The small agglomerates obtained at 873K did not sediment to the bottom. This agrees well with the results of the cold model test on segregation as has been depicted by Fig. 4.5. Round shaped agglomerates whose diameter ranged from 0.8 to
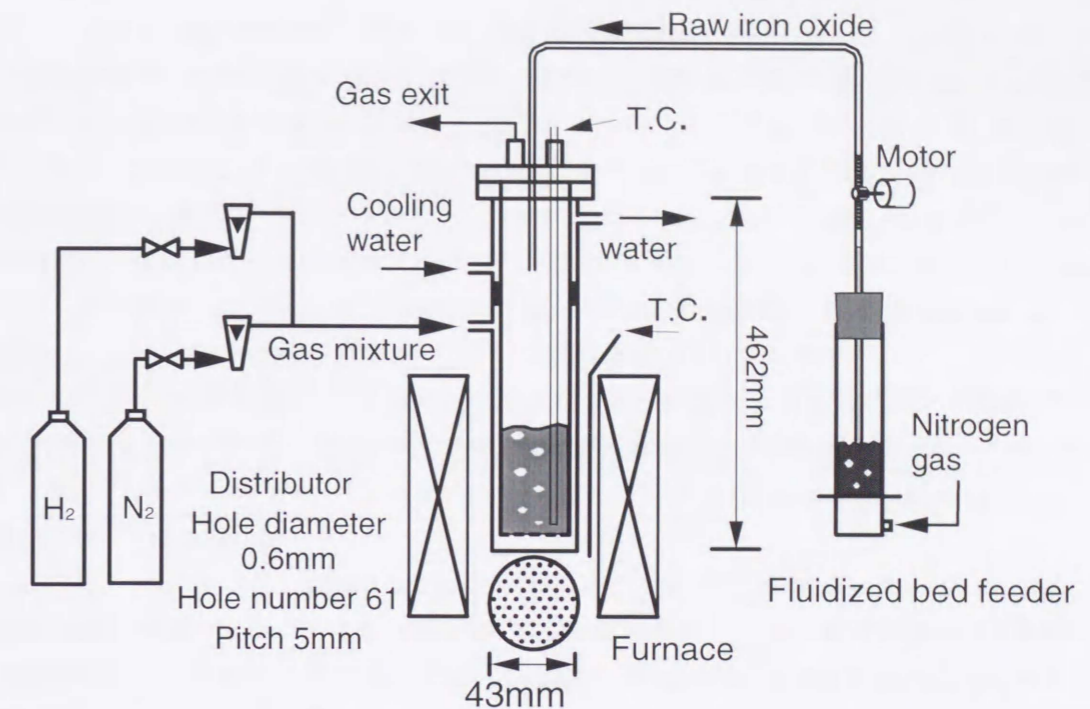

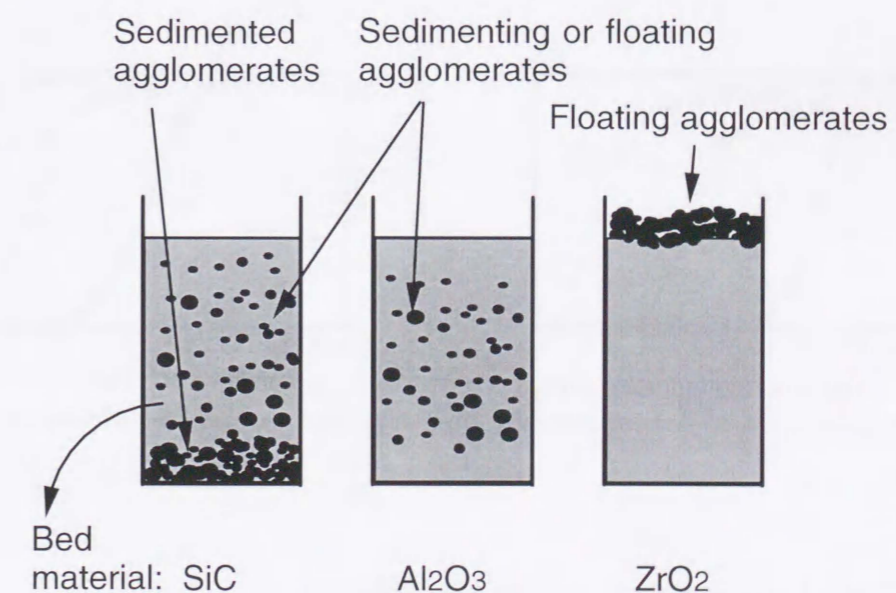Fig. 4.10 Bench scale experimental apparatus of bench scale test

Fig. 4.11   Schematic illustration of bed after reduction

Table 4.2   Chemical analysis of iron powder (% wt)

	Fe	O	C	Si	P	S	Mn
Water atomized raw iron powder	99.1	0.55	0.12	0.01	0.011	0.013	0.22
Iron agglomerate after reduction (973K)	99.5	0.18	0.10	0.02	0.014	0.013	0.21

(a) Feed : unreduced water atomized iron powder 60g

(b) Feed : reduced water atomized iron powder 60g

Bed material : SiC   ■ H₂ : 15.0 *l*/min (at 298K)   □ H₂ : 18.8 *l*/min (at 298K)
                        N₂ : 5.0 *l*/min (at 298K)   N₂ : 6.3 *l*/min (at 298K)
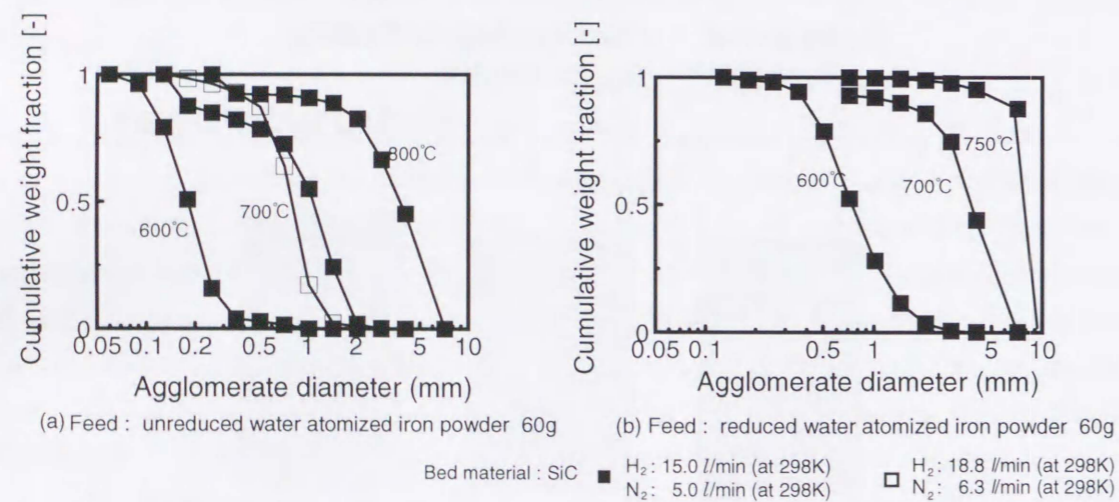
Fig. 4.12   Agglomerate diameter after reduction

2mm were formed at 973K and sedimented to the bed bottom of the bed (Fig. 4.13(a)).

The aggloerates obtained at 873K and 973K were round shaped. Agglomerates of irregular shape grown to 5mm~10mm size were formed at 1073K. These agglomerates contained bed particles within them (Fig. 4.13(b)). It is thought that they consisted of smaller agglomerates as clearly observed in the cross section of agglomerates shown in Fig. 4.14. Since sedimented agglomerates were not removed from the bed in our experiments, possibly, reagglomeration of sedimented agglomerates might occur in the bottom region of the bed. The chemical composition of the agglomerates analyzed by Inductively Coupled Plasma Spectrometry (ICP) is given in Table 4.2. The concentration of oxygen in the iron particles decreased from 0.55%(wt) to 0.18%(wt) at 973K. The concentration of Carbon, however, decreased only from 0.12%(wt) to 0.10%(wt). This indicated that decarbonization is required before the reduction of iron oxides.

The effect of surface cohesiveness on the fluidization behavior and on agglomerates diameter the pre-reduced water atomized powder (AT57R) was also fed into the fluidized bed. The diameter of agglomerates was found to increased with the reduction temperature. However, the mean agglomerate diameter obtained for the pre-reduced powder was larger, sparse and irregular in shape than that of unreduced iron powder. The pre-reduced iron powder did not have iron oxide layer on its surface, and hence all particles were supposed to have had strong cohesion force immediately after feeding.
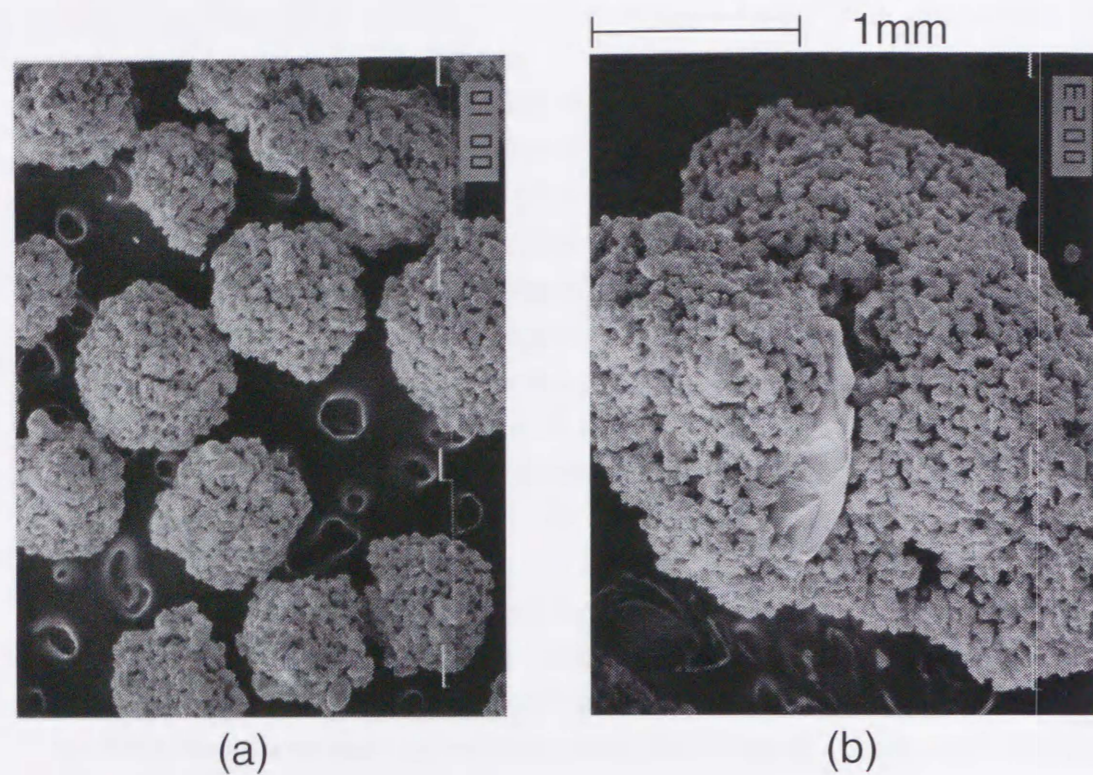
(a)　　　　　　　　　　　　(b)

Fig. 4.13　　　　SEM images of agglomerates obtained at (a) 973K, (b) 1073K
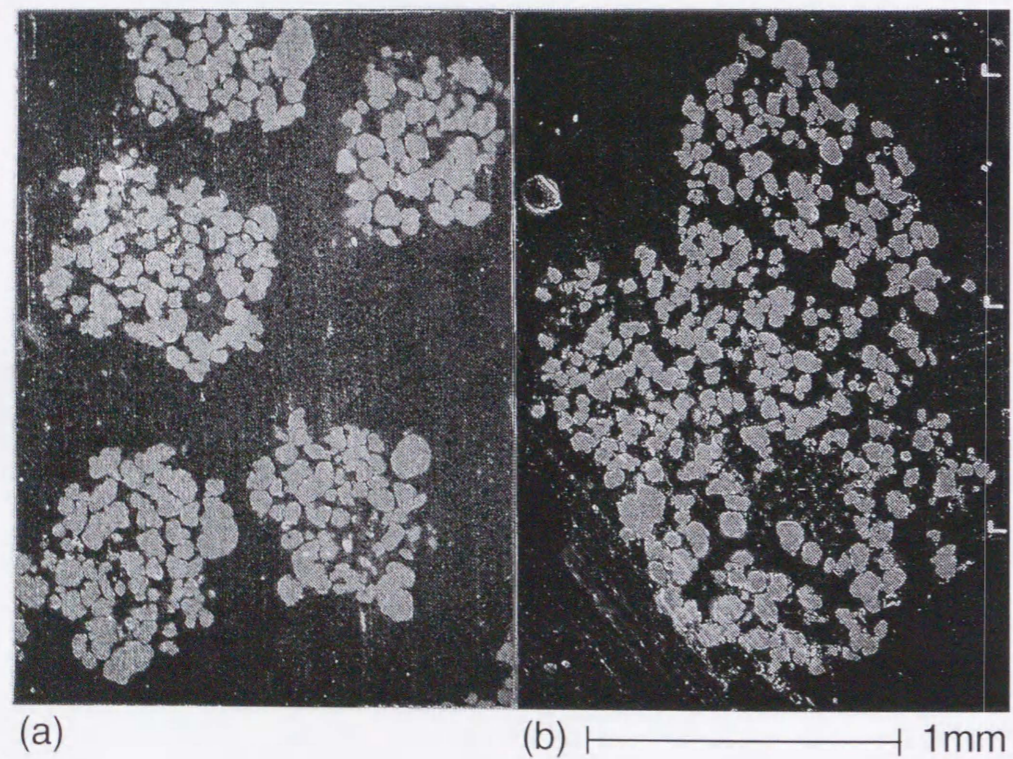

(a)　　　　　　　　　(b) ⊢————————⊣ 1mm

Fig. 4.14　　　　Cross section of agglomerates obtained at (a) 973K, (b) 1073K

4.4　CONCLUSIONS OF CHAPTER 4

A process for the production of iron powder through spontaneous agglomeration and sedimentation in a fluidized bed was proposed. During reduction the raw iron oxide powders were segregated in the upper region of the bed reducing by the difference of the particle diameter. The reduced iron particles agglomerated due to their stickiness and sedimented to the bottom. Both cold and hot experiments that:

1. The raw iron oxide particles segregated well in the upper region of the bed and iron agglomerates lager than 1000μm sedimented to the bottom at a velocity of 1mm/s in SiC sand bed of 522μm in cold experiments.
2. The formation of agglomerates and their sedimentation without defluidization was confirmed at 973K by reduction experiment.
3. The agglomerate size increased with the reduction temperature and irregularity in forming agglomerate also increased with the temperature.

REFERENCE

1) Morioka, Y., "Jyunteppun no seizougijyutsu, Dai 83 kai Nishiyama kinen gijyutsukouza, the Iron and Steel Institute of Japan, Tokyo, Japan (1982) 11

2) Rowe, P. N., A. W. Nienow and A. J. Agbim, "The mechanisms by which Particles Segregate in Gas Fluidized Beds – Binary Systems of Near-Spherical Particles," *Trans. Inst. Chem. Engrs.* **50** (1972) 310

CHAPTER 5

SUMMARY OF FINDINGS AND CONCLUSIONS

CHAPTER 5

SUMMARY OF FINDINGS AND CONCLUSIONS

The objective of this work is to contribute to advanced knowledge on fluidization of cohesive particle and to suggest the control strategy. Experimental investigations were carried out for iron particles as an example and a numerical simulation model was developed to predict the behavior of fluidized beds of cohesive particles. The results are summarized in the following with the recommendations on future research.

In CHAPTER 2, attention has been paid to the cohesion phenomena and cohesion forces on particles have been quantified.

Regression expressions for liquid bridge forces, as a function of liquid bridge volume, distance between surfaces and contact angle, and for critical rupture distance of a neck as a function of liquid bridge volume and contact angle for particle - particle and particle - wall contact were developed taking into account of the liquid bridging mechanisms described by the Laplace-Young equation.

Experimental investigation was carried out to investigate solid bridge force in typical case of iron particles at high temperature. The following results were obtained. The observed neck growth process below 1173 K was found to agree with the prediction of surface diffusion model. The cohesion force between iron particles depended on particle-particle contact time. The cohesion force of iron powder was measured by the diametral compression test. The solid bridge force can be estimated using neck area and tensile strength of neck, σ_{neck}. The neck tensile strength, σ_{neck}, was found to be constant below 1223K and was measured to 20MPa which was one twentieth of that of bulk steel. The tensile strength of neck, σ_{neck}, was estimated also by the method of bed breaking velocity and the predicted values agreed well with the data obtained from the diametral compression test. The surface roughness was important factor at relatively low temperature and the curvature of surface roughness was taken into account for the estimation of neck diameter. These result showed that the method of bed breaking velocity is applicable to predict σ_{neck} for various powders which otherwise has be predicted by the bulk value or conventional length methods.

In CHAPTER 3, Discrete Element Method (DEM) based simulation model named as SAFIRE (Simulation of Agglomerating Fluidization in Industrial Reaction Engineering) was developed for the first time based on soft sphere interaction analyzing the behavior of the non-cohesive, liquid bridging and solid bridging powders for fluidization.

The bubble formation, coalescence, eruption and particle circulation for non-cohesive powders was animated and the results were all found to be close to realistic situations. The bed behavior predicted was not affected much by the magnitude of the spring constant, and restitution coefficient if the maximum overlap distance is within 10% of the particle diameter.

Regression equations for the liquid bridge forces and for the critical rupture distances that were developed in CHAPTER 2 were introduced into SAFIRE model. Fluidization behavior of liquid bridging particles was successfully predicted and shown to be realistic by means of animated video pictures. The increase in liquid volume of the bed enhanced the pressure fluctuations, especially at shallow bed condition, made bubbles of larger size with more irregular shape. Jets on the distributor were found to be more unstable. Computer experiments showed that the minimum fluidizing velocity for wet particles was higher than that of dry particles indicating the effect of agglomerate formation in the wet bed.

Corresponding experiments for both dry and wet fluidization was carried out using a bed of 200mm inner diameter and grass beads of 1mm. Although the minimum fluidization velocity at dry condition obtained by experiment was less than numerically obtained one, the deviation was within 30% error. This overestimation of minimum fluidizing velocity of dry particles can be attributed to the difference in packing behavior between real 3D bed and one-layer bed of spheres. The experimentally observed minimum fluidization velocity of wet powder increased with the liquid content and the tendency agreed well with the SAFIRE model prediction. Experimentally obtained pressure fluctuation of a deep wet powder bed is less than a dry deep bed. However, that of shallow wet bed was larger than dry shallow one. SAFIRE model predicted almost similar tendency that the difference in pressure fluctuation between dry and wet particles was decreased with increasing bed height.

The surface diffusion mechanisms discussed in Chapter 2, which dominates cohesiveness of the iron particles in fluidized beds at high temperature, was introduced into SAFIRE model and the behavior of solid bridging particles were successfully reproduced. The defluidizing part due to neck formation was found to formed at the bottom region between nozzles at first, and then, defluidizing zone grew toward the bed top forming channels. Corresponding that, absolute pressure dorp and fluctuation of

pressure drop decreased with time. This situation was very similar to the experimental result in Chapter 2.

Iron particles at high temperature is very sticky and it is difficult to fluidize and these are described with theory and mechanisms in CHAPTER 2 and 3. In CHAPTER 4, a fluidized bed process for very sticky particles that have strong tendency to agglomerate was studied and strategy to eliminate defluidization was proposed. The proposed novel process is for the iron powder production process through spontaneous agglomeration and sedimentation in a fluidized bed. The raw iron oxide powders during reduction segregate in the upper region of the bed by the reducing gas by virtue of the difference in particle diameters. The reduced iron particles agglomerate due to their stickiness and sediment to the bottom also due to the difference in particle size. The agglomerates at the bottom are finally discharged. The results on cold and hot rig experiments showed that:

1. The raw iron oxide particles segregated well in the upper region of the bed and iron agglomerate lager than 1mm sedimented at the bottom at a sedimentation velocity of 1mm/s in SiC sand bed of 522µm by cold experiment.
2. The formation of agglomerates and their sedimentation without defluidization were confirmed by hot reduction experiments at 973K.
3. The agglomerate size increased with the reduction temperature and the irregularity in the agglomerate also increased with the temperature.

The author believes that the present results can contribute to the progress in fluidization technology of cohesive powders and to promote further investigation for understanding of cohesiveness of a varieties of powders.

Especially, the development of a novel SAFIRE model would promote further understandings and advancement of computer simulated experiments to characterize the fluidization of cohesive powders. It is recommended to improve SAFIRE version by reducing the time step and run the model program in a super computer or a parallel-processing computer to analyze the bed behavior of large 3D systems.

List of Symbols

a : curvature radius [m]

A_b : bubble cross sectional area [m^2]

Ar : Archimedes number [-] $Ar = \dfrac{d_p^3 \rho_f \left(\rho_p - \rho_f \right) g}{\mu^2}$

A_t : cross sectional area of fluidized bed [m^2]

C : integration constant [-]

Ca : capillary number $Ca = \mu v / \gamma$ [-]

C_D : drag coefficient [-]

d_p : particle diameter [m]

$D_{0,s}$: frequency factor of surface diffusion [m^2/s]

$D_{0,v}$: frequency factor of volume diffusion [m^2/s]

D_b : bubble diameter [m]

D_{b0} : initial bubble diameter [m]

D_{bm} : maximum attainable bubble diameter [m]

D_d : test piece diameter [m]

D_s : surface diffusion coefficient [m^2/s]

D_t : bed diameter [m]

D_v : volume diffusion coefficient [m^2/s]

e : restitution coefficient [-]

E : Young modulus [N/m^2]

E_{ap} : apparent Young modulus [N/m^2]

E_s : activation energy of surface diffusion [J/mol]

E_v : activation energy of volume diffusion [J/mol]

$\mathbf{f}_i$: fluid- particle interaction force acting on a fluid cell [N]

$\mathbf{f}_{pi}$: particle-fluid interaction force acting on a particle[N]

F : force [N]

F_0 : fracture load [N]

F_b : force acting on one particle from a bubble [N]

F_{buoy} : bubble buoyancy force [N]

F_c : cohesive force [N]

F'_d : drag force acting on one particle [N]

F_d : drag force acting on the lowest particle in vertically aligned n particles at the bed breakage [N]

F_n : normal soft sphere interaction at contact[N]

F_t : tangential soft sphere interaction at contact[N]

g : gravity acceleration [m/s^2]

H : curvature of liquid bridge[m^{-1}]

$\hat{H}$: dimensionless curvature of liquid bridge ($= Hr_p$)

h : separation distance between particles[m]

h_c : critical rupture distance between particles[m]

$\hat{h}_c$: dimensionless critical rupture distance between particles ($= h_c/r_p$)[-]

I : moment of inertia of a particle ($(2/5)mr_p^2$[kg m^2]

k_B : Boltzmann constant [J/K]

k_n : spring constant for normal direction [N/m]

k_t : spring constant for tangential direction [N/m]

l_{50} : height above which 50% of iron particles or agglomerates present[m]

L : static bed height [m]

m : particle mass [kg]

n : number of particle layers in a bed[-]

N : number of particles in the periphery of a bubble [-]

n : number of particles in a fluid cell[-]

n_k : coordination number [-]

p : pressure [Pa]

ΔP_{bed}: pressure drop equivalent to bed weight [Pa]

ΔP_c : pressure drop due to powder cohesion [Pa]

ΔP_{tot} : total pressure drop of bed [Pa]

R : gas constant [J/mol K]

Re_p : particle Reynolds number [-] $Re = \dfrac{\rho_f u_0 d_p}{\mu}$

R_p : particle radius [m]

S_t : tensile strength [Pa]

T_d : duration of collision[s]

T : temperature [K]

t : time[s]

u : gas velocity[m/s]

u_0 : superficial gas velocity [m/s]

u_{bb} : bed breaking velocity [m/s]

u_{mf} : minimum fluidizing velocity [m/s]

u_{rel} : particle relative velocity at collision [m/s]

v : particle velocity[m/s]

v' : particle fluctuation velocity[m/s]

$\overline{\mathbf{v}}$: average particle velocity in a fluid cell[m/s]

V : liquid bridge volume [m^3]

$\hat{V}$: dimensionless liquid bridge volume ($= V/r_p^3$)

V_b : bubble volume [m^3]

V_p : particle volume [m^3]

w : mass of liquid in bed [kg]

W : test piece thickness [m]

W_p : total mass of particles in a column

x : horizontal coordinate [m]

$\hat{x}$: dimensionless horizontal coordinate ($= x/r_p$)

x_{neck} : neck radius [m]

x_c : half distance between three phase contact points [m]

x_n : normal overlap distance [m]

x_t : tangential relative displacement [m]

X : weight fraction of iron particles in a section of the bed[-]

$\hat{X}$: weight fraction ration to average weight fraction of iron particles in the whole bed[-]

y : vertical coordinate [m]

$\hat{y}$: dimensionless horizontal coordinate ($= y/r_p$)

y_0 : neck radius at center of liquid bridge [m]

Greek Symbols

δ : lattice constant [m]

γ : surface tension or energy [N/m]

ε : voidage [-]

ε_{mf} : voidage at minimum fluidizing condition [-]

ρ_f : gas density [kg/m^3]

ρ_p : particle density [kg/m^3]

σ_{neck} : tensile strength of a neck [N/m^2]

σ_t : tensile strength of the bulk [N/m^2]

ϕ : half filling angle [rad]

η : damping coefficient

μ : viscosity [Pa·s]

μ_f : gas viscosity[Pa.s]

μ_l : liquid viscosity[Pa.s]

μ : friction coefficient [-]

θ : contact angle [rad]

ω : angular velocity [1/s]

Θ : granular temperature [m^2/s^2]

APPENDIX A   Fluid Phase Equations for Computation Code

Finite Differential Equation

Fluid phase differential equations are rearranged to differential type equation for numerical computation.

Equation of Continuity

Eq. 3.11 is integrated with respect to space and then integrated with respect to time.

$$\int_{t-\Delta t}^{t}\int_{s}^{n}\int_{w}^{e}\int_{f}^{b}\left\{\frac{\partial\varepsilon}{\partial t}+\frac{\partial(\varepsilon u_i)}{\partial x_i}\right\}dxdydzdt=0 \tag{A.1}$$

We obtain the following equation.

$$\frac{\varepsilon_t-\varepsilon_{t-\Delta t}}{\Delta t}\delta x\delta y+(\varepsilon_e u_{xe}-\varepsilon_w u_{xw})\delta y+(\varepsilon_n u_{yn}-\varepsilon_s u_{ys})\delta x+(\varepsilon_b u_{zb}-\varepsilon_f u_{zf})\delta z=0$$

$$\tag{A.2}$$

Equation of Momentum Balance

$$\int_{t-\Delta t}^{t}\int_{b}^{f}\int_{s}^{n}\int_{w}^{e}\left\{\rho_f\frac{\partial(\varepsilon u_i)}{\partial t}+\rho_f\frac{\partial(\varepsilon u_i u_j)}{\partial x_i}+\varepsilon\frac{\partial p}{\partial x_i}+F_i\right\}dxdydzdt=0 \tag{A.3}$$

At first, Eq. 3.12 is integrated with respect to space.

For example in *x* direction, we obtain the following:

Time dependence term

$$\int_{t-\Delta t}^{t}\int_{b}^{f}\int_{s}^{n}\int_{w}^{e}\left\{\rho_f\frac{\partial(\varepsilon u_i)}{\partial t}_i\right\}dxdydzdt=\int_{t-\Delta t}^{t}\left\{\rho_f\frac{\partial}{\partial t}(\varepsilon u_x)\right\}\delta x\delta y\delta zdt \tag{A.4}$$

Convection term (by first order upwind method to prevent numerical instability)

$$\int_{t-\Delta t}^{t}\int_{b}^{f}\int_{s}^{n}\int_{w}^{e}\left\{\rho_f\frac{\partial(\varepsilon u_i u_j)}{\partial x_i}_i\right\}dxdydzdt$$

$$=\int_{t-\Delta t}^{t}\rho_f[\varepsilon u_x u_x]_w^e\delta y\delta zdt+\int_{t-\Delta t}^{t}\rho_f[\varepsilon u_x u_y]_s^n\delta x\delta zdt+\int_{t-\Delta t}^{t}\rho_f[\varepsilon u_x u_z]_f^b\delta x\delta ydt$$

$$=\rho_f\int_{t-\Delta t}^{t}\left\{\varepsilon_e\left(u_{xP}\max[0,u_{xe}]-u_{xE}\max[0,-u_{xe}]\right)+\varepsilon_w\left(u_{xP}\max[0,-u_{xe}]-u_{xW}\max[0,u_{xw}]\right)\right\}\delta y\delta zdt$$

$$+\rho_f\int_{t-\Delta t}^{t}\left\{\varepsilon_n\left(u_{xP}\max[0,u_{xn}]-u_{xN}\max[0,-u_{xn}]\right)+\varepsilon_s\left(u_{xP}\max[0,-u_{xs}]-u_{xS}\max[0,u_{xs}]\right)\right\}\delta x\delta zdt$$

$$+\rho_f\int_{t-\Delta t}^{t}\left\{\varepsilon_b\left(u_{xP}\max[0,u_{xb}]-u_{xB}\max[0,-u_{xb}]\right)+\varepsilon_f\left(u_{xP}\max[0,-u_{xf}]-u_{xF}\max[0,u_{xf}]\right)\right\}\delta y\delta xdt$$

$$=\int_{t-\Delta t}^{t}Cdt$$

$$\tag{A.5}$$

Additive term, A

$$A = \int_{t-\Delta t}^{t} \int_{b}^{f} \int_{s}^{n} \int_{w}^{e} \left\{ \varepsilon \frac{\partial p}{\partial x_i} + F_i \right\} dx dy dz dt = \int_{t-\Delta t}^{t} \left(\varepsilon \frac{\partial p}{\partial x} + F_i \right) dx dy dz dt$$

$$= \int_{t-\Delta t}^{t} \frac{\varepsilon_e + \varepsilon_w}{2} (p_e - p_w) \delta y \delta z dt + \int_{t-\Delta t}^{t} \frac{F_{ie} + F_{iw}}{2} \delta x \delta y \delta z dt$$

$$= \int_{t-\Delta t}^{t} A dt \qquad (A.6)$$

Secondly, the above terms are integrated with respect to time using implicit method as follows:

Time dependent term

$$\int_{t-\Delta t}^{t} \left\{ \rho_f \frac{\partial}{\partial t} (\varepsilon u_x) \right\} \delta x \delta y \delta z dt = \rho_f \left(\left[\frac{\varepsilon_e + \varepsilon_w}{2} u_x \right]_t - \left[\frac{\varepsilon_e + \varepsilon_w}{2} u_x \right]_{t-\Delta t} \right) \delta x \delta y \delta z \quad (A.7)$$

Another terms

Using implicit method:

$$\int_{t-\Delta t}^{t} (C - A) dt = [C - A]_t \Delta t \qquad (A.8)$$

Finally, the following result was obtained:

$$\rho_f \frac{\varepsilon_e + \varepsilon_w}{2} \frac{\delta x \delta y \delta z}{\Delta t} u_x = \left[\frac{\varepsilon_e + \varepsilon_w}{2} u_x \right]_{t-\Delta t} \rho_f \frac{\delta x \delta y \delta z}{\Delta t}$$

$$+ \rho_f \left\{ \varepsilon_e \left(u_{xP} \max[0, u_{xe}] - u_{xE} \max[0, -u_{xe}] \right) + \varepsilon_w \left(u_{xP} \max[0, -u_{xe}] - u_{xW} \max[0, u_{xw}] \right) \right\} \delta y \delta z$$

$$+ \rho_f \left\{ \varepsilon_n \left(u_{xP} \max[0, u_{xn}] - u_{xN} \max[0, -u_{xn}] \right) + \varepsilon_s \left(u_{xP} \max[0, -u_{xs}] - u_{xS} \max[0, u_{xs}] \right) \right\} \delta x \delta z$$

$$+ \rho_f \left\{ \varepsilon_b \left(u_{xP} \max[0, u_{xb}] - u_{xB} \max[0, -u_{xb}] \right) + \varepsilon_f \left(u_{xP} \max[0, -u_{xf}] - u_{xF} \max[0, u_{xf}] \right) \right\} \delta x \delta y$$

$$+ \frac{\varepsilon_e + \varepsilon_w}{2} (p_e - p_w) \delta y \delta z + \frac{F_{ie} + F_{iw}}{2} \delta x \delta y \delta z$$

$$(A.9)$$
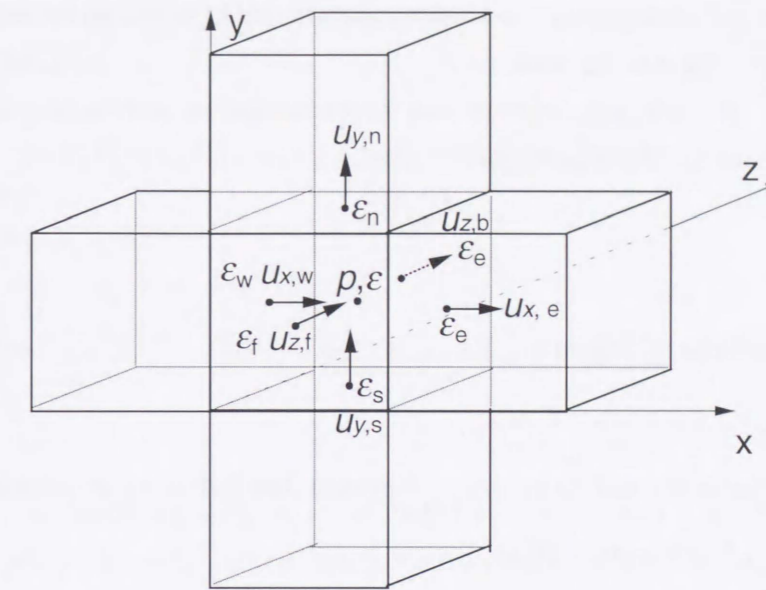
Fig. A.1   Control volume for equation of continuity

Control volume for momentum balance in x-direction
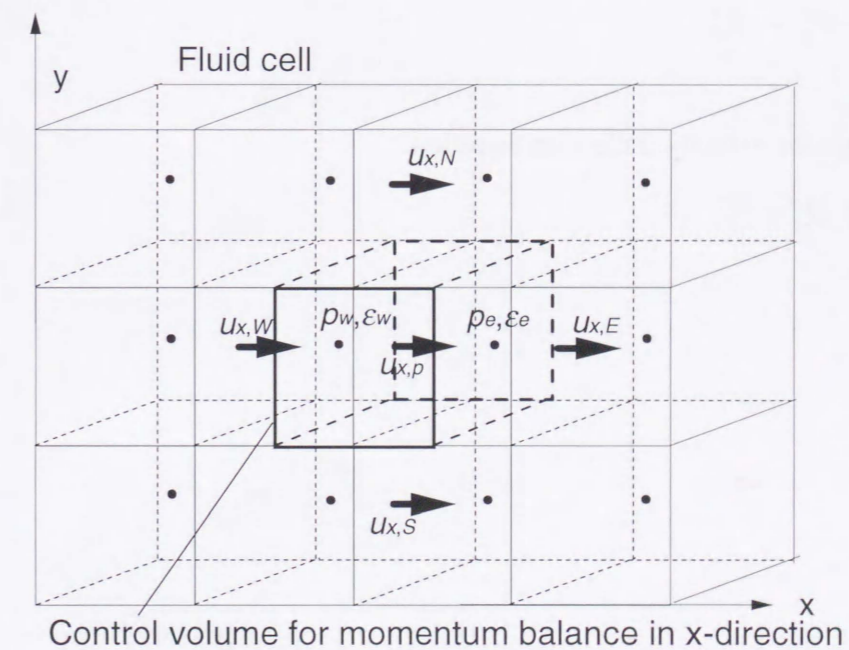
Fig. A.2   Control volume for x-direction momentum balance

Velocity Correction Equation

In order to converge the estimated values such as velocity and pressure, iterative calculations have to be done.

The true pressure and velocity can be expressed as summation of estimated value, u_i^* and P^*, and deviation p' and u':

$$P = P^* + P' \tag{A.10}$$

$$u_i = u_i^* + u_i' \tag{A.11}$$

Eq. (A.9) can be rewrite as follows:

$$a_x u_x = \sum a_{nb} u_{nb} + b + (P_P - P_E)A_x \tag{A.12}$$

The estimated value also satisfies the above equation, the following is obtained:

$$a_x u_x^* = \sum a_{nb} u_{nb}^* + b + (P_P^* - P_E^*)A_x \tag{A.13}$$

Subtracting Eq. (A.14) from Eq. (A.13) results in:

$$a_x u_x' = \sum a_{nb} u_{nb}' + (P_P' - P_E')A_x$$

The term $\sum a_{nb} u_{nb}'$ can be neglected [i] and then we obtain velocity collection term:

$$u_x' = d_x (P_P' - P_E') \tag{A.14}$$

where, $d_x = A_x / a_x$

Finally, we obtain the velocity collection equation:

$$u_x = u_x^* + d_x (P_P' - P_E') \tag{A.15}$$

Pressure Correction Equation

Substituting Eq. (A.15) into Eq. (A.2) we have equation of continuity for collected velocity:

$$a_P P_P' = a_E P_E' + a_W P_W' + a_N P_N' + a_S P_S' + a_T P_T' + a_B P_B' + b \tag{A.16}$$

where,

$$a_E = \varepsilon_e d_e \Delta y \Delta z$$

$$a_P = a_E + a_W + a_N + a_S + a_T + a_B$$

$$b = \frac{(\varepsilon_{P,t-\Delta t} - \varepsilon_P)\Delta x \Delta y \Delta z}{\Delta t} + [(\varepsilon u^*)_w - (\varepsilon u^*)_e]\Delta y \Delta z + [(\varepsilon u^*)_s - (\varepsilon u^*)_n]\Delta z \Delta x + [(\varepsilon u^*)_b - (\varepsilon u^*)_t]\Delta x \Delta y$$

where, P^* is estimated pressure, u_i^* is estimated velocity, p and u_i are true pressure and velocity, respectively, and p' and u' are deviations from the true value.

APPENDIX B   Heltzian particle contact

Goodier and Timoshenko's [ii] theoretical relationship between normal displacement, Δx, and normal load, F_n, was obtained taking into account the increased contact area by elastic deformation at a contact point as follows:

$$F_n = k_n \Delta x_n^{\frac{3}{2}}$$
$$k_n = \frac{\sqrt{d_p} E}{3(1-v^2)} \tag{B.1}$$

Mindlin and Deresiewicz [iii] analysis for relationship between tangential displacement and load considering the detailed sliding mechanism provedes the following results for tangential force and tangential spring constant:

$$F_t = k_t \Delta x_t$$
$$k_t = \frac{2\sqrt{d_p} G}{2-v} \Delta x_n^{\frac{1}{2}} \tag{B.2}$$

$$G_s = \frac{E_s}{2(1+v)}$$

d_p: particle diameter [m], E: Young modulus [Pa], v: Poison ratio [-], Δx_n: normal displacement[m], Δx_t: tangential displacement [m]

---

i) Patanker, S. V., Numerical Heat Transfer and Fluid Flow, Hemisphere Publishing 1980,
ii) Timoshenko, S. P. and J. N. Goodier, Theory of Elasticity, McGraw-Hill International editions, Singapore
iii) Mindlin, R. D. and H. Deresiewicz, Elastic spheres in contact under varying oblique forces., *J. Appl. Mech. (Trans. ASME)* **20**, 327

SUMMARY in JAPANESE

<div align="center">

学位論文和文要旨

液/固体架橋をもつ付着性粒子の凝集流動化とその制御

</div>

1．序論

流動層は、粉体ハンドリングのしやすさ、良好な気固接触などの利点により、広範囲の分野で使用されている。それらの工業化とともに、流動層工学も体系化され、流動層内の粒子の挙動はかなり明らかにされてきた。これまでの理論的体系化は固体粒子分散系の流体力学的解明とそれにもとづく固体—流体接触操作、特に固気接触操作の理論化であった。しかし、各種流動層操作において、粒子の付着凝集現象とそれに伴う流動化停止や造粒が重要な因子であることがますます広く認識されるようになった。実際にスプレー造粒はもちろん、ファンデアワールス力による微粉の付着・凝集造粒や、ポリオレフィンの重合反応での粒子同士の融着、シリコン気相析出や鉄の還元過程における表面拡散焼結による付着、石炭ガス化プロセスでの灰粒子の付着・凝集などは古くから問題になっている。付着力があると、粒子は２次粒子を作って流動化するが、さらに付着力が強い場合には粒子全体が互いに付着する流動化停止現象をひきおこす（Fig. 1）。このような粒子の付着・凝集挙動を予測・制御することは、そのプロセスの存亡をも左右するほど重要な因子である。にもかかわらず、これらの対策を勘や経験に頼っているのが現状であり、スケールアップへの指針も乏しく、流動層内の付着・凝集挙動の解明が待たれている。

流動層内での粒子の付着・凝集現象を解析するためには、個々の粒子間の付着力発生機構と、ガスによって引き起こされる粒子の運動の詳細を理解する必要がある。粒子の付着凝集を起こす付着力のうち、ファンデアワールス力、液架橋力、などは一応理論的定式化がなされているが、固体架橋についてはほとんど明らかにされていない。また、そのような付着力と流動層内で粒子に働く力との関係は、ほとんど明らかにされていない。凝集や非流動化現象は、時間依存性のある非定常現象であり、流動層の粒子流体挙動の経時変化を知ることのできる、流動層直接数値シミュレーターの開発は不可欠であるが、付着性粒子の流動層シミュレーターに関する報告はまだない。

現在、流動層の数値シミュレーションには２種類の本質的に異なるモデルがある。一つは、２流体モデルで、粒子もガスと同じような連続体とみなせると仮定して、流体相、粉体相ともに Navier-Stokes 式を解こうとする方法である。このモデルでは、粒子相の構成方程式をどうするかという問題が解決されておらず、粒子ウエーク部から噴水状の粒子上昇流が生じてしまう Fountain Problem や、実際よりも尖ってしまうといった問題がある。もう一つは、個々の粒子の運動方程式を Laglangian 的に
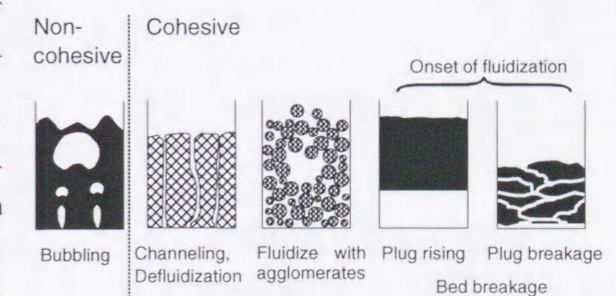
Fig. 1　付着性粉体の流動化

解くことによって、粉体層の挙動を明らかにしようとする離散要素法である。この方法では、粒子の個々の動きを追うので、計算モデルが単純であり、粒子付着力などの粒子間相互作用も、2粒子間のミクロな付着機構が解明されていれば、取り入れることが容易であり、また造粒などの現象への適応も、比較的簡単であると考えられる。

本論文では、現在の流動層工学において最も重要性の高い問題の一つである、付着性粒子の流動化挙動を解明し、さらにその工学的制御法について検討をおこない、付着性粉の流動層プロセスの基礎から開発までの工学的全体像を確立することを目的とした。まず、付着力自体の定式化については、機構の良く知られた液架橋力に関する簡便な推算式を提出し、また詳細が明らかでない固体架橋力に関しては、鉄粉の場合についての実験を含むケーススタディを行い、付着力増加機構の定式化法を明らかにした。つぎに、ソフトスフィア離散要素法に液架橋力および固体架橋付着力を導入した流動層の直接数値シミュレーター SAFIRE (Simulation of Agglomerating Fluidization for Industrial Reaction Engineering)を開発し、液架橋力よび固体架橋付着力を導入することにより、凝集流動化挙動の数値解析を行ない、非付着性粒子の流動化との比較検討を行った。さらに、ケーススタディとして固体架橋が起こるような金属粉プロセッシングの例に、付着凝集挙動を制御することのできる一つの流動層プロセスを考察し、その可能性を実験的に検討した。

2．流動層内の液・固体架橋付着力

付着性粉の流動化を理解するには、まず、付着力の原因を明らかにし、その定量化をしなければならない。ここでは、流動層造粒や、高温流動層において重要な付着力である、液架橋力と固体架橋力に着目した。液架橋力に関してはすでに、理論的定式化が一応確立しているものの、数式は極めて複雑で従来簡便な付着力および臨界破壊距離の推算式はなかった。そこで、Laplace-Young 式の繰り返し計算による数値解 (Fig. 2) を相関し、無次元付着力 $\hat{F}_c = F_c/\pi r_p \gamma$、無次元架橋破壊距離 $\hat{h}_c = h_c/r_p$ をそれぞれ、無次元液架橋量 $\hat{V} = V/r_p^3$、無次元粒子間距離 $\hat{h} = h/r_p$、接触角 θ の陽関数として以下の表現を得た。

$$\hat{F}_c = \exp(A\hat{h} + B) + C \tag{1}$$

粒子間については： $A = -1.1\hat{V}^{-0.53}$

$$B = (-0.34\ln\hat{V} - 0.96)\theta^2 - 0.019\ln\hat{V} + 0.48 \tag{2}$$

$$C = 0.0042\ln\hat{V} + 0.078$$

粒子と平面(壁)間では： $A = -1.9\hat{V}^{-0.51}$

$$B = (-0.016\ln\hat{V} - 0.76)\theta^2 - 0.12\ln\hat{V} + 1.2 \tag{3}$$

$$C = 0.013\ln\hat{V} + 0.18 .$$

臨界液架橋力破壊距離は：

粒子間については： $\hat{h}_c = (0.62\theta + 0.99)\hat{V}^{0.34} \tag{4}$

粒子と平面(壁)との間では： $\hat{h}_c = (0.22\theta + 0.95)\hat{V}^{0.32} . \tag{5}$
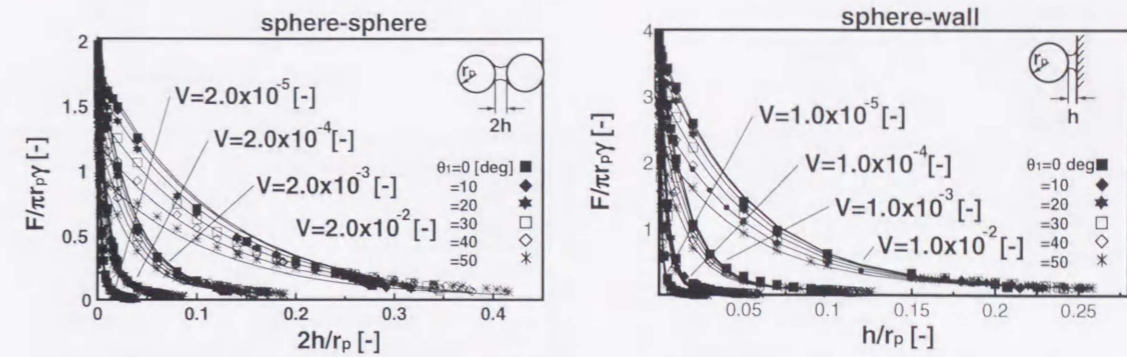
Fig. 2 Laplace – Young 式の回帰計算により得られた液架橋力と架橋が切れる点
(a) 粒子間、(b)粒子－平面間

つぎに、詳しい機構が明らかにされていない高温固体架橋力に関しては、鉄粉の場合について実験的検討を行なった。水素雰囲気中で高温処理したモデル鉄球粒子（$d_p = 200\mu m$）間の SEM 観察(Fig. 3)により焼結ネックの成長を直接観察し（Fig. 4）、鉄粉の高温付着力は、粒子間の表面拡散現象（Eq. 6）によるネック形成により起こる時間依存型現象であることを明らかにした。また、焼結体の圧裂引張強度測定データ（から、Rumpf 式により接触点あたりの付着力を求め、さらに、観察されたネック断面積から、接触点単位断面積あたりの付着力を求めたところ 20MPa であり、バルクの鉄の値の1/20 であった（Fig. 5）。つぎに、流動層内で高温処理された粉体層を破壊するのに必要なガス流速の測定 (Fig. 6) により、付着力の発生しはじめる温度は 800K 付近であること、また、接触点単位面積当たりの力を求めたところ、圧裂引張り強度試験の結果と一致する結果を得た(Fig. 7)。773K における鉄球粒子の水素雰囲気における流動化実験では、最初は問題無く流動化しているものの、2500s 位から流動状態が悪くなり、4000s で完全に流動化が停止した(Fig. 8)。これらの結果より、固体架橋付着力がKuczynsik 式により説明できることを明らかにした。

$$x = \left(\frac{56\gamma\delta^4}{k_B T}D_s a^3 t\right)^{1/7} \tag{6}$$
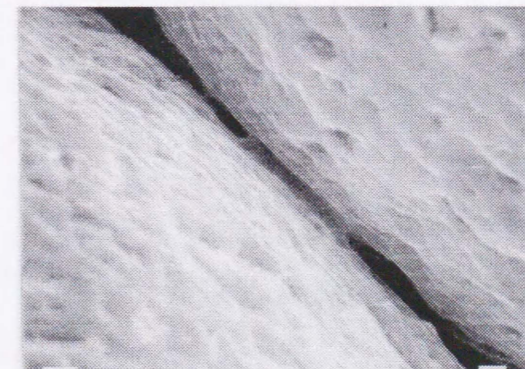
Fig. 3 観察されたネックの SEM 写真   Fig. 4 SEM 観察により得られたネック径
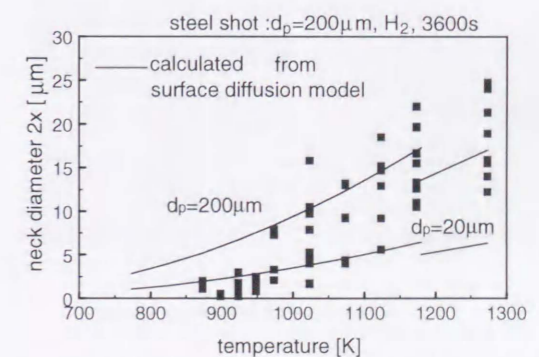
Fig. 5 ネック単位断面積あたりの付着力
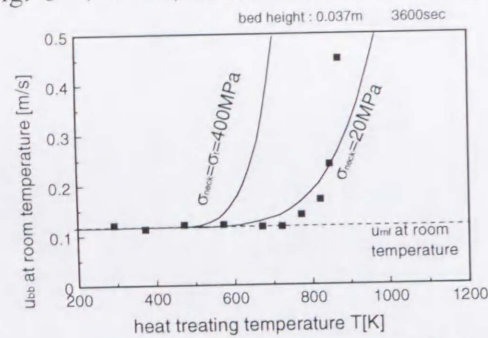

Fig. 6 熱処理粉体層の流動化曲線
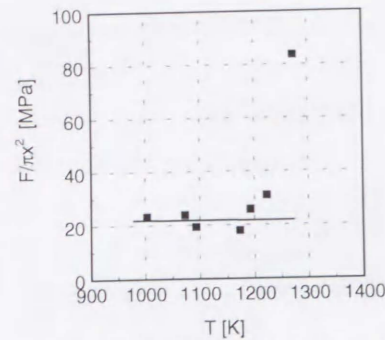
Fig. 7 粉体層破壊に必要なガス流速 u_{bb} の温度依存性

Fig. 8 スチールショット流動層の圧力損失変化と流動化停止(773K, u_0=0.24m/s)

３．凝集流動化挙動の数値解析

本章では、ソフトスフィア離散要素法に基づいた直接シミュレーションモデル SAFIRE を開発し、第一原理から凝集流動化挙動の数値解析を行うことを目的とした。このモデルでは、粒子側に関しては、ソフトスフィア離散要素法 (Fig. 9) に基づいて重力、流体抗力、粒子間接触力および粒子－壁間接触力と粒子間付着力を考慮した Newton の運動方程式（Eq. 7）を解くことにより個々の粒子の軌跡を逐一追跡する。また流体側に関しては、連続の式 (Eq. 8) と Navier-Stokes 方程式（Eq. 9）を SIMPLE 有限差分法により解くことによって求めるものである。また粒子流体間相互作用（Eqs. 10, 11）は 2way で考慮される。Flow chart を Fig. 10に示す。

$$m\frac{dv}{dt} = F_{pi} + mg + F_{collision} + F_{wall} + F_{cohesive}, \qquad (7)$$

$$\frac{\partial \varepsilon}{\partial t} + \frac{\partial(\varepsilon u_i)}{\partial x_i} = 0 \qquad (8)$$

$$\rho_f \frac{\partial(\varepsilon u_i)}{\partial t} + \rho_f \frac{\partial(\varepsilon u_i u_j)}{\partial x_j} = -\varepsilon \frac{\partial p}{\partial x_j} - F_i \qquad (9)$$

$$f_i = \left(150\frac{(1-\varepsilon)^2}{\varepsilon}\frac{\mu_f(u-\bar{v})}{d_p^2} + 1.75(1-\varepsilon)\frac{\rho_f(u-\bar{v})|u-\bar{v}|}{d_p}\right) \quad \varepsilon < 0.8 \qquad (10)$$

$$f_{pi} = \frac{\pi}{8}C_D' \rho_f \varepsilon^2 (u-v)|u-v|d_p^2 \qquad \varepsilon > 0.8 \qquad (11)$$

Fig. 9 粒子接触モデル

Fig. 10 SAFIRE モデルのフローチャート

３．１非付着性粒子のシミュレーション

まず、付着力のない粒子の気泡流動化シミュレーションを行った。均一流動化状態の層内に単一ノズルからパルスジェットを吹き込んで、単一気泡の上昇シミュレーションをおこない (Fig. 11)、実験によって良く知られたものと同様のウェークをもつ気泡が発生し上昇していくことが確認された。グラニュラーテンペラチャーは、気泡の生成時の上部と、ウエークを含む気泡の下部で高いということがわかった。6 つのガスノズルを持つフリーバブリングシミュレーションでは、気泡の発生、合体、破裂および粒子の大規模な循環運動も、きわめて現実的に再現された。最小流動化速度を数値実験的に求めたところ、2 次元条件であるものの、経験式である Wen-Yu 式から求められた値とほぼ一致する結果が得られた。各種モデルパラメーターの影響を調査し、ばね定数は、衝突によるかみこみ量が粒径の 1 割以下程度であれば結果に影響しないこと、反発係数は結果にほとんど影響しないこと、一つの流体セル中には最大 10 個程度の粒子数が必要であることを明らかにした。また 3 次元シミュレーションも行い、ウエークによって引きずられ上昇する粒子の様子などを再現した。

Table 1 計算条件

| Particles	
number of particles	14000
particle density	2650kg/m³
particle diameter	1.0mm
Collision parameters	
restitution coefficient	0.9
friction coefficient	0.3
spring constant	800N/m
Fluid : air	
viscosity	1.75×10⁻⁵Pa s
density	1.15 kg/m³
Computational grid parameters	
number of fluid cells	41 x 105
time step	2.58 x 10⁻⁵s
Fluidized bed parameters	
bed scale	0.154 x 0.3825m
number of nozzles	6 or 1
opening diameter	3.7mm
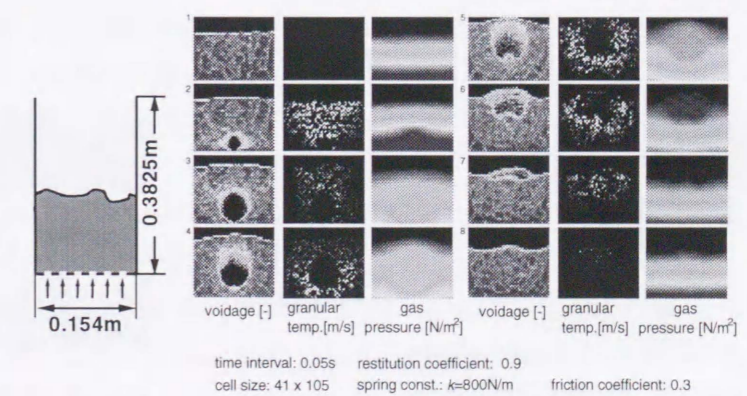
Fig. 11 単一気泡上昇シミュレーション結果(空隙率、粉体層力学温度、ガス圧力)
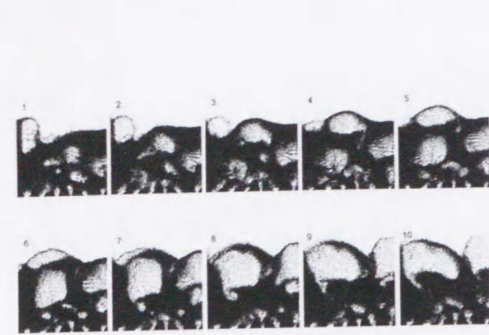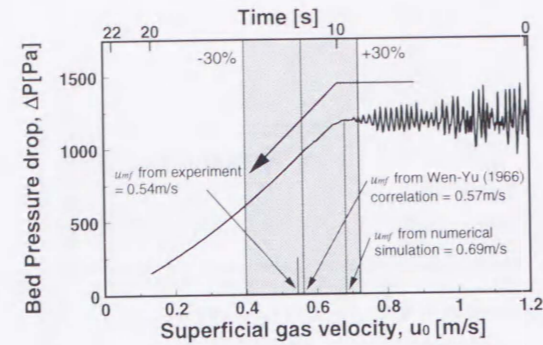
Fig. 12　フリーバブリング時の層内粒子の挙動（$u_0 = 1.2$m/s）

Fig. 13　SAFIRE モデルによる最小流動化速度の測定

3．2　液架橋を持つ粉体の流動化シミュレーション

つぎに、液架橋力が働く粉体のシミュレーションに関して、第 2 章で得た付着力と臨界破壊距離に関する回帰式を SAFIRE コードに導入しシミュレーションをおこなった。粒子は、1/2V の大きさの液滴をその表面に（2 次元の場合は 6 個、3 次元の場合は 12 個）持ち、接触すると粒子間に体積 V の液架橋が形成され、粒子間距離が臨界破壊距離を超えると液架橋がきれ、液滴は元の粒子に戻るというモデルである（Fig. 14）。$V = 1.0 \times 10^{-2}$（含水率 0.54%、dry base）のときの、流動化挙動を Fig. 15 に示す。乾いた粉体の挙動と全く異なり凝集体を作って流動化する様子が再現された。層の圧力変動は付着力のない場合と比べて、層高が低い(10cm)時は、顕著であり、層高が 20cm の時はほぼ同じという結果になった（Fig. 16, 17）。実験では、10cm の場合は液架橋がある方が大きく、20cm の場合は Dry な方が大きいという結果になり傾向的には一致する。流動化開始速度 u_{mf} も、液架橋が存在すると大きくなった。単一気泡を層内に導入した場合の結果を Fig. 17 に示す。グラニュラーテンペラチャーは、 dry な場合と似た傾向を示した。計算にかかる時間を Table 2 に示す。液架橋の導入はそれほど計算負荷を大きくしなかった。
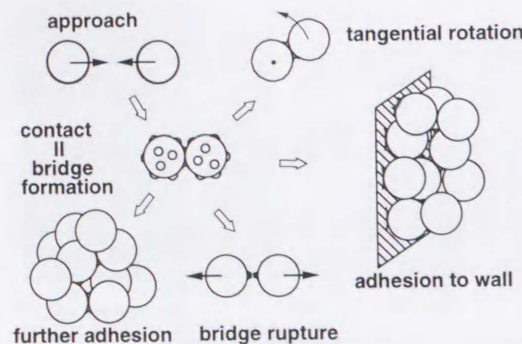
Fig. 14　流動層内液架橋モデル
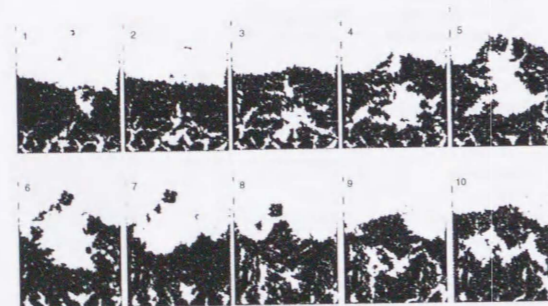
Fig. 15　液架橋のある場合の流動化シミュレーション（$V = 1.0 \times 10^{-2}$）
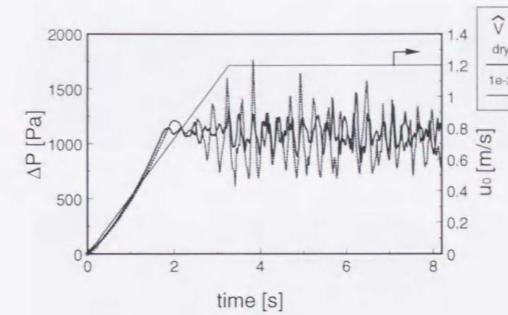
Fig. 16　液架橋がある場合とない場合の流動化時の層の圧力変動
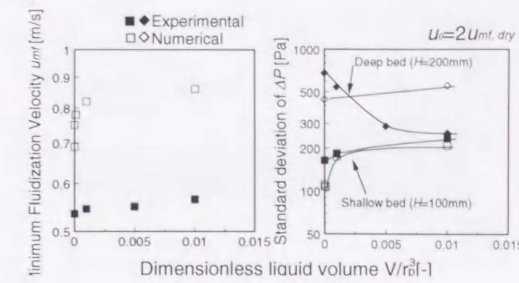
Fig. 17　umf と圧力変動の標準偏差への駅添加による影響

Fig. 18　単一気泡を吹き込んだときの層の挙動
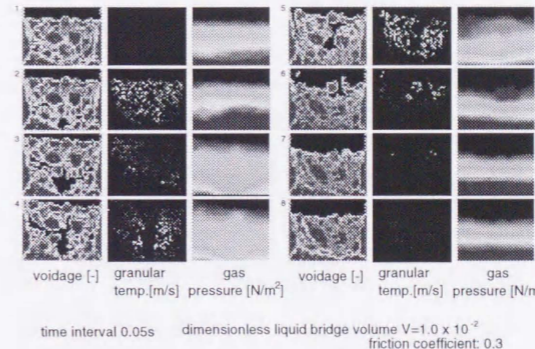
Table 2　CPU time on HP 9000 C110 for computation

	CPU time	al time
DRY	2.7 hour	1sec
WET	3.6 hour	1sec

Conditions: particles: 14000, fluid grid number: 4305, time step: 25.9μs

3．3　固体架橋を形成する粉体の流動化シミュレーション

固体架橋付着力に関して第 2 章で明らかにした Kuczynski 表面拡散式とネックの引張り破壊応力を SAFIRE モデルに導入して数値シミュレーションを行った。本モデルは粒子の接触時間に応じてネックが成長していき、ネックに働く力が、最大応力を超えるとネックが切れる。ただし粒子が衝突する場合の接触時間を求める場合には、Hooke 型でなく、真の鉄の弾性係数を用いた Hertz 理論によりもとめられる値を用いた。表面粗さを考慮した（表面粗度 20μm）とき、および、考慮しないときの 2 つのシミュレーションを行った。粒径 200μm のスチールショットの場合について、1273K での計算をおこなったときの圧力変動を Fig. 19 に示す。スナップショットを Fig. 20 に示す。時間とともに圧力損失の絶対値、変動ともに小さくなっており、また、スナップショットにおいて層内の分散板や壁近などの運動状態が不良なところから焼結が始まり、チャンネルが形成し、流動化が悪化していくことが明らかになった。この圧力損失低下の傾向は、実験とも一致する。これにより、鉄粉だけの流動層では、安定な流動化は難しいということが示唆された。
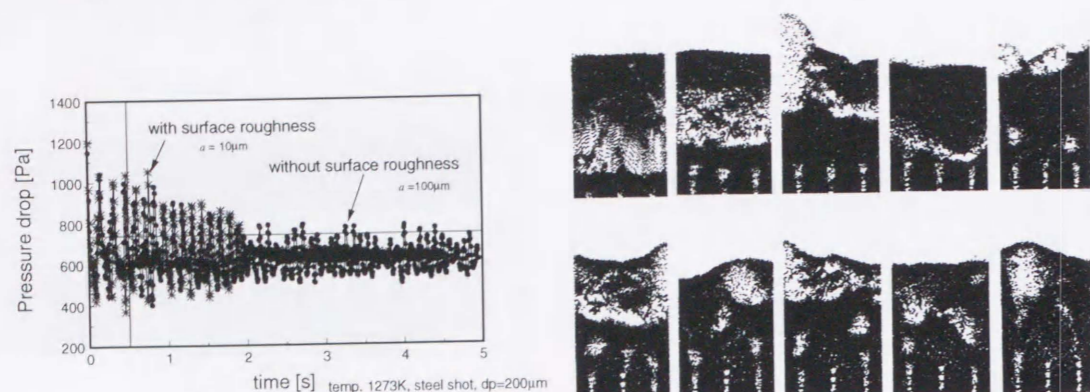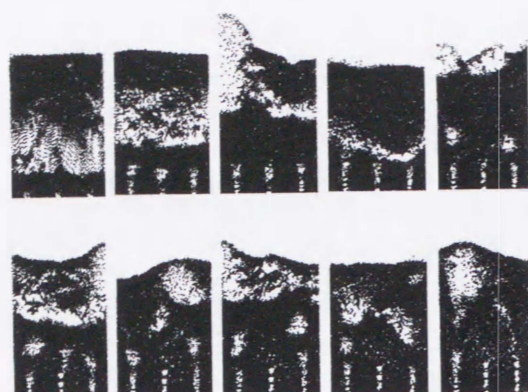
Fig. 19 固体架橋を持つ粒子の高温流動化時の圧力損失

Fig. 20 固体架橋を持つ粒子の流動化挙動スナップショット($a=100\mu m$, $\Delta t = 0.325$s)

- Unreduced iron oxide particles are segregated in upper region of a fluidized bed.
- When iron oxide particles are reduced to some extent, they begin to agglomerate.
- When agglomerates grow beyond to some critical size, they start sedimenting to the bed bottom.
- Bed height is adjusted to complete reduction during sedimentation.
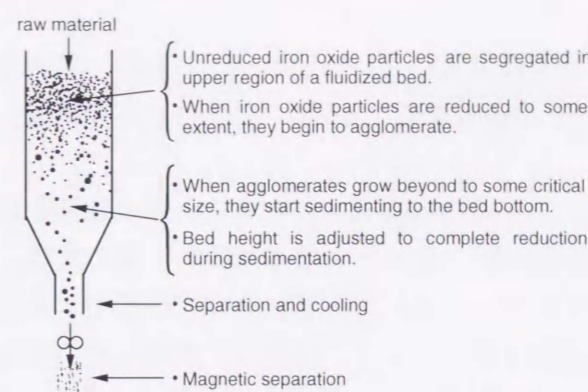- Separation and cooling
- Magnetic separation
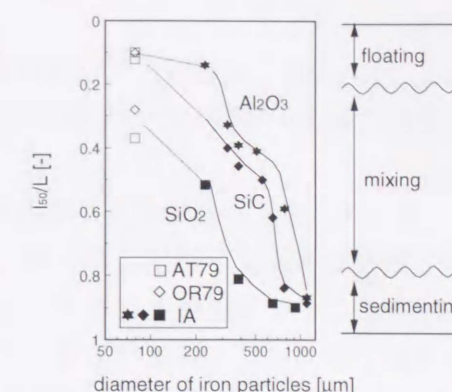
Fig. 21 凝集を制御できる新しい鉄粉製造法のコンセプト

Fig. 22 原料酸化鉄粉及び還元鉄粉凝集体の粒径が平均沈降距離 l_{50} におよぼす影響
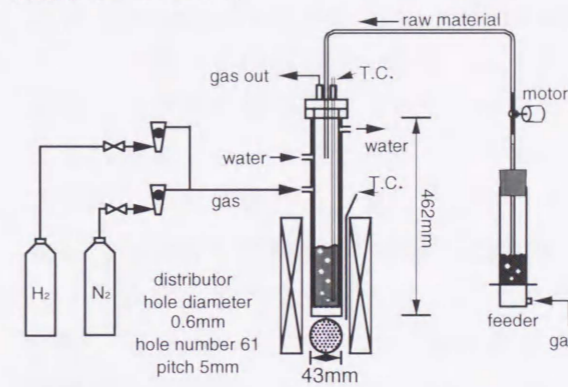
Fig. 23 ベンチスケール還元実験装置

Fig. 24 還元後の層内の鉄粉の分布状況模式

4．流動層内の凝集現象の制御についての検討 ——ケーススタディ：不活性媒体粒子による希釈効果を用いた鉄粉凝集制御——

　本章では、高温流動層中での金属粒子の焼結現象のような非常に強い付着力を制御する工学的方法を確立することを目的とした。ケーススタディとして、最も代表的で重要な高温付着性流動層プロセスであり、また付着凝集現象が制御できないためにほとんど実用化されていない流動層鉄粉還元の場合について、流動層内での粒子の凝集現象を制御し、非流動化現象を確実に回避する新しいプロセスの可能性を実験的に検討した。このプロセスは、不活性粒子で鉄粉を希釈する事により過度の凝集体成長とそれによる流動化停止を防ぎ、また、偏析現象を利用して未還元粉を層上部に滞留させ、凝集体を沈降させる事により抜き出す連続操作が可能なものである (Fig. 21)。本プロセス概念の検証のために、常温装置により、人為的偏析現象を起こすのに適切な媒体粒子および操作条件を明らかにした。3 種類の媒体を用いた時の原料酸化鉄粉および鉄粉凝集体の流動層内軸方向濃度分布のデータから鉄粉の平均沈降距離 l_{50} を求めると Fig. 22のようになり、SiC 砂を用いると、原料鉄粉が十分上部に偏析し、また 700μm 以上の大きさになった凝集鉄粉が沈降することがわかった。次に、バッチ型ベンチスケール高温還元実験装置 (Fig. 23) により、水アトマイズ表面酸化鉄粉を還元した。Fig. 24に見られるように、SiC 砂を使うと、酸化鉄粉は流動化停止することなく還元され、凝集体を形成し、ある程度の大きさになると沈降した。SiC を用いた場合の還元後の鉄粉凝集体 (Fig. 25) の粒度分布を Fig. 26に示す。還元鉄中の酸素濃度は粉末冶金粉に要求される 0.2% 以下になった。
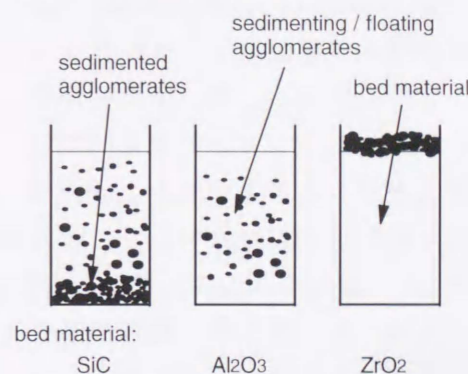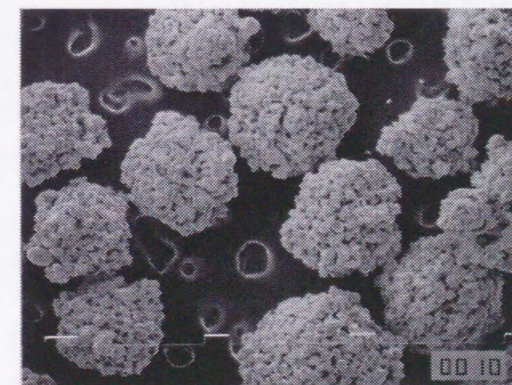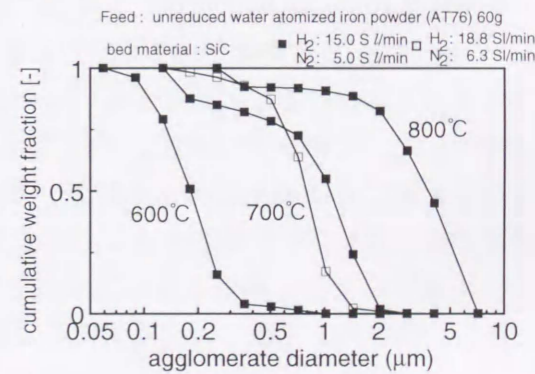

Fig. 25 得られた凝集体の SEM 写真

Fig. 26 生成した鉄粉凝集体の粒度分布

５．結論

　本論文では、現在の流動層工学において最も重要性の高い問題の一つである、付着性粒子の流動化挙動を解明しその制御法について検討をおこない、以下のような結論を得た。

　第 2 章では、まず、機構の良く知られた液架橋力に関して、付着力と臨界破壊距離に関する簡便な推算式を提出した。また詳細が明らかでない固体架橋力に関しては、鉄粉の場合についての実験を含むケーススタディを通して、ネックの直接観察、圧裂引張り強度試験および、焼結層破壊ガス速度の測定により、付着力を測定しその増加機構を解明し、固体架橋力の定式化法を明らかにした。

　第 3 章では、ソフトスフィア離散要素法に基づく流動層の直接数値シミュレーターSAFIRE (Simulation of Agglomerating Fluidization for Industrial Reaction Engineering)を開発し、流動層の直接数値シミュレーションを行った。まず、付着力のない場合のシミュレーションを行ない、単一気泡の挙動や、フリーバブリングの挙動を観察し、現実性の高いシミュレーション結果を得た。グラニュラーテンペラチャーは、気泡の下部および気泡が発生時の生成気泡上部で高いことを示した。次に、2 章で得た液架橋力および固体架橋付着力を導入することにより、凝集流動化挙動の数値解析を行ない、液架橋があると、凝集体を形成しながら流動化すること、圧力変動が大きくなること、水の量が大きくなるほどその傾向が強くなることを再現した。最後に、第 2 章で明らかにした、表面拡散による固体架橋力を SAFIRE モデルに取り入れ、高温での鉄粉粒子の流動化シミュレーションを行ない、液架橋がある系と異なり、分散板上にチャンネルが形成されて、流動化が停止していく様子が再現された。

　第 4 章では、固体架橋が起こるような粉体プロセッシングの系を典型例として、付着凝集挙動を制御することのできる一つの流動層プロセスを考察し、その可能性を実験的に検討した。このプロセスは、不活性粒子で鉄粉を希釈することにより過度の凝集体成長とそれによる流動化停止を防ぎ、また、偏析現象を利用して未還元粉を層上部に滞留させ、凝集体を沈降させることにより抜き出す連続操作可能なものである。常温モデル実験により、最適な媒体粒子径を見出すとともに、高温実験により、流動化停止無しに凝集体が形成し、沈降することを明らかにした。